LASER ANNEALING AND DEFECT STUDY OF CHALCOGENIDE PHOTOVOLTAIC MATERIALS

by

Ashish Bhatia

A dissertation submitted to the faculty of
The University of Utah
in partial fulfillment of the requirements for the degree of

Doctor of Philosophy

Department of Materials Science and Engineering

The University of Utah

August 2013

The University of Utah Graduate School

STATEMENT OF DISSERTATION APPROVAL

The dissertation of **Ashish Bhatia**

has been approved by the following supervisory committee members:

Michael Scarpulla	, Chair	**06/03/2013** Date Approved
Anil Virkar	, Member	**05/23/2013** Date Approved
Ashutosh Tiwari	, Member	**05/16/2013** Date Approved
Gerald Stringfellow	, Member	**05/17/2013** Date Approved
Loren Rieth	, Member	**05/16/2013** Date Approved

and by **Feng Liu**, Chair of

the Department of **Materials Science and Engineering**

and by Donna M. White, Interim Dean of The Graduate School.

ABSTRACT

$Cu(In,Ga)Se_2$ (CIGSe), $CuZnSn(S,Se)_4$ (CZTSSe), etc., are the potential chalcogenide semiconductors being investigated for next-generation thin film photovoltaics (TFPV). While the champion cell efficiency of CIGSe has exceeded 20%, CZTSSe has crossed the 10% mark. This work investigates the effect of laser annealing on CISe films, and compares the electrical characteristics of CIGSe (chalcopyrite) and CZTSe (kesterite) solar cells.

Chapter 1 through 3 provide a background on semiconductors and TFPV, properties of chalcopyrite and kesterite materials, and their characterization using deep level transient spectroscopy (DLTS) and thermal admittance spectroscopy (TAS).

Chapter 4 investigates electrochemical deposition (nonvacuum synthesis) of CISe followed by continuous wave laser annealing (CWLA) using a 1064 nm laser. It is found that CWLA at $\approx$ 50 W/cm^2 results in structural changes without melting and dewetting of the films. While Cu-poor samples show about 40% reduction in the full width at half maximum of the respective x-ray diffraction peaks, identically treated Cu-rich samples register more than 80% reduction. This study demonstrates that an entirely solid-phase laser annealing path exists for chalcopyrite phase formation and crystallization.

Chapter 5 investigates the changes in defect populations after pulse laser annealing in submelting regime of electrochemically deposited and furnace annealed CISe films. DLTS on Schottky diodes reveal that the ionization energy of the dominant majority

carrier defect state changes nonmonotonically from 215±10 meV for the reference sample, to 330±10 meV for samples irradiated at 20 and 30 mJ/cm^2, and then back to 215±10 meV for samples irradiated at 40 mJ/cm^2. A hypothesis involving competing processes of diffusion of Cu and laser-induced generation of In vacancies may explain this behavior.

Chapter 6 compares the electrical characteristics of chalcopyrite and kesterite materials. Experiments reveal CZTSe cell has an order of magnitude higher net carrier concentration and saturation current density, whereas five times smaller shunt resistance and depletion width at equilibrium compared to CIGSe. The TAS measurements suggest that the dielectric freezeout occurs at relatively higher temperatures ($\approx$ 150 K) and lower frequencies ($<$ 1 MHz) for CZTSe cell. Both sample types show a broad DLTS signal, possibly indicating a parallel recombination process with carrier emissions.

TABLE OF CONTENTS

LIST OF FIGURES

LIST OF TABLES

ACKNOWLEDGEMENTS

I would like to express my sincere gratitude to Dr. M.A. Scarpulla for giving me the opportunity to work with him and help me develop my scientific knowledge. I really appreciate your patience and guidance as you never discouraged me from asking trivial questions but at the same time always pushed me towards becoming an independent researcher. I hope I have graduated with the scientific temperament you want in your student and shall remember the lesson: "*Don't forget the big picture*" as I step out of the graduate school.

I would like to thank Dr. P.J. Dale at University of Luxembourg for being an outstanding collaborator on this project. I am indebted to Dr. Dale's student, H. Meadows, for carrying out electrochemical deposition of the samples I have used in my research.

I am thankful to Dr. A. Tiwari for kindly allowing me to carry out experiments using the 248 nm laser in his lab.

I would also like to extend appreciation to my colleagues Brian, Liz, Mak, Mitch, Vlad and Win for discussions, suggestions and help during the course of my research.

I am grateful to my parents, Sushma and Satyapal Bhatia for always encouraging me to work hard and for support in my endeavors.

Last but not the least, I don't know how to say "*Thank you*" to my wife Aruna, for tolerating me, having faith in me and always standing by my side. This work would have not been possible without the incessant support and patience exuded by you. I assure you that the time I have spent in the lab was worth it!

The work at the University of Utah was fully supported by the US National Science Foundation under the Materials World Network program award 1008302 and the work at University of Luxembourg was fully supported by Fonds National de la Recherche du Luxembourg grant MAT09/02.

CHAPTER 1

INTRODUCTION

1.1 The source of energy

A photovoltaic cell is a device which converts photon flux into electron current. Photons are the particles associated with light energy and electrons are the negatively-charged particles that bind atoms together but are also sufficiently mobile to dominate electrical conductivity. The source of the photons from the sun is nuclear fusion reactions at MeV typical energies, but the outgoing spectrum is thermalized to the sun's surface temperature of approximately 6000 K. In every second approximately $6x10^{11}$ kg of H_2 is converted into He, with a loss of about 4000 kg, which is equivalent to $4x10^{20}$ Joules as per the Einstein's relation ($E= mc^2$) [1]. The intensity of solar radiation in free space at the average distance of the earth from the sun is about 1353 W/m^2. While the solar radiation incident on the earth's atmosphere is relatively constant, the radiation at the earth's surface varies widely due to atmospheric absorption and scattering, local variations in the atmosphere such as water vapor, clouds, pollution, latitude, season, and time of day. These variations make it necessary to generate a standard solar spectrum for standardizing the testing devices: otherwise the performance in Salt Lake City, UT would not be comparable to that in Hillsboro, OR. The Air Mass (AM) is the path length which light takes through the atmosphere normalized to the shortest possible

path length (that is, when the sun is directly overhead). It quantifies the reduction in the power of light as it passes through the atmosphere and is absorbed by air and dust. The Air Mass (AM) is defined as:

$$AM = \frac{1}{Cos\theta} \tag{1.1}$$

in which θ is the angle from the vertical (zenith angle). Thus AM0 represents the solar spectrum outside the earth's atmosphere and AM1.5 conditions (with sun at ≈ 45° above the horizon) represents a satisfactory time and mid-latitude-geography-weighted average for terrestrial applications. The total incident power density for AM1.5 spectrum is ≈ 1000 W/m^2. Figure 1.1 shows the solar irradiance at AM0 and AM1.5 conditions. Inset to Fig. 1.1 illustrates the position of sun for various AM conditions.

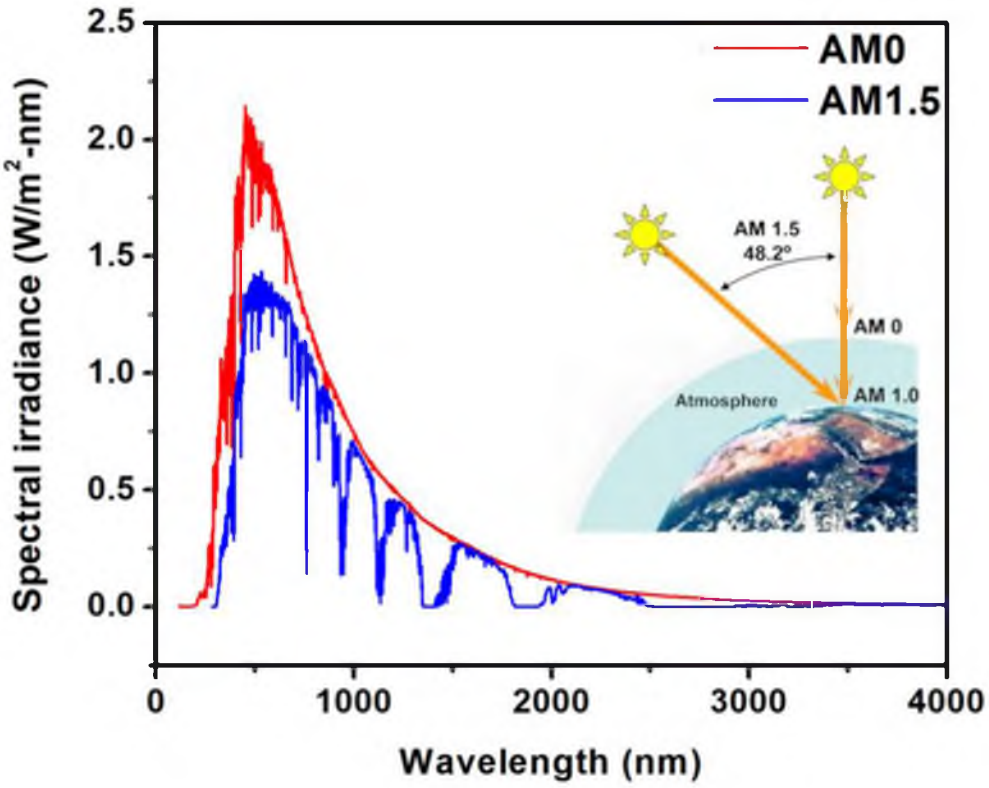

Figure 1.1: Solar spectrum for AM0 and AM1.5 conditions. Inset to figure shows the position of sun for various AM conditions.

1.2 Photovoltaic principles

1.2.1 p-n junction formation

Now, let us discuss the underlying physics of the working of a solar cell. An inorganic solar cell (relevant for this work, see examples later) is essentially a photoactive p-n junction diode. A p-n junction is formed when a p-type and an n-type semiconductor are brought in intimate contact with each other. A p-type semiconductor is one which has holes (electrons) as the majority (minority) charge carriers, while an n-type semiconductor has electrons (holes) as majority (minority) charge carriers. Since both of these have different majority charge carrier type, they are referred to as anisotype semiconductors. If the anisotype semiconductors are made out of the same material, the junction is termed as anisotype homojunction. The reader is suggested to refer to the Appendix for the discussion on anisotype p-n homojunctions.

When a p and n type semiconductors are brought in intimate contact with each other, excess free carriers move from one side to other side. The driving force for the movement is the difference in the electrochemical potential of the free carriers. This electrochemical potential is termed as the Fermi energy or level (E_f) of the free carriers. The Fermi level is defined as an arbitrary energy level that represents the charge neutrality position in the semiconductor on the energy scale. Roughly speaking it gives an idea about the average energy of the free carriers. Now, for a p-type (n-type) semiconductor that has excess holes (electrons), E_f lies close to the valence (conduction) band. Because of the difference in E_f on both the sides, the system would try to minimize its energy when in intimate contact. Thus at equilibrium or steady state, E_f is constant throughout the p-n junction. However because of the difference in the E_f on both the

sides initially, a built-in voltage (V_{bi}) or potential is created at the interface which acts as a barrier for the carrier's movement once the steady state is achieved.

Again, following the discussion in the Appendix, we could modify equation A.21 to a more robust form, if we consider the majority carrier contribution in addition to the impurity concentration, and also take into account the applied bias ($V_{applied}$) on the junction. The depletion region or the space charge region (SCR) width in that case can be calculated as per the following equation:

$$W_{total} = \sqrt{\frac{2\left(V_{bi} - V_{applied} - \frac{2k_bT}{q}\right)\varepsilon}{q\,N_{net}}} \tag{1.2}$$

in which W_{total} is the width of the SCR, k_b is the Boltzmann constant, T is the absolute temperature q is the charge on the electron, ε is the is the permittivity or the dielectric constant of the medium and N_{net} is the net space charge density.

The SCR can be visualized to be equivalent to a parallel plate capacitor, i.e., positive and negative charges separated by a dielectric medium. In that case the capacitance of the junction can be expressed as:

$$C_{depletion} = \frac{\varepsilon A}{W_{total}} = \sqrt{\frac{\varepsilon A^2\, q\, N_{net}}{2\,(V_{bi} - V_{applied} - \frac{2k_bT}{q})}} \tag{1.3}$$

As will be seen later in Chapter 5 and 6, equation 1.3 can be used to calculate the N_{net} and V_{bi} for a diode.

Figure 1.2 shows the band diagram alignment for the various bias conditions in the case of an anisotype homojunction (p and n type semiconductors are of same material). The E_f will be constant all throughout the device for equilibrium condition. When the diode is under forward (reverse) bias condition the depletion region shrinks (expands) as

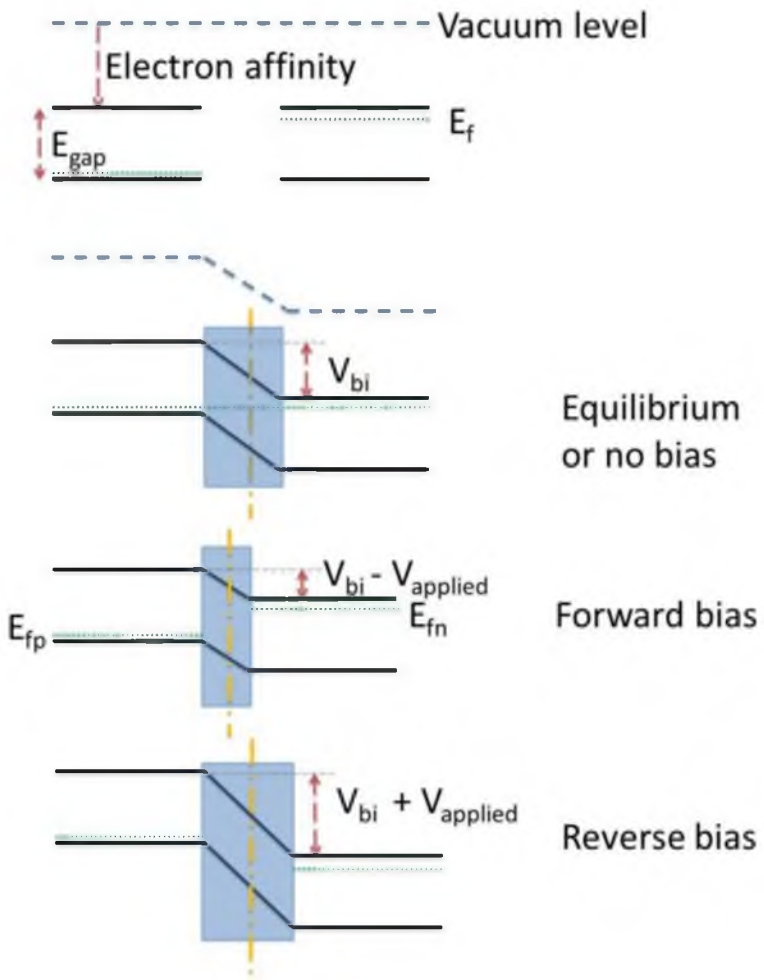

Figure 1.2: p-n homojunction formation, band bending and appearance of the barrier potential for various bias conditions.

per equation 1.2 and the barrier for carrier's movement also decreases (increases). Also since under biased condition the equilibrium condition of the diode is perturbed, the constant E_f splits into quasi Fermi levels on both the sides designated by E_{fp} and E_{fn} for holes and electrons respectively.

The discussion so far applies to the case of anisotype homojunctions, i.e., the electron affinity (energy difference between the bottom of conduction band and the vacuum level) of both the p-type as well as the n-type materials is same. Now let us take a quick look at the formation of anisotype heterojunctions.

In case of heterojunctions the electron affinity of the p-type and n-type materials is dissimilar. When these materials are brought in intimate contact with each other, SCR will be formed, V_{bi} will appear and band-bending will take place similar to the case of homojunctions. Although different cases might be possible for the case of heterojunctions, the formation of Straddling junction or Type-I junction which is most relevant to the kind of materials discussed in this work is presented over here. Although the framework for finding out the basic parameters will not change, for further details the reader is suggested to go through the references [1-5]. Now in order to calculate V_{bi} the following set of equations and procedure could be adopted:

$$\delta E_{fp} \approx k_b T \ln\left(\frac{N_v}{N_a}\right) \tag{1.4}$$

$$\delta E_{fn} \approx k_b T \ln\left(\frac{N_c}{N_d}\right) \tag{1.5}$$

where δE_{fp} and δE_{fn} represent the position of E_f with respect to valence band and conduction band in case of p and n type semiconductors respectively and N_v and N_c correspond to density of states in valence and conduction band respectively. As discussed earlier, V_{bi} develops because of the difference in the electrochemical potential or E_f on both the sides of p-n junction. Hence:

$$V_{bi} \approx \Delta E_f \tag{1.6}$$

The depletion region widths on the p-type side and the n-type side can be expressed as (after modifying equations A.23 and A.24):

$$W_p = \sqrt{\frac{2\,(V_{bi} - V_{applied})\varepsilon_p\,\varepsilon_n\,N_d}{q\,N_a(\varepsilon_p N_a + \varepsilon_n N_d)}} \tag{1.7}$$

$$W_n = \sqrt{\frac{2\,(V_{bi} - V_{applied})\varepsilon_p\,\varepsilon_n\,N_a}{q\,N_d(\varepsilon_p N_a + \varepsilon_n N_d)}} \tag{1.8}$$

and

$$W_{total} = W_p + W_n \tag{1.9}$$

Also, similar to equation.1.3:

$$C_{depletion} = \sqrt{\frac{\varepsilon_p\, \varepsilon_n\, A^2\, q\, N_a\, N_d}{2\,(V_{bi} - V_{applied})(\varepsilon_p N_a + \varepsilon_n N_d)}} \tag{1.10}$$

Figure 1.3 illustrates the formation of Type- I p-n heterojunction. The band bending principle discussed for homojunctions case is applicable to heterjunctions also. However, due to the initial offset between the respective conduction band (ΔE_c) and valence band (ΔE_v), there exists a discontinuity at the metallurgical junction interface when the junction is formed.

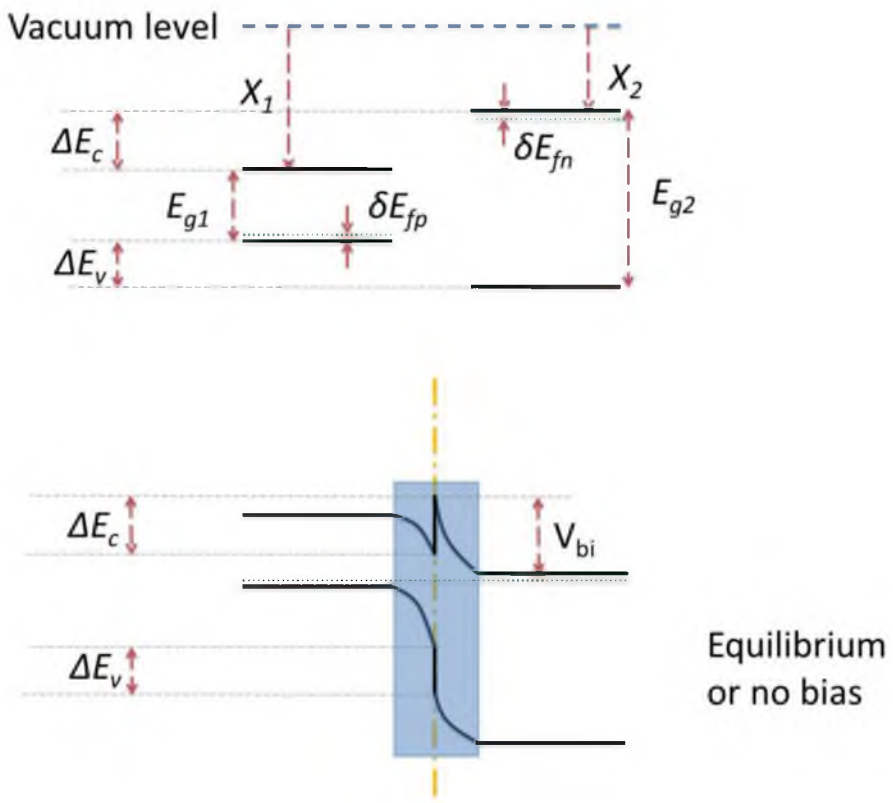

Figure 1.3: p-n junction formation, band bending and appearance of the barrier potential for anisotype heterojunction.

For the example illustrated in Fig. 1.3, the V_{bi} can be determined by the following expression:

$$V_{bi} = (X_1 - X_2) - \delta E_{fn} + (E_{g1} - \delta E_{fp}) \quad (1.11)$$

1.2.2 Photovoltaic effect

So far we saw how a p-n junction is formed in case of anisotype homo- and heterojunctions. Now, we shall discuss the principle of photovoltaic cell and how it can be used for doing work. For the sake of explanation, again consider a homojunction.

Figure 1.4 shows a photoactive p-n homojunction under equilibrium. When white light (composed of photons of different wavelength) shines on this p-n junction from the n-side, electron-hole (e-h) pairs are generated all throughout the p-n junction. This is because the incoming photons are absorbed by the material based on the complex refractive index (see Chapter 2) and hence the electrons in the valence band are promoted to the conduction band leaving behind holes in the valence band. Now, these e-h pairs diffuse randomly and eventually recombine to release photons or phonons (quasi particles associated with lattice vibrations) depending on the mechanism of recombination [6]. However, e-h pairs which are generated within the diffusion length ($L_{e/h} \approx \sqrt{D_{e/h}\tau}$) from depletion region boundary, could be drifted across the SCR because of the V_{bi}. The electrons which are minority carriers on the p-type side would be drifted towards the n-type side and vice versa. When this happens, an extra negative charge appears on the n-type side and an extra positive charge appears on the p-type side. This appears as the open circuit voltage (V_{oc}) in the cell and could be used to do work externally.

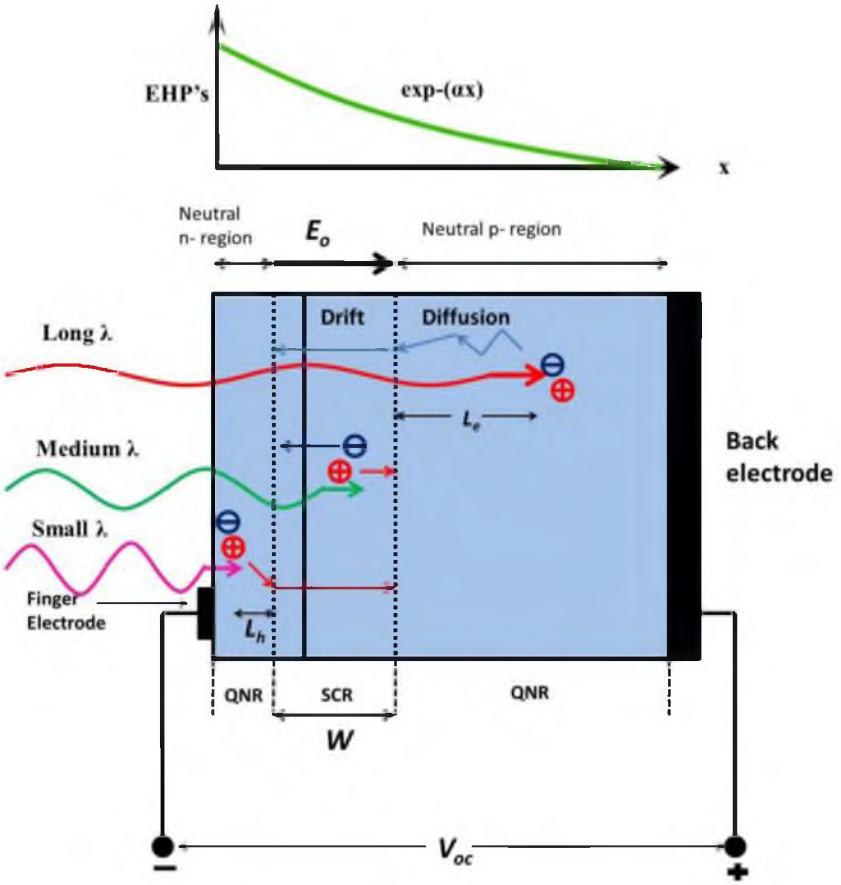

Figure 1.4: The principle of operation of a solar cell.

If we look closely we will realize that a solar cell works when the minority carriers become the majority carriers and the sooner it occurs, the better it is for the device performance. Also, an important thing to be kept in mind while designing the solar cell is that the e-h pair generation rate will fall off exponentially along the depth as per the Beer-Lambert's law [1], and thus the main absorber layer should be chosen based on minority carrier diffusion length. For example, in case of homojunctions the absorber layer should be p-type if electrons (minority carriers) have a larger diffusion length.

Thus under light, the current density of the p-n junction could be expressed by the following equation:

$$J = J_{diode} - J_{ph} = J_o \left[\exp\left(\frac{qV}{k_bT}\right) - 1\right] - J_{ph} \quad (1.11)$$

where J is the net current density, J_{ph} is the current density because of the photon absorption also termed as the short circuit current density (J_{sc}) and J_o is the saturation current density. Thus if J = 0:

$$J_{ph} = J_o \left[\exp\left(\frac{qV_{oc}}{k_bT}\right) - 1\right] \quad (1.12)$$

$$V_{oc} = \frac{k_bT}{q} \ln\left(\frac{J_{ph}}{J_o} + 1\right) \approx \frac{k_bT}{q} \ln\left(\frac{J_{ph}}{J_o}\right) \quad (1.13)$$

Thus we see that V_{oc} is a function of J_{ph}, J_o and temperature. In order to maximize V_{oc} we have to aim for maximum J_{ph} and minimum J_o. Now, J_{ph} is governed by the band gap of the material; i.e., the smaller the bandgap of the material the larger the J_{ph} because of more photon capture and vice versa. Hence we can realize from Fig. 1.1 that the band gap of the material sets an upper limit on the maximum possible J_{ph}. If we consider the AM1.5 spectrum in Fig. 1.1 and integrate the flux of incoming photons at each different wavelength as per the following expression we would end up with the maximum J_{ph} possible for each different bandgap:

$$J_{ph}\,(max)|_{E_g} = q \int_{E_g}^{\infty} \Gamma_{ph}(E)dE \quad (1.14)$$

where E_g is the band gap of the particular material and Γ_{ph} is the photon flux at the corresponding energy. In the above expression the quantum conversion efficiency of photons to electrons is assumed to be unity.

Again J_o can be expressed as per the following expression:

$$J_o = q\, N_c\, N_v \left(\frac{1}{N_a}\sqrt{\frac{D_n}{\tau_n}} + \frac{1}{N_d}\sqrt{\frac{D_p}{\tau_p}}\right) \exp\left(-\frac{E_g}{k_bT}\right) = J_{OO} \exp\left(-\frac{E_g}{k_bT}\right) \quad (1.15)$$

where N_c and N_v are density of states of the conduction and valence band, respectively, N_a and N_d are acceptor and donor atom densities, D_n and D_p are diffusion lengths of

electrons and holes, respectively, and τ_n and τ_p are lifetimes of electron and holes, respectively. The preexponential factor J_{oo} combines all these terms and as per Ref. [7-8] it is approximately $\approx 10^8$-10^9 mA/cm^2 for good quality diodes. Thus we can infer from equation 1.15 that J_o is inversely related to E_g, i.e., larger the band gap smaller the J_o. Hence in order to maximize V_{oc} one has to make a compromise and chose the optimum band gap material.

Again a theoretical limit could be set up on the V_{oc} based on the band gap of the material. The ideal-maximum V_{oc} possible for a solar cell is:

$$V_{OC}\ (ideal\ maximum)|_{E_g} = E_g \tag{1.16}$$

However, due to nonideal factors such as recombination of free carriers in SCR and or quasi-neutral region and or interface etc., this scenario is never realized. Hence the V_{oc} at room temperature always tend to be smaller than E_g. Now if we replace J_o in equation 1.11 by the expression in equation 1.15, we can find an expression for V_{oc} which is given by:

$$V_{oc}\ (maximum)|_{E_g} = \frac{E_g}{q} + \frac{k_b T}{q} \ln\left(\frac{J_{ph}}{J_{oo}}\right) \tag{1.17}$$

in which J_{ph} for the corresponding E_g is given by equation 1.14. Thus using equation 1.14 and 1.17 we can end up with the Fig. 1.5, which shows the maximum possible J_{ph} and V_{oc} for various band gaps.

Now the overall efficiency (η) of a solar cell is defined as:

$$\eta = \frac{Output\ power}{Input\ power} = \frac{P_{out}}{P_{in}} \tag{1.18}$$

where P_{in} is the input power density at AM1.5 conditions ($\approx$ 1000 W/m^2) and P_{out} is the maximum output of the solar cell. The P_{out} is given by:

$$P_{out} = V_{max} J_{max} = FF\ V_{oc} J_{ph} \tag{1.19}$$

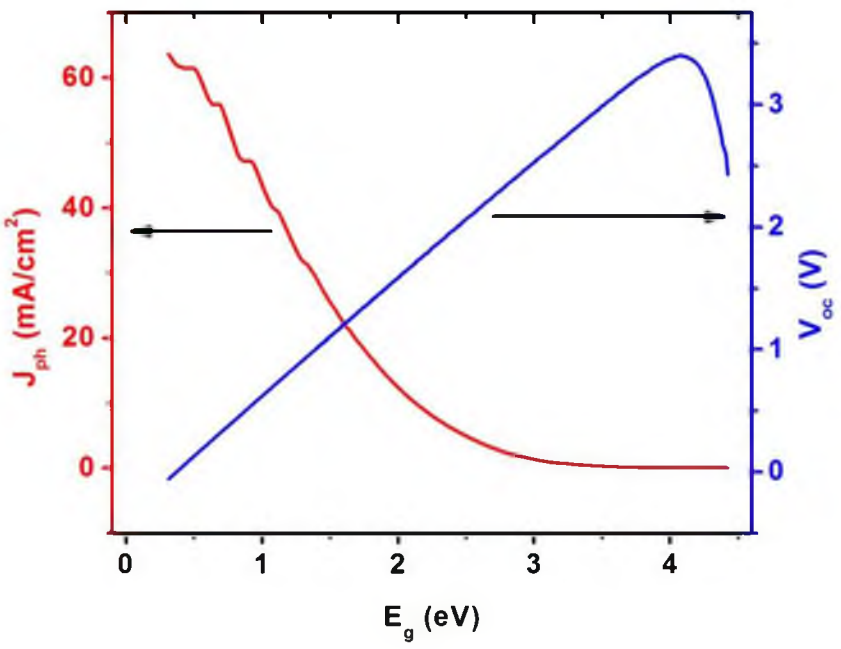

Figure 1.5: Maximum possible J_{ph} and V_{oc} for various materials band gap.

where FF stands for fill factor and is defined as the ratio of the actual maximum output power density to maximum possible theoretical power density. Figure 1.6 illustrates the various terms discussed above. Thus equation 1.18 can be written as:

$$\eta = \frac{V_{oc} J_{ph} FF}{P_{in}} \tag{1.20}$$

Again, based on the above discussion a theoretical efficiency limit could be imposed on the material based on its band gap. This is usually referred to as the principle of detailed balance. For an exhaustive treatment on the detailed balance, reader could refer to [9]. However, based on the assumptions made in the above discussion, an approximate solution [10] to theoretical efficiency curve is presented here. Figure 1.7 shows the approximate solution to the detailed balance problem. By using the expressions for V_{oc} (equation 1.17), J_{ph} (equation 1.14), assuming FF to be 0.85 and P_{in} as the AM1.5 input power density, one could arrive at Fig. 1.7. We can see from the figure that the

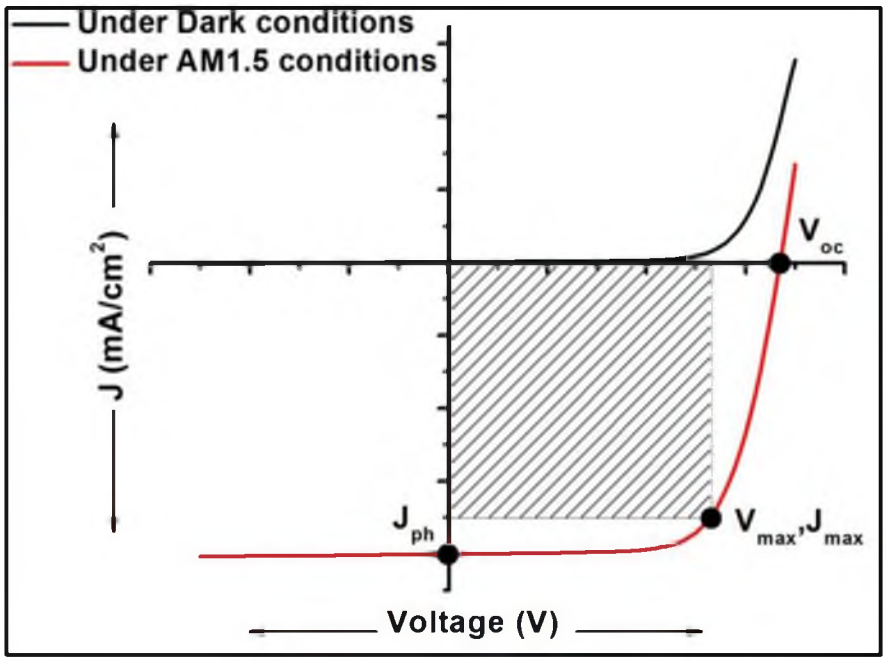

Figure 1.6: J-V characteristic of a solar cell under dark and AM1.5 conditions.

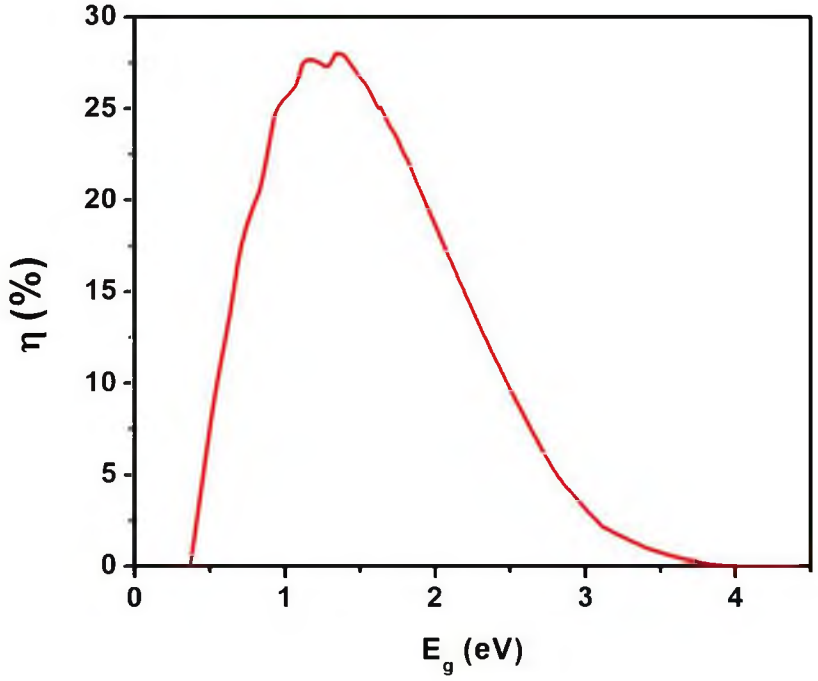

Figure 1.7: Approximate solution to the problem of detailed balance.

theoretical efficiency curve peaks around 1-1.5 eV. Thus a semiconductor material which has a bandgap in the range of 1-1.5 eV is most suited for photovoltaic application.

The net current density expressed by equation 1.11, can be modified to the following if we consider the effect of parasitic resistances:

$$J = J_0 \left[\exp\left(\frac{q(V-JR_s)}{nk_bT}\right) - 1\right] + \frac{V-JR_s}{R_{sh}} - J_{ph} \qquad (1.21)$$

where R_s is the series resistance, R_{sh} is the shunt resistance and n is the diode ideality factor. The term R_s usually accounts for the resistance offered by the quasi neutral semiconductor regions to the charge carriers and also the contact resistance between the metal grid and the semiconductor.

The main impact of R_s is to reduce the FF, although excessively high values may also reduce the J_{ph}. The R_{sh} is associated with the leakage or alternate shortcut current path in the solar cells. Thus for maximum J, one should aim for minimum R_s and maximum R_{sh}. Figure 1.8 illustrates the equivalent solar cell circuit including R_s and R_{sh} and also the effect of R_s and R_{sh} on the I-V characteristics of solar cell.

The diode ideality factor is also an important indicator of the optoelectronic quality of the p-n junction. Ideally, n should be unity but because of the nonradiative recombination process inside SCR and other nonideal effects (as mentioned above), n tends to be greater than unity. Figure 6.7 in Ref. [2] illustrates the effect of diode ideality factor on I-V curves for various semiconductor materials.

Last but not the least, temperature also affects the performance of a photovoltaic device. As temperature increases, firstly the bandgap will decrease according to Varshini's equation [1]. Also a higher temperature implies larger minority carrier diffusion length. Both of these effects will increase J_{ph} with increasing temperature.

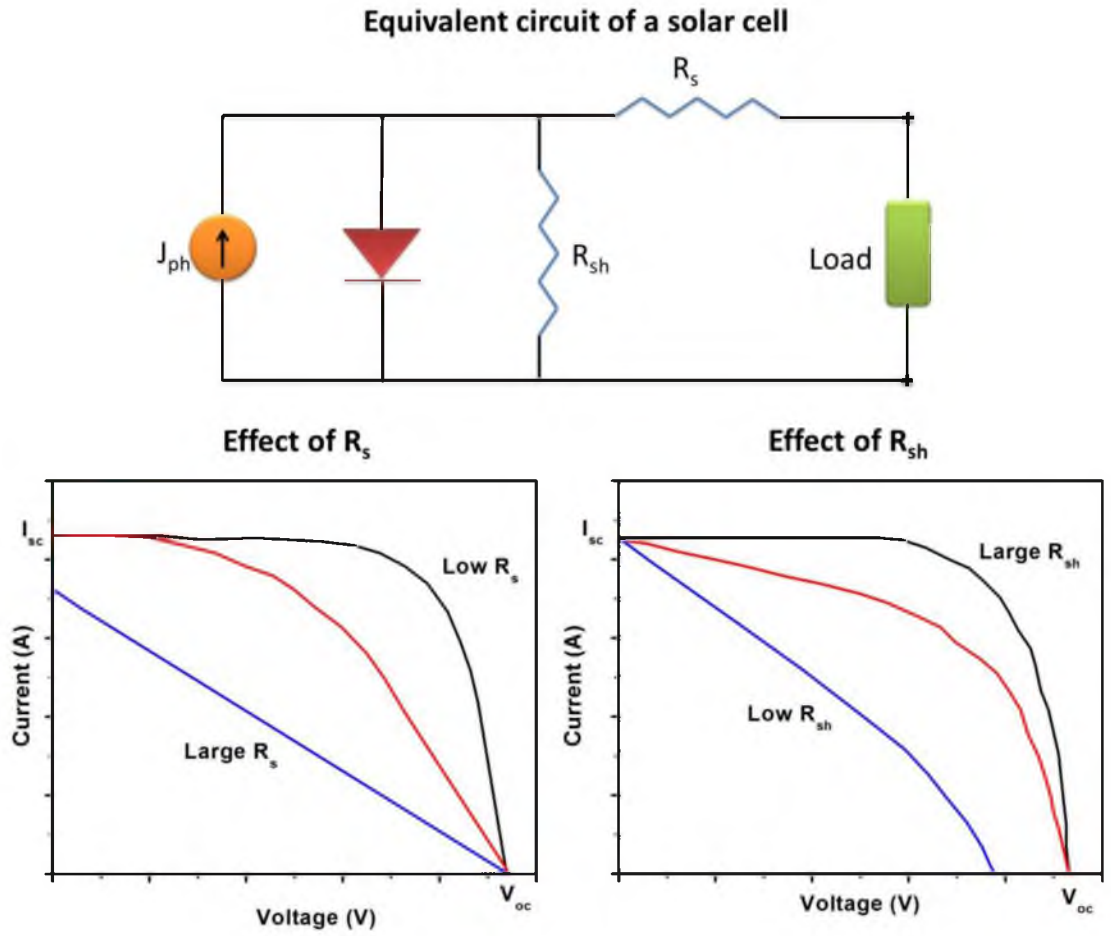

Figure 1.8: Equivalent circuit of a solar cell with parasitic resistances and the effect of R_s and R_{sh} on I-V characteristics of solar cell (modified after Ref. [10]).

However, an increase in temperature also causes an exponential increase in J_0 as per equation 1.15. Since the percentage change in E_g is less than the percentage change in absolute temperature, the net effect is an exponentially decreasing V_{oc}. The V_{oc} effect dominates J_o effect resulting in decreasing efficiency with increasing temperature. Hence cold-sunny environment is best suited for solar cells.

1.3 References

[1] S.M. Sze and K.K. Ng, Physics of Semiconductor Devices, Wiley India Pvt. Ltd., Third edition, 2009.

[2] S.O. Kasap, Principles of Electronic Materials and Devices, Tata McGraw-Hill Publishing Company Limited, Third edition, 2008.

[3] R. Scheer and H.W. Schock, Chalcogenides Photovoltaics: Physics, Technologies and Thin Film Devices, Wiley-VCH Verlag GmbH & Co. KGaA, Weinheim, Germany, 2011.

[4] D.A. Neamen, Semiconductor Physics and Devices: Basic Principles, Richard D Irwin publishers, Second edition, 1997.

[5] https://nanohub.org/resource_files/2007/05/02660/adept_heterostruct_tutorial.pdf

[6] http://pveducation.org/pvcdrom

[7] http://www.superstrate.net/pv/limit/limit.html

[8] A. Shah, Thin-Film Silicon Solar Cells, EPFL press, 2010.

[9] W. Schockley and H.J. Queisser, J. Appl Phys. 32(3) (1961) 510.

[10] M.A. Green, Solar Cells: Operating Principles, Technology and System Application, University of NSW, 1992.

CHAPTER 2

CHALCOGENIDE PHOTOVOLTAIC MATERIALS

2.1 Properties and solar cell structure

2.1.1 Properties of chalcogenide absorbers (CISe: Chalcopyrite type)

The chalcogenide absorbers are compounds that contain one of the group VI elements such as S, Se etc. $CuInSe_2$ (CISe), $CuZnSnS_4$ (CZTS) and their other derivatives (mentioned later) are the potential Cu-based compound semiconductors that are being used and investigated for next generation photovoltaics.

CISe is a thin film semiconductor that offers various advantages and the following properties:

1) It has a tetragonal crystal structure which is regarded as the superstructure of ZnSe (Zinc blende). The chalcopyrite structure could be derived by ordered substitution of Zn atoms with Cu and In atoms. See Fig. 2.1.

2) It is a direct bandgap semiconductor whose bandgap can be varied from $\approx$ 1-2.67 eV by alloying it with other elements such as Ag, Al, Ga, S etc. Firstly, since it is a direct bandgap semiconductor, it is good for optoelectronics applications. This is because in a direct bandgap semiconductor, a band to band transition leading to creation of an electron-hole (e-h) pair is more probable to occur as against an indirect bandgap semiconductor such as silicon.

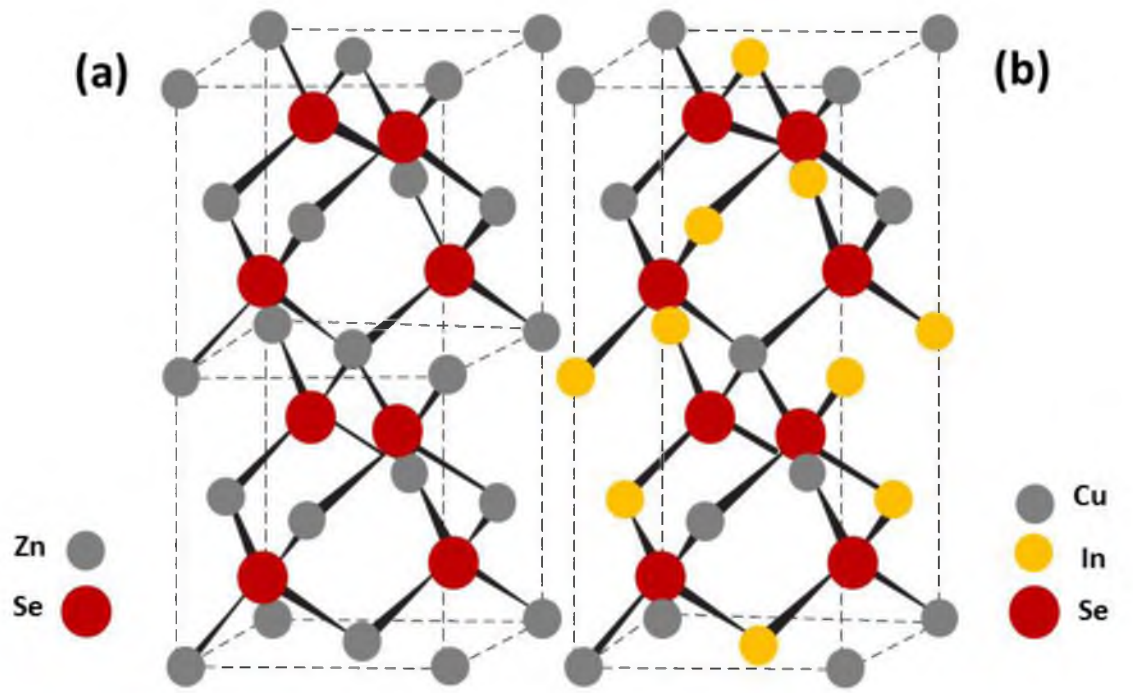

Figure 2.1: Comparison of (a) Zinc blende and (b) Chalcopyrite crystal structures.

Secondly, the maximum in the Shockley-Queisser theoretical efficiency limit calculation [1] (also see Fig. 1.7) occurs in the range from ≈ 1-1.5 eV. Hence the bandgap of CISe could be manipulated within the optimum bandgap range. The various alloying atoms such as Al, Ga, and S are smaller than the corresponding In cations and Se anions. Hence the bandgap tends to increase from the base value of ≈ 1eV. For this class of compounds, alloying with cations usually effects the conduction band while alloying with anions usually effect both the conduction as well as valence band. Figure 2.2 shows the variation in the bandgap with alloying.

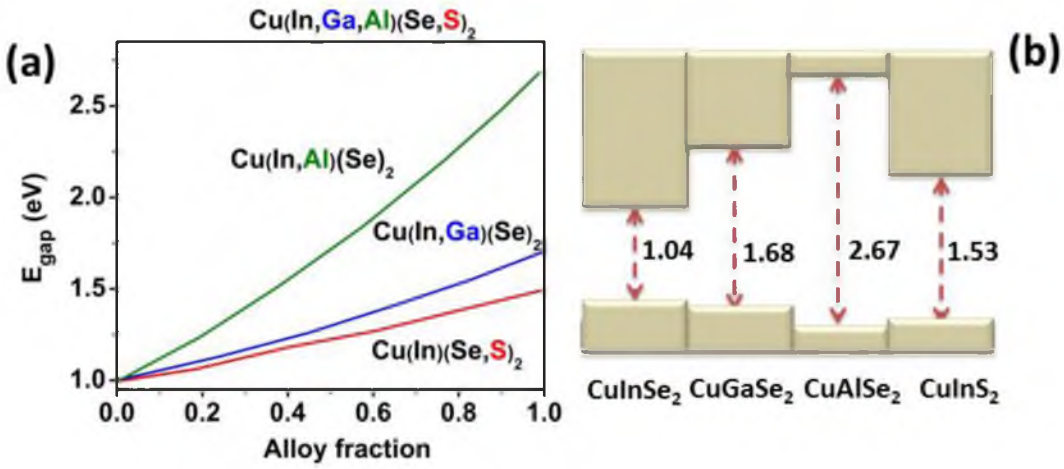

Figure 2.2: Variation and lineup of bandgaps in chalcopyrites. (a) Variation of bandgap of CISe by alloying with various elements in various proportions and (b) lineup of the actual band diagram of various chalcopyrites. Figure modified after Ref. [2].

3) CISe has a very high optical absorption coefficient (α) $\approx 10^4$ cm^{-1} for photons with energy $\geq$ bandgap. This translates into an optical absorption depth of $\approx$ 1µm as per the Beer-Lambert's law [3]. Hence a solar cell based on CISe absorber layer needs only 1 µm thin film of CISe. This number is in contrast to Si which has a very low optical absorption coefficient ($\approx 10^2$ cm^{-1}) , and hence one needs a thick layer $\approx$ 100 µm, for a solar cell made out of Si absorber. Figure 2.3 shows the absorption coefficient of various semiconductors for photons with different energy.

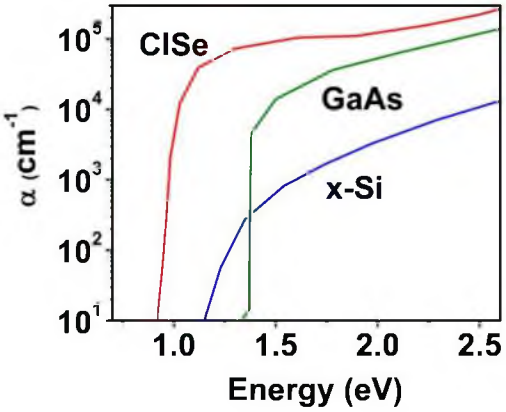

Figure 2.3: Optical absorption coefficient of various semiconductors. Figure modified after Ref. [4].

4) CISe is very tolerant towards large stoichiometric deviations. This implies that even if the atomic ratio of the synthesized CISe compound semiconductor is not 1:1:2, the chalcopyrite phase is still formed. $CuInSe_2$ and other chalcopyrites can tolerate a large range of anion to cation off stoichiometry, i.e., samples with few atomic % of Cu-poor and/or In-poor stoichiometries are stable [5]. As a result of nonstoichiometry, native defects are formed in CISe which are responsible for its doping, electrical and optical behavior. These native defects have low defect formation enthalpies (< 1 eV) as compared to elemental or II-VI semiconductors [5-6] and play an important role in the optoelectronic properties of these compounds (discussed next).

5) CISe is natively p-type and hence no additional dopant atoms are needed as in case of Si. This can be attributed to its native defect equilibrium. In the ternary CISe system, at least 12 native defects (see Chapter 3) are possible: three vacancies (V_{Cu}, V_{In}, V_{Se}), at least three interstitials (Cu_i, In_i, Se_i) and six antisite defects (Cu_{In}, Cu_{Se}, In_{Cu}, In_{Se}, Se_{Cu}, Se_{In}). Additionally, various defects can interact to form defect complexes such as, $(2V_{Cu}^{-} + In_{Cu}^{+2})^{0}$, etc. It is generally believed that V_{Cu}^{-} cause p-type conductivity whereas Cu_i^{+} and In_{Cu}^{+2} antisite defects give n-type character to CISe [7]. Zhang et al. [5] have theoretically calculated the formation energies of various point defects in CISe (excluding V_{Se}) using first-principles self-consistent electronic structure theory. They found that the V_{Cu} is easy to form in CISe and its defect formation energy varies from 0.6 to -2.41 eV for various stoichiometries and electron Fermi energy.

Interestingly the off-stoichiometry in CISe, which leads to a large number of defects, does not seems to have a negative impact on its electronic properties [8]. This has been attributed to the formation and interaction of defect complexes. The formation energy of

defect complex $(2V_{Cu}^{-} + In_{Cu}^{+2})^{0}$ is actually negative. Again this is in huge contrast to II-VI and III-V semiconductors in which the lowest native defect complex formation energies are roughly 5 eV [5].

Also it is interesting to note that the pairing of defects can alter the electrical activity. For example, an isolated V_{Cu}^{-} is a shallow acceptor (discussed in Chapter 3), while an isolated In_{Cu}^{+2} is a deep donor (discussed in Chapter 3), but a defect pair based on $[2V_{Cu}^{-} + In_{Cu}^{+2}]^{0}$ is electrically inactive, i.e., neither a dopant nor a recombination center. Because of the negative formation energy of defect complex in CISe, large bandgap Cu-depleted ordered defect compounds (ODC's) such as $CuIn_5Se_8$, $CuIn_3Se_5$, etc., can form at surfaces and grain boundaries of CISe. The band alignment of CISe and ODC's as per Ref. [8-9] is shown in Fig. 2.4. It can be realized from Fig. 2.4 that if an electron-hole (e-h) pair is created in the bulk of a CISe film, the minority electron would move towards the ODC while the majority hole sees a barrier towards the ODC and hence moves towards the bulk region. This reduces the probability of e-h pair recombination.

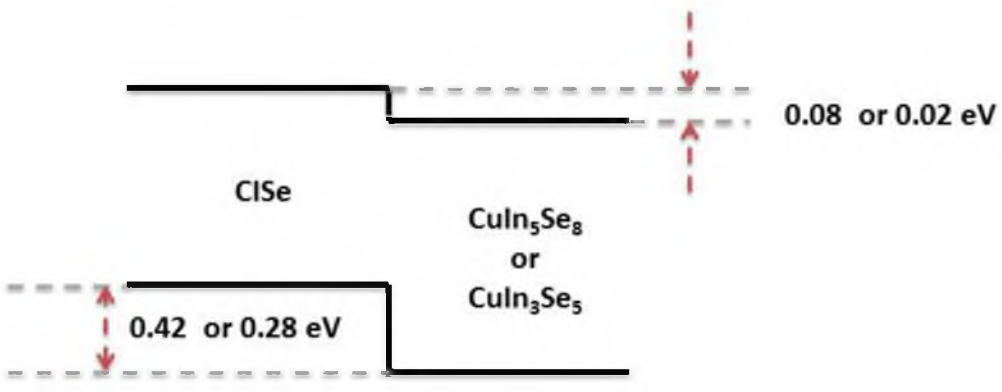

Figure 2.4: Flat band alignment of CISe and ODC. Figure after Ref. [8-9].

Evidence of Cu-depletion at the surface of CISe and related compounds comes from experimental results as well [10-12]. It has been reported that for bulk compositions with a relative Cu content in the range of $([Cu]/[III])_{int} = 0.55–0.90$, surface compositions of around $([Cu]/[III])_{surf} \approx 0.35$ have been found. Figure 3(a) in Ref. [10] shows the depth profiles of various CISe films with varying bulk compositions. It can be concluded from the figure that the depth of the inflection point of the Cu/III distribution varies from 3 to 25 nm. Another interesting aspect associated with the Cu-depletion is the type inversion of the CISe semiconductor layer at the surface. It has been found that as-grown $CuIn_3Se_5$ films are slightly n-type with very high resistivity [13]. This is evidence that a native p-n junction is formed by CISe-ODC semiconductors, which helps in the reduction of recombination at the metallurgical interface between CISe and CdS (see section 2.1.2). It is worthwhile to mention now that in order to achieve an efficient device quality p-type CISe absorber, an overall slightly Cu-poor composition is necessary, whereas the region close to the buffer/absorber interface should be of n-type character by exhibiting a very Cu-poor composition [14].

Figure 2.5(a) shows the various possible phases in the ternary Cu-In-Se system. The chalcopyrite phase along with the ODC's, lie on the tie line between Cu_2Se and In_2Se_3 phases. The detail of the tie-line near $CuInSe_2$ is given by the pseudobinary phase diagram reproduced in Fig. 2.5(b). Here α is the chalcopyrite $CuInSe_2$, δ is a high-temperature phase with the sphalerite structure, and β is an ODC phase. A comprehensive study on the phase diagram of Cu-In-Se system has been reported by Gödecke et al. [15].

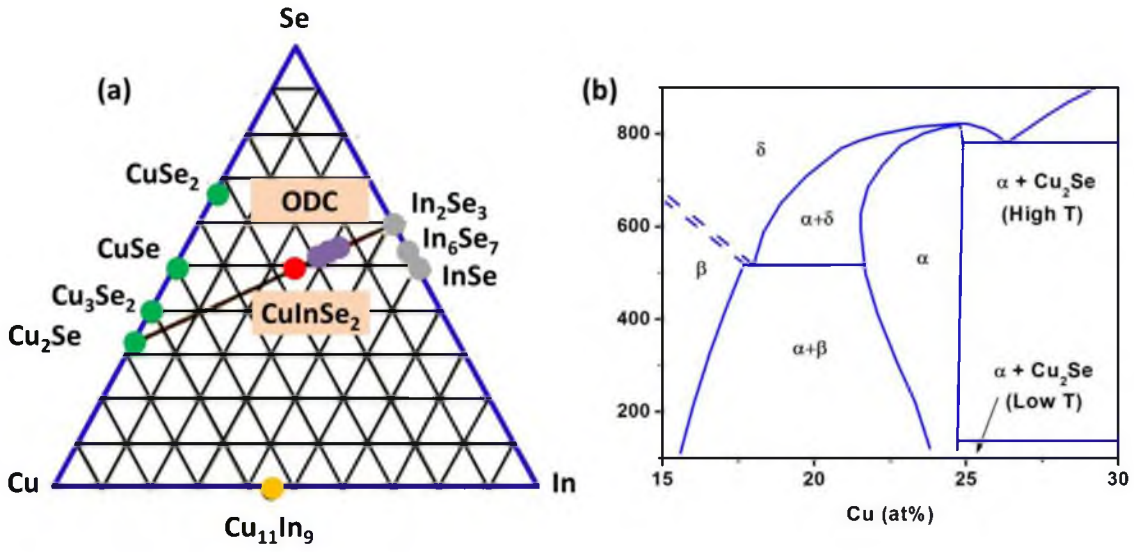

Figure 2.5: Phase diagrams of Cu-In-Se material system. (a) Ternary phase diagram of Cu-In-Se system. Thin films usually have composition near Cu_2Se-In_2Se_3 tie line. (b) Pseudobinary Cu_2Se-In_2Se_3 equilibrium phase diagram close to chalcopyrite $CuInSe_2$ phase (α). Figure after Ref. [15].

6) The most intriguing characteristic associated with chalcopyrite semiconductors is that the polycrystalline films seem to be more efficient than the corresponding single crystal counterparts [14, 16-20]. This is in contrast to semiconductors such as Si, GaAs etc. Although a lot of theories have been proposed to date to explain this behavior, but a general consensus has so far not been achieved. Hence a brief overview of the grain boundary (GB) theory in general is presented over here, followed by the proposed theories for chalcopyrites.

A polycrystalline material is composed of crystallites or grains arranged randomly with respect to each other. Inside each grain the atoms are arranged in a periodic manner so that it can be considered as a small single crystal. This is because the grains are large (≈ 1μm) in quantum mechanical terms and hence the mechanical, thermal, optical and electronic properties of the bulk grain is almost identical to single crystal material or the theoretical results. However at the free surface or the grain boundary the periodicity of

the crystal is destroyed and hence the above mentioned properties should be affected. The grain boundary is a complex structure, usually consisting of a few atomic layers of disordered atoms, dangling bonds, adsorbed species, etc., which represent a transitional region between the different orientations of neighboring grains.

As per Seto [21] there are two theories associated to describe the effect of grain boundaries on the electrical properties of semiconductors. One theory states that grain boundary acts as a sink for impurity atoms due to impurity segregation at the grain boundary. Consequently, the amount of impurity in the bulk grains is reduced making them more resistive in comparison to grain boundaries. The other theory states that since the atoms at the grain boundary are disordered, there are a large number of defects due to incomplete atomic bonding. This results in the formation of trapping states, which are capable of trapping carriers and thereby immobilizing them. This reduces the number of free carriers available for electrical conduction. After trapping the mobile carriers, the traps become electrically charged, creating a potential energy barrier which impedes the motion of carriers from one crystallite to another. Based on this theory, for the same amount of doping, the mobility and carrier concentration of a polycrystalline semiconductor would be less than that of a single crystalline material. These two theories have been used over the years [22-26] to explain the behavior of polycrystalline semiconductor films such as in case of Si.

Now, before delving into the discussion of chalcopyrites grain boundary theories, let us take a quick look at the defect physics of the free surface and or grain boundaries that will help us understand the band diagram and band bending for polycrystalline material. As mentioned earlier the grain boundary consists of dangling bonds or states that are

capable of capturing free carriers. Similar to bulk defect states (Refer to Chapter 3), an interface defect is considered as a donor (acceptor) if it is neutral and can become positively (negatively) charged by donating (accepting) an electron. Also, analogous to the case of bulk semiconductors, where the Fermi level (E_f) denotes the charge neutrality position (See Chapter 1), a charge neutrality level (E_o) is defined for free surface too. In equilibrium, all the states above E_o are empty and all the states below E_o are filled with electrons. Now consider a situation as shown in Fig. 2.6, where two p-type grains are separated with a grain boundary that has $E_0 > E_f$ initially. Again following the band bending principles discussed in Chapter 1 (also see Schottky barrier formation in Chapter 3), we can see that the bands will bend downwards, a positive charge appears at grain boundary (donates electrons) and a negative charge (accepts electrons) on the grains side.

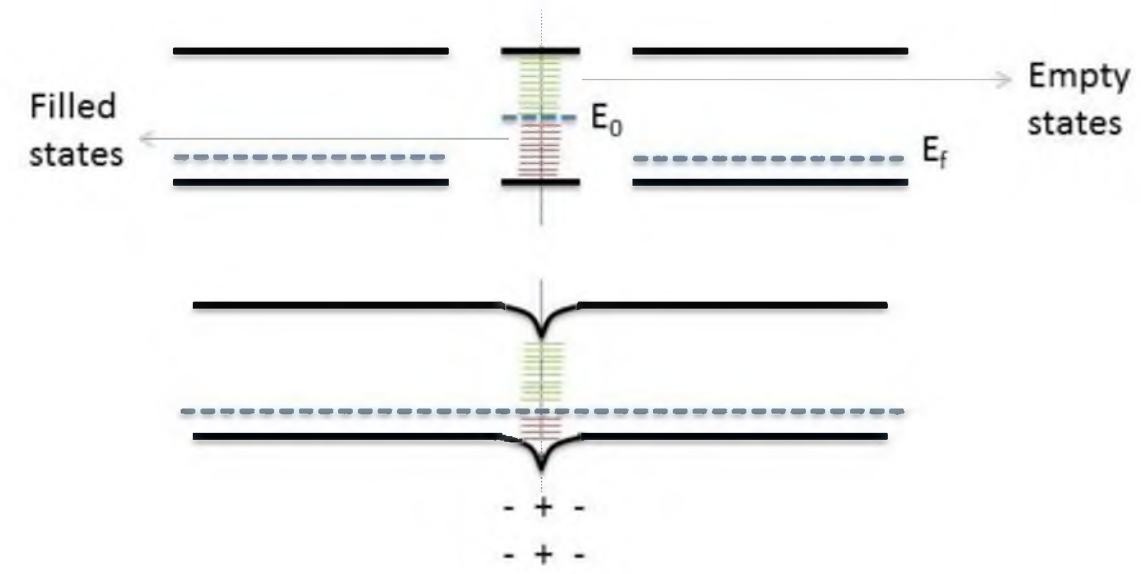

Figure 2.6: Band bending and appearance of back-to-back Schottky barriers in two p-type grains separated by a grain boundary with $E_0 > E_f$.

Again, as mentioned earlier, polycrystalline CIGSe films outperform their epitaxial counterparts and hence several theories have been proposed to explain this phenomenon. In general there are four models available in chalcopyrite literature which addresses this issue. Although a large literature is available discussing the effects of grain boundaries, the work of Gloeckler et al. [27-28] who have considered all of the four cases and have tried to predict the behavior of films and cells under these conditions is discussed here. Figure 2.7 schematically illustrates the proposed models for grain boundary behavior in chalcopyrite.

The electrically benign grain boundary model states that the band diagram at the grain boundary is indistinguishable from the band diagram of the bulk material and the electronic defect states lie in the valence band rather than in the bandgap region. The

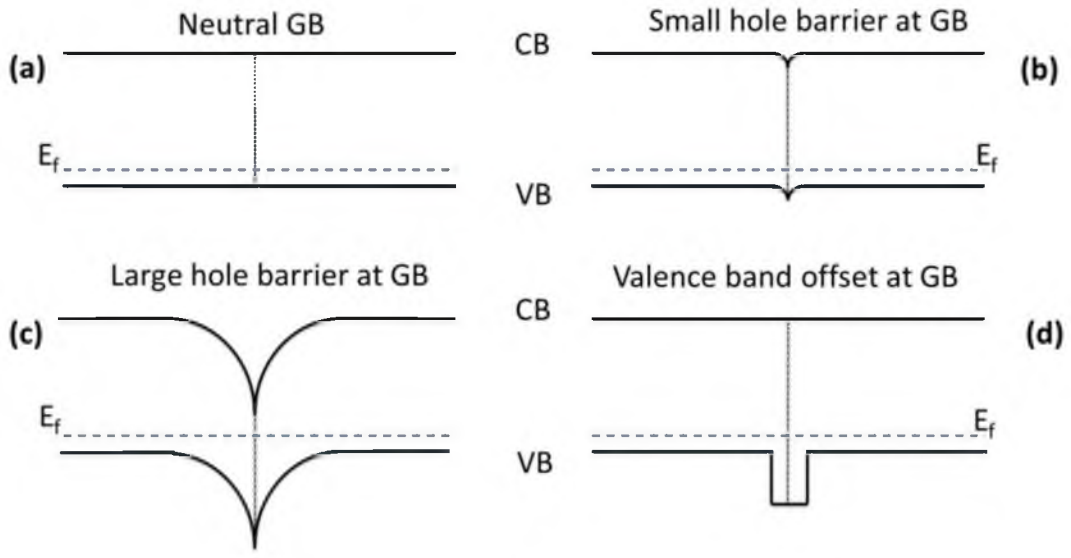

Figure 2.7: Various grain boundary band diagram models for polycrystalline semiconductors. The figure shows: (a) Benign grain boundary model, (b) Positively charged grain boundary model with small barrier, (c) Positively charged grain boundary model with large barrier and (d) Valence band offset model. Figure after Refs. [27-28].

positively charged grain boundary model is based on grain boundary discussion made earlier (see Fig. 2.6). However, two cases are possible, where a small or a large barrier for holes could be present at the grain boundary. A large hole barrier actually helps in type inversion at the grain boundary, which helps in minority carrier transport. The valence band offset model states that the offset in valence band causes a reduced free hole density at the grain boundary leaving fewer unoccupied states available for electrons within the conduction band, which effectively results in a reduced recombination rate. The VB offset model is actually in agreement with the formation of ODC's (Cu-depletion) at the free surface (see Fig. 2.4) which mainly affects the VB.

If we look at the results in Fig. 3 of Ref. [27], we can conclude that the recombination rate and the associated current loss is least for case (c) and case (d), i.e., positively charged grain boundary with large barrier for holes and valence band offset model. The simulated current density-voltage (J-V) curves (see Fig. 14 in Ref. [27]) under AM1.5 spectrum for solar cells made out of these types of precursor layers are in agreement with the above results. Again, case (c) and case (d) precursors tend to minimize the effect of grain boundaries in case of chalcopyrites. Also see section 2.2 in order to draw comparison between GB's in CIGSSe and CZTSSe type materials.

The above discussed characteristics make polycrystalline chalcopyrites as interesting photovoltaic absorber layer materials and hence they have been the subject of research and industrial interest for many years.

2.1.2 Fabrication of chalcogenide solar cells

The complete solar cell structure of CISe based solar cells is illustrated in Fig. 2.8. CISe is used in conjunction with various other semiconductor materials to form a heterojunction solar cell. Let us take a look at the various materials involved one by one.

2.1.2.1 Substrate

Soda lime glass (SLG), although one of the cheapest commodity glasses, is the preferred substrate for CIGSe based photovoltaics. The thermal expansion coefficients (TEC) of CISe and SLG match closely: The TEC for SLG is $9x10^{-6}$ K^{-1}, while for CISe it is $8.32x10^{-6}$ $K^{-1}$and $7.89x10^{-6}$ K^{-1} perpendicular to and parallel to c-axis, respectively [14]. Initially SLG was used as the substrate as it was stable during CISe processing as well as cost effective. However it was realized that the Na diffusing out of SLG plays an important role in synthesizing device-quality CISe films. The Na diffuses through the Molybdenum (Mo) layer via grain boundaries into the CISe film and affects

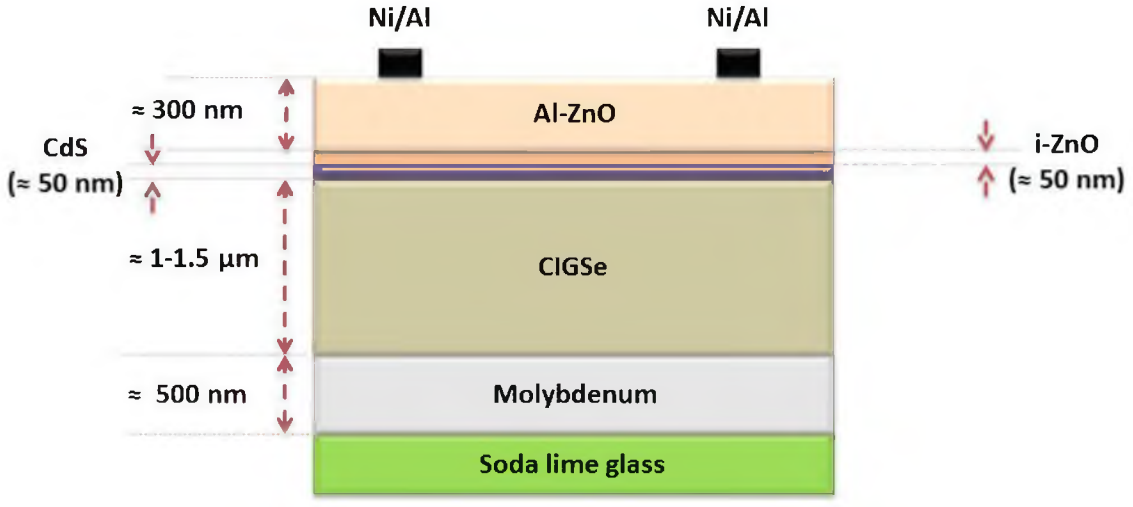

Figure 2.8: Complete solar cell heterostructure of chalcogenide solar cell.

its properties. A typical Na concentration in high efficiency CIGSe solar cells is ≈ 0.1% [14]. In CISe, Na accumulates at grain boundaries (see Fig. 1 in Ref. [29]) and presumably passivates them and increases p-type conductivity [30-31]. Optimum Na doping mainly improves fill factor and open circuit voltage of the solar cell [30-31]. The effect of Na on the grain size and preferred orientation of CISe films seems to be contradictory [14, 32-35].

If flexible (stainless steel etc.) or other substrates (borosilicate glass etc.) are used, Na could be incorporated in controlled amount by depositing a thin layer of Na containing compound on top of the substrate [32] or post deposition of Na containing compound on top of the film followed by heat treatment [31].

2.1.2.2 Back contact layer

Molybdenum (Mo) forms the back contact layer and is deposited using DC magnetron sputtering. Mo is used because it has negligible diffusion into the CIGSe film and it does not form a high recombination back surface. Interestingly the work function of Mo (≈ 4.6 eV) is smaller than the work-function of CISe. Hence, it should form a Schottky-contact (see Chapter 3) with CISe. However, Mo forms a layer of $MoSe_2$ (≈ 100 nm) during the CISe processing (see Fig. 3 in Ref. [36]) which possibly is responsible for the Ohmic behavior at the back contact.

In addition to Mo, Orgassa et al. [37] have tried solar cell fabrication with other back contact layers such as W, Cr etc. and evaluated the performance of CIGSe solar cells. They found that while the performance of W was comparable to Mo, Cr reacts with CIGSe during the growth.

2.1.2.3 Buffer layer

The first layer in direct contact with the CISe layer from the top forms the buffer layer. A thin layer (≈ 50 nm) of CdS (≈ 2.4 eV) usually deposited by chemical bath deposition (CBD) [14, also see Chapter 5], instead of physical vapor deposition, is generally used as the buffer layer. The CBD process is preferred as it gives more conformal deposition [38]. Although the role of CdS layer is still under active research, various advantages have been identified over the years, such as removal of native oxides from CIGSe surface [39] and protection of CIGSe surface from high energy ions during sputtering of window layers (see section 2.1.2.4). However the most important aspect of CdS deposition is that Cd diffuses into the CIGSe layer within few atomic layers (see Fig. 2 and Fig. 3 in Ref. [40]) and induces type inversion of the CIGSe layer by forming a shallow Cd_{Cu}^{+} defect [14, also see Chapter 3].

Because of the toxicity of Cd, other buffer layers under investigation are ZnS, ZnSe, $In(OH)_3$, Zn(O,OH) etc. [14].

2.1.2.4 Window layers

The transparent window layers consist of a highly-resistive intrinsic i-ZnO layer (≈ 50 nm) and a highly conductive aluminum doped n-ZnO layer (≈ 300 nm). Both of these films are usually deposited by RF sputtering [14, also see Chapter 5]. Although the role of i-ZnO is debatable, it is believed that it reduces the impact of lateral inhomogeneities due to varying electrical properties of different crystallites and also prevents Al from diffusing into the absorber layer thereby avoiding shunt paths. On the other hand ZnO:Al provides the transparent conductive front contact for the solar cell. The electrical

conductivity of ZnO:Al is directly dependent on the free carrier concentration and mobility. While increasing the carrier concentration increases the free carrier absorption thus resulting in reduced transmission, increasing the mobility of the carriers is a better route to achieve improved conductivity. Examples of other window layers being investigated include In_2O_3, SnO_2, In_2O_3:Sn (ITO), etc. [14].

2.1.2.5 Metal grid

The PV cell is then usually completed by depositing a Ni-Al bilayer metal grid. A thin layer of Ni is generally used to improve adhesion of Al to the ZnO:Al window layer while Al is used for the main contact metal.

Figure 2.9 shows the complete band diagram of CIGSe solar cell at equilibrium. The band diagram is not intuitive and is somewhat intriguing. As can be seen in Fig. 2.9(a), there is an energy "spike" for electrons in the band diagram at the CIGSe/CdS interface, which should act as a barrier for electrons passing into the buffer and window layers. Seemingly one might expect that an energy "cliff" (Fig. 2.9(b)) at the CIGSe/CdS interface should be better in comparison to energy spike. This however is not supported by the experimental and theoretical results. The E_f is close to the valence band (Fig. 2.9(a)) in the bulk CIGSe region and hence a photogenerated free electron will be a minority carrier in the bulk CIGSe region. However once this free electron reaches close to the metallurgical junction, it effectively becomes a majority carrier, since E_f is closer to conduction band rather than valence band. As highlighted in section 1.2.2, the underlying principal of the working of solar cell is to make minority carriers as the

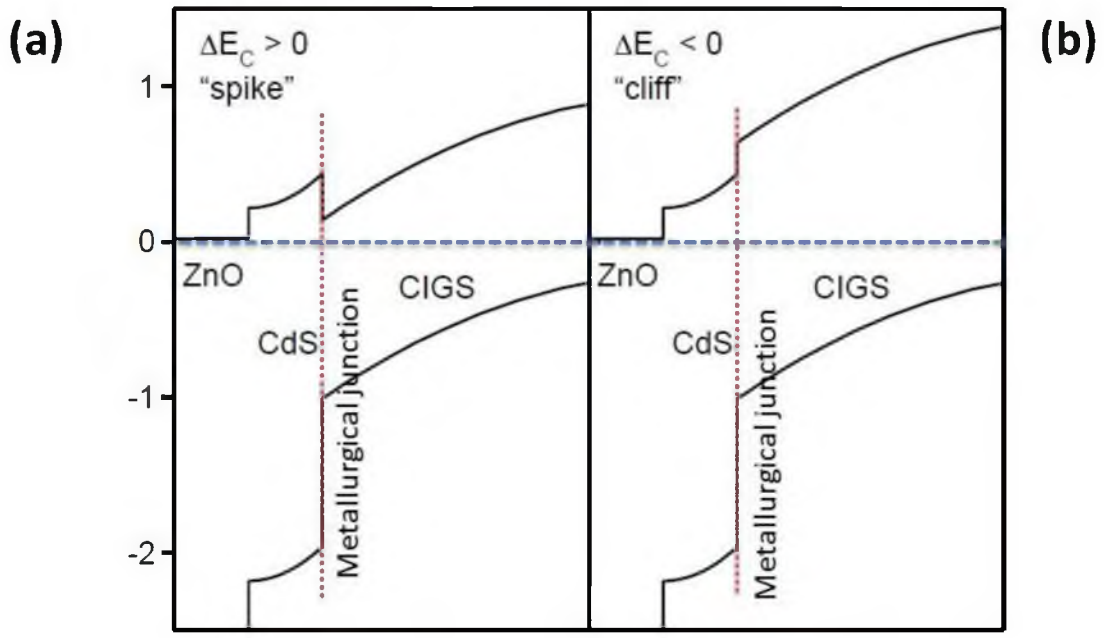

Figure 2.9: Band diagram of full solar cell stack in case of energy (a) Spike and (b) Cliff. Figure modified after Ref. [28].

majority carriers and here we realize that the minority carrier electrons become the majority carriers even before crossing the metallurgical junction. This is important because the metallurgical junction might be having a lot of surface states such as interface defects, traps and or recombination centers which would decrease the photocurrent. It has been reported that if the energy spike is greater than about 0.4 eV, collection of photogenerated electrons is impeded. However, with a smaller spike electrons can transport across the interface via thermionic emission. This however is not true in the case of the system with energy cliff. In the case of the system with energy cliff, the induced type inversion near the interface is eliminated and interface state recombination will limit V_{oc} [41].

2.2 Key comparison of chalcopyrite and kesterite materials

Since a portion of this thesis research involved the study of defects in $Cu_2ZnSn(S,Se)_4$ absorber layers, the current status of these materials is presented followed by a quick comparison between the chalcopyrite and kesterite materials.

The kesterite phase of quaternary CZT(S,Se) has attracted interest as a possible candidate for earth-abundant photovoltaic (PV) absorber layers which could be used to reduce materials costs for a large-scale PV industry producing>150 GW_P/ year of thin-film panels [42-50]. CZT(S,Se) has very similar structural and optoelectronic properties to the chalcopyrite CIG(S,Se) alloys, which are the thin-film absorber materials used in current thin-film cells with record laboratory efficiency. Figure 2.10 shows the crystal structure of CZTSe which can be derived by replacing In atoms with Zn and Sn atoms. Research and development on CZT(S,Se) is progressing at a fast rate. So far the best sulfur (CZTS) device has achieved a power conversion efficiency of 8.4% [51], the mixed CZTSSe a record efficiency of 11.1% [52] and the pure Se devices (CZTSe) have reached a maximum efficiency of 9.1% [53].

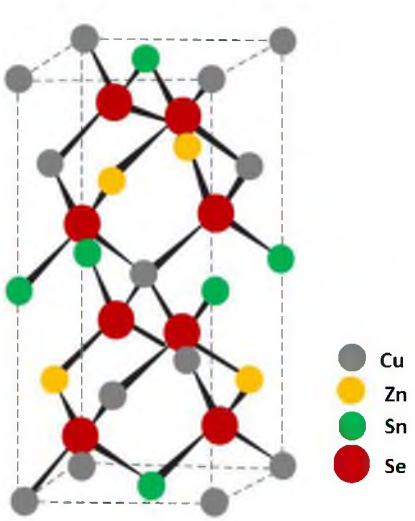

Figure 2.10: Kesterite crystal structure.

Although first-principles calculations and experimental results suggest many similarities between CIG(S,Se) and CZT(S,Se) materials, one of the key differences is the narrow range of the compositional stability of kesterite. Minor deviations from stoichiometry in CZT(S,Se) system lead to formation of secondary phases such as ZnS, SnS_2, etc. which severely limit device performance and pose a huge challenge from the materials science perspective.

Another striking difference between the chalcopyrite CIG(S,Se) and kesterite CZTS and CZTSe materials has been discussed by Romero et al. [54-55]. One of the critical aspects behind high efficiency CIG(S,Se) materials is their grain boundary physics (see section 2.1.1). Because of the Cu-depletion at the free surface and or grain boundaries, V_{Cu}^- point defects extend the acceptor band into the band gap region leading to red shift on energy scale in luminescence spectroscopy. The predicted valence band offset caused by the removal of copper atoms from the boundary leads to the formation of a neutral barrier for holes that do not otherwise impede the electron transport and reduce recombination [56-57]. This appears as a red shift of the bandgap at the grain boundaries in luminescence images of polycrystalline CIGSe thin films (see Fig. 5 in Ref. [55]). It has been established that this redshift is absolutely critical in achieving high efficiency in CIGSe and must be related to the formation of the neutral barrier [54-55]. At least to date, the kesterite CZTS does not show a clear red shift and the spatial variation in the emission spectrum is largely dominated by grain-to grain inhomogeneity possibly because of disorder and or secondary phases. On the other hand luminescence images of high-efficiency kesterite CZTSe shows similar characteristics to chalcopyrite CIGSe thus indicating that it may be more capable of producing higher-efficiency cells.

2.3 Electrochemical deposition of chalcopyrites and laser annealing theory

For this NSF sponsored project we collaborated with Dr. P.J. Dale at the University of Luxembourg. The deposition of the samples was primarily carried out by H. Meadows, a PhD student with Dr. Dale, using the electrochemical deposition method. This was followed by laser annealing of the samples at University of Utah.

The details of the exact samples prepared and used for carrying out the various laser annealing experiments is provided in Chapters 4 and 5. However, an overview of these two processes is presented in the following sections.

2.3.1 Electrochemical deposition: Basics

In electrochemical deposition, ions in the solution are assembled as atoms on the surface of the conductive back contact (Mo in this case) to form a semiconductor precursor thin film by the application of a modest voltage. Figure 2.11 illustrates the setup of electrochemical deposition (ED). Although a detailed discussion of all the factors (pH, ionic concentration, temperature, mass transport, etc.) that influence electrochemical deposition is beyond the scope of the discussion here, the underlying thermodynamic principle of electrochemical deposition is presented here.

The main components of the ED setup include working electrode, counter electrode, reference electrode and the electrolyte. An electrode is a conductor or semiconductor material in contact with an electrolytic solution. The working electrode (cathode in this case) is the one at which a desired reaction or a set of reactions are evaluated by altering the potential using a potentiostat or any other external means. The reduction of ionic species takes place at the working electrode. The counter electrode (anode in this case) is

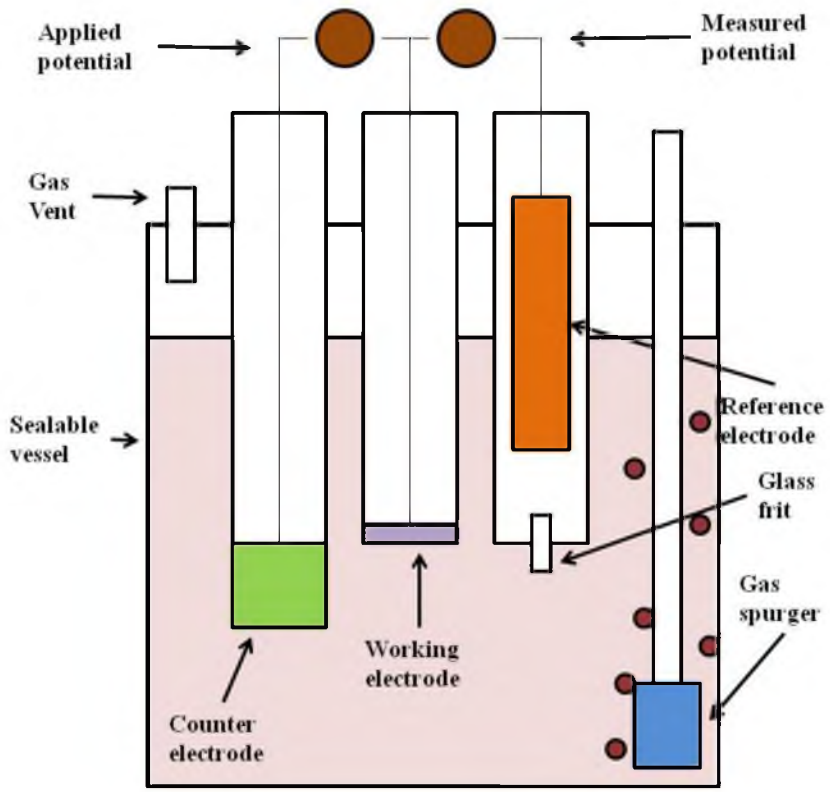

Figure 2.11: Electrochemical deposition setup.

an auxiliary electrode used to provide the current so as to counter balance the reactions taking place at the working electrode. On the other hand, the reference electrode is an electrode with constant electrochemical potential [58] and is used as a reference to which the potential of the working electrode is compared or measured against. Thus the main purpose of reference electrode is to constantly monitor the reactions taking place at the working electrode based on the sign of the voltage, so that the counter electrode could be used to supply or accept the electrons. The various reference electrodes used in practical applications include standard hydrogen electrode (SHE: E_0 = 0 V), silver chloride electrode (E_0 = +0.23 V vs SHE) etc. Here E_0 represents the standard electrode potential.

The other reference electrodes are generally preferred over SHE because of the dangers involved with H_2 evolution and its handling. It should be pointed out here that SHE is an arbitrary reference chosen for convenience, in order to compare or evaluate a set of reactions. In a sense it is similar to the vacuum level (0 eV) defined in solid state physics for evaluating junction formation and charge transfer when two dissimilar materials come in intimate contact. The SHE energy level is located -4.5 eV below the vacuum level [59]. Lastly, an electrolyte is a medium through which charge is transferred without the direct conduction of electrons. It is composed of a solvent and dissolved ionic compound/compounds that serve as the precursors for the semiconductor film that need to be deposited.

During the course of electrochemical deposition, positive ions from the electrolyte solution migrate to the cathode and there receive electrons, losing their positive charge and becoming new lower charge ions or neutral elements or molecules; this process is known as reduction. At the same time, negative ions migrate to the anode and transfer electrons to it, also becoming new lower negative charged ions or neutral elements or molecules; this process is known as oxidation. These two processes, the transfer of electrons from negative ions to positive ions, are known as an electrochemical reaction.

Now consider the following half-cell reaction:

$$M^{X+} + Xe^{-} = M \; ; \; E_0 = E^0{}_M \; V \; vs \; SHE \tag{2.1}$$

The reaction will proceed cathodically, i.e., lead to deposition of M at the working electrode, as long as the applied potential is more negative or lower than the equilibrium potential. This is true provided the activity of the involved species is unity. In the real world this is not true and we have to take into account the activity (depending on the

concentration) of the involved specie, which modifies the equilibrium potential value as per the following equation (referred as the Nernst equation [60-61]):

$$E_M = E^0{}_M - \frac{RT}{nF} \ln\left(\frac{a_M}{a_{M^{X+}}}\right) \tag{2.2}$$

where, R is the universal gas constant, T is the temperature, n is the number of electrons involved, F is the Faraday constant and a_M and $a_M{}^{X+}$ are the activities of the respective species. Now, the rate of an electrochemical reaction or the rate at which the mass is deposited at the working electrode can be determined by the Faraday's law [60-61]:

$$i = nFj \tag{2.3}$$

where, i is the current density (A/m^2) and j is the molar flux density ($moles/s\text{-}m^2$).

Now if we have to deposit a compound M_aN_b, the situation is a little different. This is because the equilibrium potential of the species M and N are dissimilar and hence when we mix the corresponding precursors, there will be superposition of the electrochemical reactions. In addition a precise adjustment of the deposition conditions is necessary to avoid excess of either M or N. This poses a big question on the potential to be used for the deposition because we need to reduce both the species M and N at the same time. The way it is usually achieved is by modifying the activity values of the corresponding species in the electrolytic solution. A complexing agent is introduced in the electrolytic solution that forms intermediate compound-complex with the ionic species of M and N. This modifies their effective activity values and bridges the gap between their equilibrium potential values. The free energy of formation of the compound M_aN_b further closes the gap between their corresponding equilibrium potentials by an amount proportional to $-\Delta G_f/XF$, where ΔG_f is the Gibb's free energy and X is the number of transferred electrons [62].

As mentioned earlier, the above discussion is based on just the thermodynamic considerations. In actual practice electrochemical deposition is a complex process and various variables (mentioned earlier) need to be optimized in order to deposit a good quality film. In addition if the specie to be deposited exhibits multiple oxidation states or the effect of the substrate on the properties of the deposited film make the problem quiet challenging. Thus for further reading, reader is suggested to study Ref. [62-67].

2.3.2 Laser annealing: Basics

The term Laser was originally an acronym meaning light amplification by stimulated emission of radiation. In nature everything follows the principle of minimization of energy, i.e., if there is an electron in a higher energy level it will fall back spontaneously to the lower energy level thus emitting a photon. This type of process is called spontaneous emission and is the basic principle behind light emitting diodes (LED). In this kind of emission the light produced is random both in space and time. However, if a photon of known energy is impinged on an electron in an excited state, the emitted photon tends to be into the identical photon state. Thus this stimulated emission is coherent and amplifies the field intensity of that mode. In a laser, a population inversion of electrons is created by pumping the gain medium with electrical or optical means and then a resonant optical cavity with one partially-transmitting mirror at the emission end is used to give each photon multiple passes through the gain medium to reinforce the desired wavelength. Such a laser works in continuous wave mode (CW; constant emission intensity vs. time).

One technique to further increase the peak power and create a pulsed output is to introduce a switchable loss or shutter into the cavity such that the population inversion in the gain medium is allowed to reach its maximum value. Then the loss or shutter is switched off, changing the finesse or quality (Q) factor of the cavity and allowing lasing to occur on nanosecond timescales, hence the name Q-switching [68, 69]. A Q-switch is typically a Pockels' cell which uses an electro-optical crystal coupled with a fixed polarizer to modulate its transmission. When the Q-switch is working (closed), some of the light leaving the gain medium does not return and hence there is no lasing as the losses exceed the gain in the cavity. This corresponds to losses inside the Fabry-Perot cavity of the laser and hence low Q-factor. At the same time population inversion keeps on building inside the gain medium. After a certain time the stored energy inside the gain medium will reach some maximum level; the gain medium is said to be saturated. At this point, the Q-switch is quickly opened, i.e., the Q-factor is changed from low to high Q thus allowing feedback to the gain medium. Because of the large amount of energy already stored in the gain medium, the intensity of light in the Fabry-Perot cavity of the laser builds up very quickly (and the stored energy in the gain medium drained quickly) and the net result is a short duration pulse of light output from the laser, with very high peak intensity. Thus, the main difference between pulsed and CW lasing is that pulsed lasing gives high peak power and low average power, while CW lasing results in high average power and low peak power.

Laser annealing of semiconductors takes place in a number of steps and involves a number of semiconductor properties [70-72]. While the optical properties of the material govern the absorption of photons in the material, the free-carrier transport and

recombination properties are also important since most of the radiation absorbed by a semiconductor goes initially into the system of mobile electrons and holes. Also, the absorption of laser radiation by a semiconductor can be substantially increased if lattice disorder and or amorphous regions are present [73-74]. Last but not the least the thermal properties such as specific heat capacity, thermal conductivity, etc., govern the flow of heat (generated) inside the material.

Consider the band diagram of semiconductor illustrated in Fig. 2.12. When a photon of certain energy impinges on a semiconductor, it can be absorbed by an electron in the valence band or an electron (hole) already in the conduction (valence) band. Thus the respective processes leading to photon absorption are; creation of an electron hole pair (band to band transition: B to B) or free carrier absorption (FCA). The FCA is dominant when $h\nu < E_{gap}$ and is stronger for longer wavelengths, while photons with $h\nu >> E_{gap}$ also induce B to B transitions, which present stronger oscillator strengths as well. In general, for efficient laser annealing, it is desirable to use laser wavelengths which lie

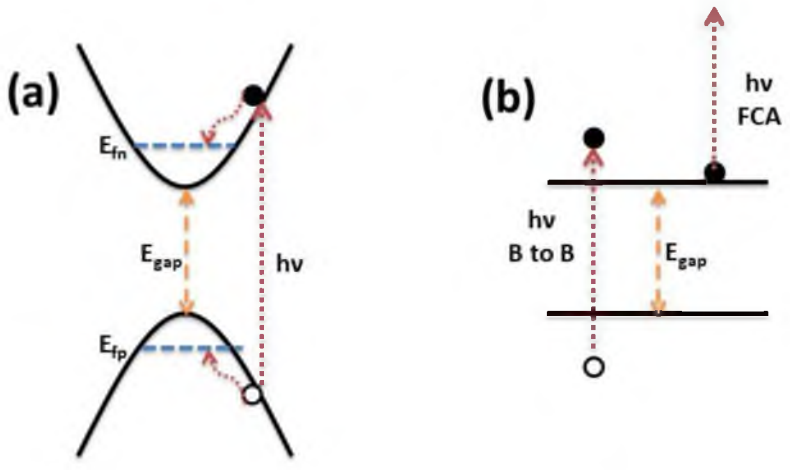

Figure 2.12: Energy absorption and release in a material system. (a) Photon absorption followed by e-h pair creation and their thermalization. (b) Band to band absorption and free carrier absorption.

within the absorption band ($h\nu >> E_{gap}$) exhibited by the material of interest. Now, if $h\nu >> E_{gap}$, the newly created e-h pair have energies in excess of the quasi-equilibrium values E_{fn} and E_{fp}, respectively. The "hot" electron and hole rapidly relax or thermalize to quasi-equilibrium state via collision to other quasi particles such as electrons/holes or phonons at time scales of $\sim 10^{-12}$ s or less. This released energy gets converted to lattice heat. This is followed by diffusion of relaxed e-h pair in the crystal; eventually leading to their recombination ($\sim 10^{-9}$ s) thus liberating more energy and heat. Another important process that could take place is the Auger recombination process, in which an electron hole pair recombines and gives its energy to an electron or hole (which becomes hot) instead of emitting a photon or a series of phonons. Eventually the hot carrier will thermalize by emitting phonons. Since Auger recombination involves an electron-hole pair and another carrier, it becomes more and more significant at high doping or high injection conditions. The inverse process in which a hot carrier thermalizes to the band edge by creating an electron-hole pair is also possible and is responsible for multiple exciton generation (MEG).

Thus to summarize we could say that for pulses or dwell times of lasers longer than the ps range, laser annealing may be understood in terms of light absorption in the material, nearly instantaneous conversion to heat, and heat flow.

In order to get an idea about the carrier generation rate, let us consider a simple calculation outlined as following. Consider photons of energy 5 eV (248 nm) from KrF laser. If the fluence is 100 mJ/cm^2, it gives us a power density of $\approx$ 8 MW/cm^2 assuming a triangular pulse with pulse width $\approx$ 25 ns. This translates into a photon flux of $\approx 1 \times 10^{25}$ photons/cm^2-s which will be absorbed within $\approx$10 nm of the surface giving an e-h pair

generation rate of $\approx 1x10^{31}$ $cm^{-3}s^{-1}$. The net change in carrier density is determined by the net recombination rate, which will include contributions from radiative, Schockley-Read-Hall, Auger, and surface recombination processes. Under these conditions a steady state electron density of about $\approx 10^{19}$ cm^{-3} could be achieved [75]. Thus a very large number of free carriers (comparable to atomic density of the material) could be generated, which mainly reduce the real part and increase the imaginary part of the refractive index of the material (see below) thus further enhancing absorption of the laser radiation (by the free-carrier mechanism primarily, which result in phonon emission but not further pair generation although some inverse Auger generation can occur).

This all happens microscopically inside the material during the course of laser annealing. What we see is the macroscopic effect in terms of heating of the material. The laser beam is an electromagnetic (EM) wave and its propagation inside the material is governed by Maxwell equations [72]. This EM wave carries energy with itself in form of flux of photons, which determine the amplitude of the associated electric field. The relevant property of the material that determines the speed of the EM wave and its decay inside the material is complex refractive index (N), which is expressed as:

$$N = n - ik \tag{2.4}$$

where n is the refractive index of the material and governs the speed of the wave inside the material and k is the extinction coefficient which governs the decay of the wave inside the material. The n and k can further be expressed as:

$$n = \frac{c}{v} \tag{2.5}$$

$$k = \frac{\alpha\lambda}{4\pi} \tag{2.6}$$

where c and v are the speed of light in vacuum and material, respectively, and α is the absorption coefficient of the material at the concerned wavelength λ. Thus simply speaking, the EM wave slows down and decays its energy inside the material thus releasing the energy it possesses which causes the material to heat.

2.4 References

[1] W. Schockley and H.J. Queisser, J. Appl Phys. 32(3) (1961) 510.

[2] W.N. Sharfarman, 34th IEEE-PVSC tutorial (2009).

[3] S.M. Sze and K.K. Ng, Physics of Semiconductor Devices, Wiley India Pvt. Ltd., Third edition, 2009.

[4] J.E. Jaffe and A. Zunger, Phys. Rev. B. 29(4) (1984) 1882.

[5] S.B. Zhang, Su-Huai Wei, A. Zunger and H. Katayama-Yoshida, Phys. Rev. B. 57(16) (1998) 9642.

[6] S. Siebentritt and U. Rau, Wide-gap Chalcopyrites, First edition, Springer Series in Materials Science, 2005.

[7] C. Stephan,S. Schorr, M. Tovar and Hans-Werner Schock, Appl. Phys. Lett. 98 (2011) 091906.

[8] Su-Huai Wei and S.B. Zhang, J. Phys. Chem. Solids 66 (2005) 1994.

[9] H.W. Schock, L. Stolt, in: H.S. Ullal, C.E. Witt (Eds.), Proceedings of the 13th NREL Photovoltaics Program Review, AIP, New York, 1995, p. 59.

[10] I.M. Ko¨tschaua, and H.W. Schock, J. Phys. Chem. Solids 64 (2003) 1559.

[11] H. Monig , Ch.-H. Fischer , R. Caballero , C.A. Kaufmann , N. Allsop , M. Gorgoi , R. Klenk , H.W. Schock , S. Lehmann , M.C. Lux-Steiner and I. Lauermann, Acta. Mater. 57 (2009) 3645.

[12] D. Schmid, M. Ruckh, F. Grunwald, and H.W. Schock, J. Appl. Phys. 73 (1993) 2902.

[13] Takayuki Negami, Naoki Kohara, Mikihiko Nishitani, Takahiro Wada, and Takashi Hirao, Appl. Phys. Lett. 67(1995) 825.

[14] R. Scheer and H.W. Schock, Chalgogenide Photovoltaics: Physics, Technology and Devices, First edition, Weinheim, Germany : Wiley-VCH, 2011.

[15] G¨odecke T, Haalboom T, Ernst F, Z. Metallkd. 91(2000) 622–634.

[16] A. Bosio, N. Romeo, A. Podestà, S. Mazzamuto, and V. Canevari, Cryst. Res. Technol. 40(10–11) (2005) 1048.

[17] S. Wagner, J.L. Shay, P. Migliorato, and H.M. Kasper, Appl. Phys. Lett. 25 (1974) 434.

[18] N. Romeo, G. Sberveglieri, L. Tarricone, and C. Paorici, Appl. Phys. Lett. 30 (1977) 108.

[19] W.E. Devaney, R.A. Michelsen, and W.S. Chen, 18th IEEE Photovoltaic Specialists Conference, IEEE Publishing, NY, (1985), p. 173.

[20] J.R. Tuttle, J.S. Ward, T.A. Berens, A. Duda, M.A. Contreras, K.R. Ramanathan, A.L. Tennant, J. Keane, E.D. Cole, and R. Noufi, Proc. Materials Research Society, San Francisco (1996).

[21] J.Y.W. Seto, J. Appl. Phys.46 (1975) 5247.

[22] P. Rai-Choudhury and P.L. Hower, J. Electrochem. Soc. 120 (1973) 1761.

[23] M.E. Cowher and T.O. Sedgwick, J. Electrochem. Soc. 119 (1972) 1565.

[24] T.I. Kamins, J. Appl. Phys. 42 (1971) 4357.

[25] E. Munoz, J.M. Boix, J. Llabres, J.P. Monico, and J. Piqueras, Solid-State Electron. 17 (1974) 439.

[26] G.L. Pearson and J. Bardeen, Phys. Rev. 75 (1949) 865.

[27] M. Gloeckler, J.R. Sites and W.K. Metzger, J. Appl. Phys. 98 (2005) 113704.

[28] M. Gloeckler, PhD Thesis Colorado State University, 2005.

[29] M. Bodegard, L. Stolt, and J. Hedstrom, in Proc 12th European Photovoltaic Solar Energy Conf., edited by R. Hill, W. Palz, and P. Helm, Stephens F, Bedford, UK.

[30] M. Ruckh, D. Schmid, M. Kaiser, R. Schaffler, T. Walter, and H.W. Schock, in Proc. 1st World Conf. on Solar Energy Conversion, p. 156, IEEE, New York, 1994.

[31] D. Rudmann, A.F. Da Cunha, M. Kaelin, F. Kurdesau, H. Zogg, A. N. Tiwari and G. Bilger, Appl. Phys. Lett. 84 (2004) 1129.

[32] D. Rudmann, G. Bilger, M. Kaelin, F.J. Haug, H. Zogg and A.N. Tiwari, Thin Solid Films 431 (2003) 37.

[33] K. Granath, M. Bodegard, L. Stolt, Sol. Energy Mater. Solar Cells 60 (2000) 279.

[34] M.A. Contreras, B. Egaas, P. Dippo, J. Webb, J. Granata, K. Ramanathan, S. Asher, A. Swartzlander, R. Noufi, Proceedings of the 26th IEEE Photovoltaic Specialists Conference, Anaheim, CA, USA (1997) 359.

[35] V. Probst, F. Karg, J. Rimmasch, W. Riedl, W. Stetter, H. Harms, O. Eibl, Mater. Res. Soc. Symp. Proc. 426 (1996) 165.

[36] T. Wada, N. Kohara, S. Nishiwaki and T. Negami Thin Solid Films 387 (2001) 118.

[37] K. Orgassa, H.W. Schock, and J.H. Werner, Thin Solid Films 431 (2003) 387.

[38] K.L. Chopra, P.D. Paulson, and V. Dutta, Prog. Photovolt.: Res.Appl. 12 (2004) 69.

[39] J. Kessler, K.O. Velthaus, M. Ruckh, R. Laichinger, H.W. Schock, D. Lincot, R. Ortega, and J. Vedel, in Proc. 6th Intern. Photovolt. Science Eng. Conf., edited by B. K. Das and S. N. Singh, p. 1005, Oxford Publ., New Delhi, 1992.

[40] T. Nakada and A. Kunioka, Appl. Phys. Lett. 74 (1999) 2444.

[41] W.N. Shafarman and L. Stolt, Chapter 13 in Handbook of Photovoltaic Science and Engineering, Edited by A. Luque and S. Hegedus, John Wiley and Sons, Second edition 2011.

[42] T.M. Friedlmeier, H. Dittrich, and H.W. Schock, Ternary and Multinary Compounds, edited by R.D. Tomlinson, A.E. Hill, and R.D. Pilkington (CRC Press, Boca Raton, 1998), p. 345.

[43] V. Fthenakis, Renew. Sust. Energ. Rev. 13 (2009) 2746.

[44] K. Zweibel, Science 328 (2010) 699.

[45] M.A. Green, Prog. Photovoltaics 14 (2006) 743.

[46] M.A. Green, Prog. Photovoltaics 17 (2009) 347.

[47] C. Wadia, A.P. Alivisatos, and D.M. Kammen, Environ. Sci. Technol. 43 (2009) 2072.

[48] H. Katagiri, K. Jimbo, W.S. Maw, K. Oishi, M. Yamazaki, H. Araki, and A. Takeuchi, Thin Solid Films 517 (2009) 2455.

[49] H. Katagiri, K. Jimbo, S. Yamada, T. Kamimura, W.S. Maw, T. Fukano, T. Ito, and T. Motohiro, Appl. Phys. Exp. 1 (2008) 041201.

[50] D.B. Mitzi, O. Gunawan, T.K. Todorov, K. Wang, and S. Guha, Sol. Energ. Mater. Sol. Cells 95 (2011) 1421.

[51] B. Shin, O. Gunawan, Y. Zhu, N.A. Bojarczuk, S.J. Chey, S. Guha, Prog. Photovolt. Res. Appl. 21 (2013) 72.

[52] T.K. Todorov, J. Tang, S. Bag, O. Gunawan, T. Gokmen, Y. Zhu, D. B. Mitzi, Adv. Mater. 3 (2013) 34.

[53] I. Repins, C. Beall, N. Vora, C. De Hart, D. Kuciauskas, P. Dippo, B. To, J. Mann, W.C. Hsu, A. Goodrich, R. Noufi, Sol. Energy Mater. Sol. Cells 101 (2012) 154.

[54] M.J. Romero,. Hui Du, G. Teeter, Y. Yan, and M.M. Al-Jassim, Phys. Rev. B 84 (2011) 165324.

[55] M.J. Romero, I. Repins, G. Teeter, M.A. Contreras, M. Al-Jassim and R. Noufi, Conference record of the 38th IEEE-PVSC 2012 proceedings, 1580 (2012).

[56] C. Persson and A. Zunger, Phys. Rev. Lett. 91 (2003) 266401.

[57] C. Persson and A. Zunger, Appl. Phys. Lett. 87 (2005) 211904.

[58] W.D. Callister Jr., Materials Science and Engineering: An Introduction, Wiley India Pvt. Ltd., Student Sixth edition, 2007.

[59] http://franklin.chem.colostate.edu/diverdi/C477/experiments/electrochemistry%20-%20cyclic%20voltammetry/references/encyclopedia_of_electrochemistry_Bard_(ed)_v6.pdf

[60] D.R. Gaskell, Introduction to the Thermodynamics of Materials, Taylor and Francis Fourth edition, 2003.

[61] M.L. Free, Electrometallurgy notes (MET E 6770 at University of Utah).

[62] T. Lincott, Thin Solid Films 487 (2005) 40.

[63] G.F. Fulop, Ann. Rev. Mater. Sci. 15 (1985) 197.

[64] E. Chassaing, J.F. Guillemoles, and D. Lincot, ECS Transactions 19(24) (2009) 1.

[65] D. Lincot, J.F. Guillemoles, S. Taunier, D. Guimard, J. Sicx-Kurdi, A. Chaumont, O. Roussel, O. Ramdani, C. Hubert, J.P. Fauvarque,N. Bodereau, L. Parissi, P. Panheleux, P. Fanouillere, N. Naghavi, P.P. Grand, M. Benfarah, P. Mogensen, O. Kerrec, Solar Energy 77 (2004) 725.

[66] C.J. Hibberd, E. Chassaing, W. Liu, D.B. Mitzi, D. Lincot and A.N. Tiwari, Prog. Photovolt: Res. Appl.18 (2010) 434.

[67] R.K. Pandey, S.N. Sahu, S. Chandra, Handbook of Semiconductor Electrodeposition, Marcel Dekker, New York, NY, 1996.

[68] http://opto.braggcell.com/index.php?MAIN_ID=106

[69] http://en.wikipedia.org/wiki/Q-switching

[70] R.T. Young and R.F. Wood, Ann. Rev. Mater. Sci. 12 (1982) 323.

[71] J.M. Poate and J.W. Mayer, Laser Annealing of Semiconductors, Academic Press, 1982.

[72] M.V. Allmean and A. Blatter, Laser-beam Interactions with Materials: Physical Principles and Applications, Springer Series, Second edition, 1994.

[73] A.G Cullis, Rep. Prog. Phys. 48 (1985) 1155.

[74] M. Bass, Laser Materials Processing, North-Holland Publishing Company, 1982.

[75] E.J. Yoffa, Appl. Phys. Lett. 36(1) (1980) 37.

CHAPTER 3

CHARACTERIZATION OF DEFECTS IN SEMICONDUCTORS

3.1 Defects in semiconductors: Basics

A defect in a crystalline semiconductor is a disturbance or divergence from a perfectly periodic crystal structure. In general defects can be classified into four major categories: point defects which involve a single lattice point (vacancies, interstitials, antisite etc.), line defects which involve a string of lattice points (screw dislocation, edge dislocation etc.), planar defects which involve a surface of lattice points (grain boundaries, stacking faults, twin planes, etc.), and voids and inclusions which are 3D volumes containing lattice dissimilarity. Figure 3.1 illustrates the various point defects.

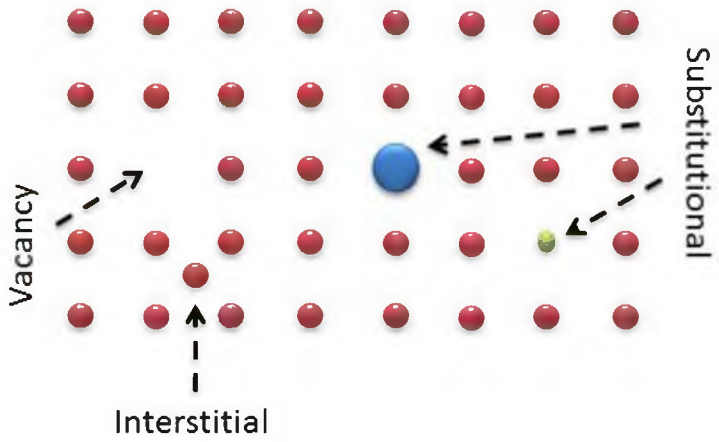

Figure 3.1: Point defects in crystal structure.

As discussed in Chapter 2, Cu-based compound semiconductors have a natural tendency to form point defects in the absence of stoichiometry. Some of these defects are shallow (small ionization energy) while some are deep (large ionization energy). Let us now discuss the implications of the shallow and deep point defects in terms of optoelectronic properties of the material.

3.1.1 Shallow level defects

As outlined earlier, shallow level defects have small ionization energy. By small the implication is the energy required to ionize the defect (set free the trapped charge carrier, i.e., hole or electron) is comparable to the thermal energy at room temperature given by $k_BT \approx 26$ meV in which k_B is the Boltzmann constant and T is taken as 300 K. Since the defect could be readily ionized at room temperature, shallow level defects do not deteriorate and or degrade the optoelectronic properties of semiconductors. In fact, the n and p-type doping of semiconductors is a direct consequence of the introduction of shallow level defects. Examples of extrinsic shallow level defects include but are not limited to P in Si, B in Si, S in GaAs, etc.

In compound semiconductors, absence of stoichiometry creates native or intrinsic defects such as vacancies, antisite etc. These native defects could be electrically charged or neutral depending on the position of Fermi level (E_f). Examples include the oxygen vacancy (V_O) in ZnO and V_{Cu} in CISe etc. These are examples of intrinsic shallow level defects. The ionization state of the defect could be decided as per Kroger-Vink notation [1-2]. For example V_{Cu} which is an acceptor type defect (0-(+1) = -1) can take up an ionization state of -1/0 and V_O which is a donor type defect takes an ionization state of

+2/0 (0-(-2) = +2). This rule could be applied to P_{Si} (+5 – (+4) = +1) also which is a donor type defect. It is important here to point out that a defect is neutral if it is occupied and gets ionized when it releases the charge carrier.

3.1.2 Deep level defects

Since the ionization energy of deep level defects is greater than several k_bT, carriers may become trapped at these localized sites for appreciable times before being thermally emitted back to their relevant band. A large ionization energy of deep levels means that the wave function of the trapped charge carrier is localized in real space and hence is de-localized in reciprocal space as per the Heisenberg's uncertainty principle [3]. Reciprocal space delocalization implies that a large number of k-values are allowed to couple with phonons and hence they have a tendency to behave as nonradiative centers [4-5]. Any type of acceptor-like or donor-like defect can trap a hole or an electron for short periods of time; the emission cross-section, thermal velocity, energy difference between the charge transition level and the respective band, and the absolute temperature determine the residence time. If the deep defect involved is close to mid-gap, then the probability of interaction of both the carrier types (holes and electrons) with the defect is approximately equal and hence nonradiative recombination can take place via the deep defect. In this process both carriers are localized at the same place and the large wave function overlap promotes rapid recombination. Thus, a deep level defect can either act as a carrier trap or a nonradiative recombination center. The net recombination rate (U), which is the difference between the recombination rate and the excess generation rate induced by a deep center, is given by:

$$U = \frac{(np - n_i^2)\sigma_p v_{th} N_t}{n + p + 2n_i Cosh\left(\frac{E_t - E_f}{k_b T}\right)} \quad (3.1)$$

where U is the recombination rate, n, p and n_i are the concentration of electrons, holes and intrinsic carrier concentration, σ_p is the capture cross-section, v_{th} is the thermal velocity, N_t is the density of the defects and E_f and E_t are the Fermi energy level and defect level, respectively. This is the reason why deep level defects should be avoided as much as possible in solar cell materials, as they severely deteriorate the optoelectronic properties of the semiconductor by reducing the number of available free carriers. It is hard to predict the exact charge transition levels an impurity atom will form, but the more different the type (s, p, d, f) and energy of the atomic orbitals of the impurity compared to the host crystal the more likely it will form a deep defect [6].

Examples of deep level defects include but are not limited to Fe_{Si} (+2/+1/0), V_{Se} (+2/+1/0) in CISe, etc. Figure 3.2 illustrates the difference between the behavior of shallow and deep level defects.

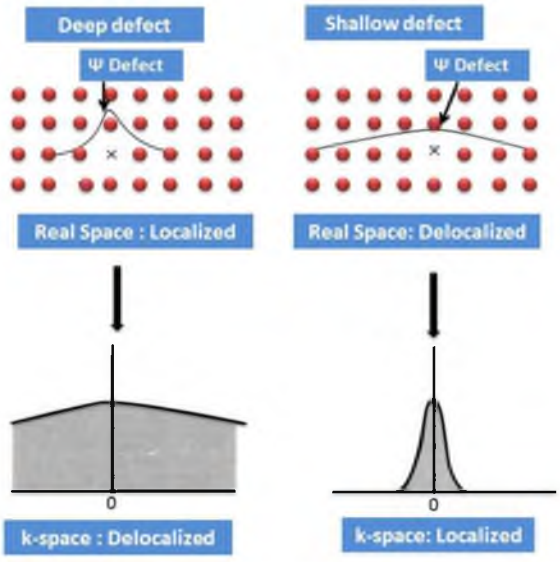

Figure 3.2: The wave functions associated with deep and shallow level defects.

Zhang et al. and Lany et al. [7-9] have calculated the charge transition energies of various point defects in CISe using first-principles self-consistent electronic structure theory. The results of their calculations are summarized in Fig. 4.14 of Ref. [10], which gives the ionization energy values of various point defects in CISe. It can be inferred from the Fig. that V_{Cu} is a shallow acceptor while Cd_{Cu} is a shallow donor. On the other hand, the behavior of V_{Se} is very complex and it can exhibit multiple ionization states and also form defect clusters with V_{Cu}.

3.2 Characterization of deep level defects in semiconductors

Although a variety of techniques such as deep level transient spectroscopy (DLTS) [11], thermal admittance spectroscopy (TAS) [12], photocapacitance and photoconductance [13-16], thermally stimulated capacitance spectroscopy [17], etc., are available to characterize deep level defects, the work in this thesis relied primarily on DLTS and TAS to characterize the behavior of defects in thin film CISe and CZTSe samples. It is important here to point out that DLTS and photoluminescence (PL) [18] are in large part complementary and best for characterizing mutually exclusive sets of defects. As mentioned in section 3.1.2, deep level defects behave either as carrier traps or nonradiative recombination centers. Neither of these behaviors results in photon emission and hence such defects cannot be characterized using PL. PL measures photon yields arising from radiative recombination transitions of photogenerated carriers either by band to band transition, shallow level defect assisted transitions etc. [19].

3.2.1 Principle of deep level transient spectroscopy (DLTS)

In general we could observe the behavior of a deep defect state by measuring capacitance, charge or current response of the device [20]. In this work we have primarily focused on the capacitance response and hence discuss the technique from the capacitance perspective.

DLTS measures the decay time of the capacitance transient occurring when the bias of a diode is changed from positive, zero or slightly negative bias to more reverse bias resulting in a change in its depletion width. An exponential transient arises when carriers are emitted from a single localized state. DLTS can be used to determine the activation energy of the dominant defect, its type, its concentration, and its capture cross-section. Let us now study the physics behind DLTS and determine how to calculate the defect related parameters mentioned above.

Consider a p-type Schottky diode in equilibrium at zero bias as shown in Fig. 3.3. If this diode is pulsed to forward bias condition (≈ few ms to tens of ms) and then its polarity is switched to reverse bias, the following things happen in sequence:

First, a sudden switch from forward to reverse bias increases the depletion width. An increase of depletion width implies the capacitance should decrease up as per the parallel plate capacitor formula (see equation 1.3).

Second, at this reverse bias some of the deep level defects that lie below E_f are still occupied by holes, while they should be ionized.

Third, this leads to emission of these trapped holes to the valence band and hence ionization of the deep defect. This increases the corresponding space charge density,

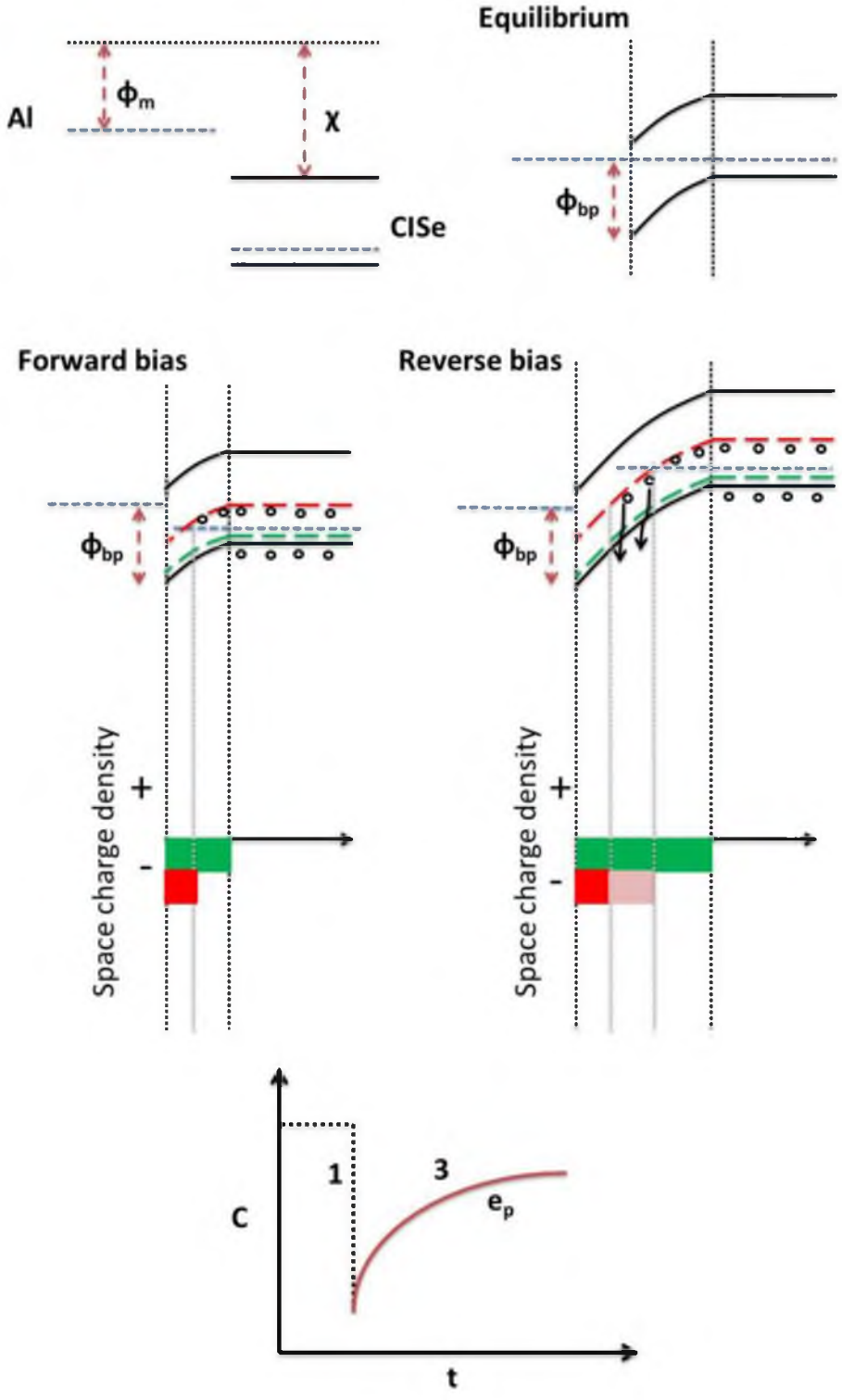

Figure 3.3: Formation of Schottky diode and principle of DLTS technique.

which decreases the depletion width and hence the capacitance rises with a characteristic time constant.

The above discussion dealt with switching the diode polarity from forward to reverse bias, i.e., conditions used for the DLTS experiments discussed in Chapter 5 and 6. However, the capacitance transient would result (as mentioned earlier) whenever a diode is brought from positive, zero or slightly negative bias to more reverse bias.

Now let us derive the equations associated with the analysis of the DLTS data and determine the parameters of the deep defect state. Consider Fig. 3.4 which shows the capture and emission of hole associated with a deep defect state at energy E_t and total density N_t (#/cm^3). Let us assume that out of the total concentration N_t, n_t (#/cm^3) is the density of states occupied by holes. Hence the density of free holes (#/cm^3) in the valence band (neglecting the concentration of intrinsic holes) is N_t-n_t. It should be pointed out that this is a valid assumption because the capacitance transient is a result of change in the space charge density brought about by deep defects only and shallow level defects do not influence it.

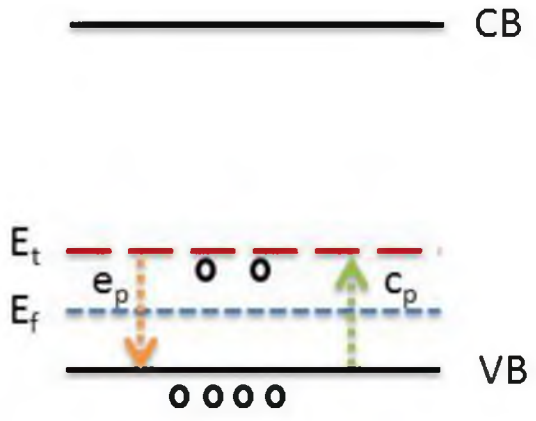

Figure 3.4: Capture and emission of holes associated with a deep level defect.

Thus the net rate of holes being emitted (#/cm^3-s) and captured (#/cm^3-s) is given by:

$$E_p = e_p n_t \tag{3.2}$$

and

$$C_p = c_p(N_t - n_t) \tag{3.3}$$

where e_p and c_p are the emission and capture coefficients of the holes with the units of inverse time (s^{-1}).

Again, the principle of detailed balance [21] requires that in a neutral material at thermal equilibrium there should be no charge accumulation. Hence:

$$e_p n_t = c_p(N_t - n_t) \tag{3.4}$$

Now, as per the Fermi-Dirac statistics [4]:

$$\frac{n_t}{N_t} = \frac{1}{1+\exp\left[\frac{(E_f - E_t)}{k_b T}\right]} \tag{3.5}$$

The capture coefficient can further be expressed by:

$$c_p = \sigma_p v_{th} p = \sigma_p v_{th}(N_t - n_t) \tag{3.6}$$

where σ_p is the capture cross-section (cm^2), v_{th} is the thermal velocity (cm/s) and p is the free hole concentration (#/cm^3) in the valence band and can be expressed by:

$$p = (N_t - n_t) = N_v \exp\left(-\frac{(E_f - E_v)}{k_b T}\right) \tag{3.7}$$

and N_v is the effective valence band density of states given by:

$$N_v = 2\left(\frac{2\pi m_{dh} k_b T}{h^2}\right)^{3/2} \tag{3.8}$$

where m_{dh} is density of states effective mass of valence band and h is the Planck's constant.

Also v_{th} is given by:

$$v_{th} = \sqrt{\frac{3k_bT}{m_p{}^*}} \tag{3.9}$$

where m_p* is the effective mass of charge carriers holes. Hence,

$$e_p = \frac{c_p(N_t - n_t)}{n_t} = \sigma_p v_{th}(N_t - n_t)\frac{(N_t - n_t)}{n_t} \tag{3.10}$$

$$e_p = \sigma_p v_{th} N_v \exp\left(-\frac{(E_f - E_v)}{k_bT}\right) \exp\left[\frac{(E_f - E_t)}{k_bT}\right] \tag{3.11}$$

Thus,

$$e_p = \sigma_p v_{th} N_v \exp\left(-\frac{E_t}{k_bT}\right) = Const.T^2 \exp\left(-\frac{E_t}{k_bT}\right) \tag{3.12}$$

Now, the capacitance transient during the course of holes emission can be expressed as:

$$C(t) = C_{oo} + C_{\infty} \exp(-t\, e_p) \tag{3.13}$$

where C_{oo} is a constant offset and C_{∞} is the steady state capacitance of the junction.

Thus if we record the capacitance transient at different temperatures and curve fit the data to extract the emission constant, we could then use equation 3.12 to determine ionization energy of the defect state. However the DLTS technique emerged at a time when computer routines were not available to curve fit the capacitance transient. Hence an alternative method to extract the information is the rate window analysis which is described as follows.

At two different time instances (defined as the rate window) during the course of single transient, we could define:

$$\Delta C = C_{\infty}\left(\exp(-t_1\, e_p) - \exp(-t_2\, e_p)\right) \tag{3.14}$$

This DLTS signal ($\Delta C/C_{\infty}$) is then plotted over a range of temperatures, with the maximum signal at a temperature where the emission rate is given by (obtained by differentiating equation 3.14 with respect to e_p and setting the differential equal to zero):

$$e_p(max)|_{\Delta t} = \frac{\ln\left(\frac{t_1}{t_2}\right)}{t_1 - t_2} \tag{3.15}$$

A peak in the plot of DLTS signal versus temperature can then be used to obtain the emission rate at the temperature of the peak. Setting the boxcar integrators to measure the DLTS signal at another two points (different Δt) during the transients and repeating the temperature scan results in an emission rate at another temperature. One temperature cycle is then required for each pair of points, T and e_p. From several temperature scans, pairs of e_p and T can be obtained and plotted on an Arrhenius plot of $\ln(e_p/T^2)$ versus 1/T based on equation 3.12. The slope of the Arrhenius plot is the ionization energy of the defect level. The intercept with the vertical axis can be used to determine the capture cross section. If the condition of full saturation of the defect level is met, its concentration could also be determined by the following expression:

$$N_t = 2\,\frac{\Delta C}{C_\infty}\,(N_{net}) \tag{3.16}$$

where N_{net} is the net average free carrier concentration.

The important thing to be kept in mind is the sign of the capacitance transient as the sign indicates whether a majority carrier defect or a minority carrier defect is being measured. Based on the above discussion we can conclude that for a majority carrier related defect the capacitance transient will be negative, as shown in Fig. 3.3. This is true irrespective of the type of conductivity of the samples, i.e., whether a p-type or n-type sample is being measured.

3.2.2 Principle of minority carrier deep level transient spectroscopy (MCDLTS)

As discussed in Chapter 1, the minority carrier transport is important for the optimal performance of a photovoltaic cell and hence there is a need to study the defects associated with the minority carriers (electrons in this case). However, the minority carrier behavior is more difficult to measure than the majority carrier parameters. One way to obtain information about minority carrier defects in a p-n junction is by applying an injecting (forward bias) pulse and then observing the capacitance transient. However because both types of carrier are present the minority carrier occupancy is uncertain which presents difficulties for quantitative measurements of concentration unless $\sigma_{min} >> \sigma_{maj}$ [22].

A better method for studying minority carriers is minority carrier DLTS (MCDLTS) which is a variant using light biasing in place of voltage bias and was introduced by Brunwin et al. [23]. This technique is mainly used to characterize the deep level defects associated with the minority carriers. In MCDLTS, the sample is held under reverse bias during the entire measurement and above bandgap light is pulsed on the sample to generate electron-hole pairs. The electric field in the depletion region excludes majority carriers, and the photogenerated minority carriers created within a diffusion length from the depletion region boundary may then enter the depletion region and be available for capture.

Again, consider the p-type Schottky diode under reverse bias as shown in Fig. 3.5 (a) and 3.5 (b). Under this condition in the dark, it is under steady state, which is obviously different from the steady state under equilibrium (zero bias). Two cases are possible as

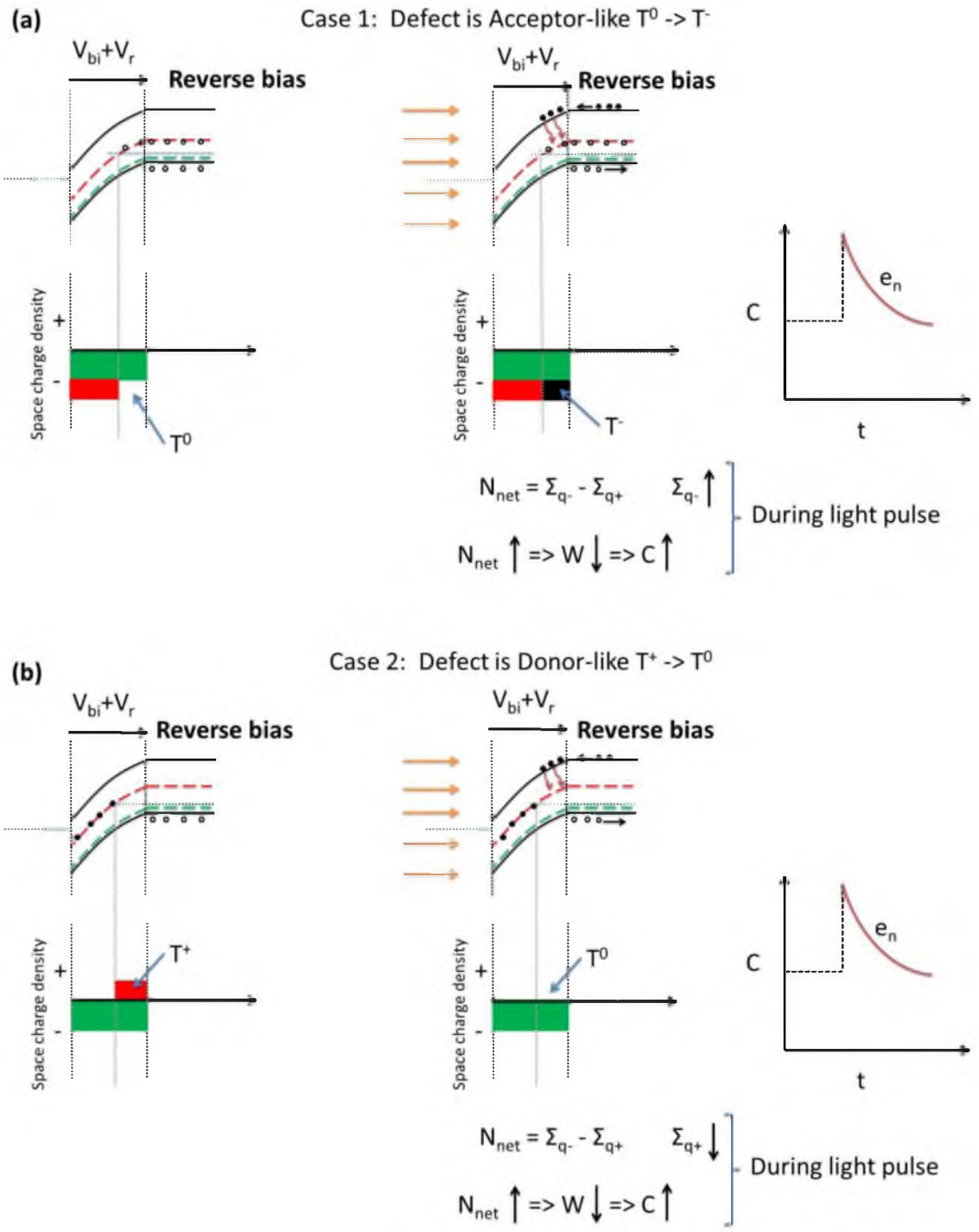

Figure 3.5: Principle of MCDLTS technique: (a) Acceptor like neutral defect and (b) donor like ionized defect.

presented in Fig. 3.5(a) and 3.5(b) which might give a capacitance transient corresponding to minority carrier defect state. The steps of MCDLTS are as follows:

First, light above band gap energy is pulsed on the diode held under reverse bias condition.

Second, this generates e-h pairs all over the diode. Holes being the majority carriers cannot enter the depletion region because of the huge barrier presented by built-in voltage and the reverse bias. However, photo generated electrons (on p-side) within diffusion distance experience an electric field that forces them into the depletion region. Hence, the free electrons within diffusion length distance from the space charge boundary can enter the depletion region.

Third, once the minority carrier electrons enter the space charge region, two scenarios are possible:

(a) Electrons get captured by neutral defect states previously occupied by holes. If this happens, it increases the net space charge density, as there is an increase in the net negative charge. This decreases the depletion width which increases the capacitance. This whole action takes place during the course of light pulse. When the light is switched off, the diode would go back to its original quasi equilibrium condition. This will lead to emission of trapped electrons and hence a corresponding decrease in the space charge density or an increase in depletion width or a decrease in capacitance. Thus a positive capacitance transient is observed in this case.

(b) The other possibility is that minority carrier electrons are captured by positively-charged defect states, making them less positive. If this happens, during the course of light pulse the net space charge density will again increase, however this

time due to decrease in the net positive charge. This again decreases the depletion width or increases the capacitance. When the light is switched off, the diode would go back to its original quasi equilibrium condition. This will lead to emission of trapped electrons and hence a corresponding decrease in the space charge density or an increase in depletion width or a decrease in capacitance. Thus a positive capacitance transient could be observed in this case too.

The remaining procedure of MCDLTS is similar to DLTS and the data collected are analyzed in a similar fashion to DLTS, the main difference being that the defect energy E_t in this case will be measured from conduction band and also one has to use effective mass of electrons and effective density of states for conduction band.

3.2.3 Principle of thermal admittance spectroscopy (TAS)

TAS involves measuring the junction capacitance as a function of the frequency of a small AC bias signal and temperature. The capacitance of the depletion region is given by equation 1.3. However equation 1.3 was derived assuming complete ionization (shallow defects). In the presence of deep defects, the band bending in the depletion region causes the Fermi level to cross the deep defect level at some distance (crossover point) from the interface as discussed earlier (see Fig. 3.3). Now, if a small AC voltage (10's of mV) with oscillating frequency ω is superimposed on the DC bias and applied to the junction, it causes the electric charge accumulated by traps to oscillate in the vicinity of crossover point. The trapped electric charge follows the applied voltage oscillations and contributes to the total capacitance only if their frequency does not exceed the characteristic trap frequency ω_t, which is related to emission coefficient e_p by:

$$\omega_t = 2\pi e_p \tag{3.17}$$

Thus the junction capacitance in presence of a single deep defect level can be expressed as [24]:

$$C(\omega) = C_{depletion} + C_{deep\ defect} \tag{3.18}$$

The depletion capacitance usually corresponds to high frequency capacitance (~ MHz) and the capacitance at low frequency (~ 10's to 100's of Hz) has a contribution from deep defects as well. Hence if capacitance is plotted vs. applied AC frequency the capacitance decreases with increasing frequency, with an inflexion point (step) stationed in between high and low frequencies. The frequency at the inflexion point (f_i) corresponds to e_p at the particular temperature from a set of C-f-T data. The inflexion frequencies for corresponding temperatures are then determined from the maxima of the quantity -f(dC/df) plotted as a function of f (which will yield a peak). The set of (f_i,T) values form the input values for equation 3.12 and again the activation energy of the defect state could be determined from the modified Arrhenius expression given by equation 3.12.

As per the above discussion, it is reasonable to state that the volume concentration of an isolated trap state can be estimated by:

$$N_t \propto \ ({C_{lf}}^2 - {C_{hf}}^2) \tag{3.19}$$

Walter et al. [25] have derived a more rigorous solution to the above formulation in order to calculate the concentration of defect states across the band gap of the semiconductor. The expression for this calculation is:

$$N_t\,(E_\omega) = -\frac{1}{k_b T}\,\omega\,\frac{dC}{d\omega}\,\frac{V_{bi}}{qw} \tag{3.20}$$

in which E_ω corresponds to the activation energy in equation 3.12.

The application of DLTS, MCDLTS and TAS to characterize defects in Cu based photovoltaic films will be discussed in Chapter 5 and Chapter 6.

3.3 References

[1] F.A. Kröger, The Chemistry of Imperfect Crystals, North-Holland, Amsterdam, and Wiley, New York, 1964.

[2] F.A. Kröger, and Vink, H.J. in Solid State Physics (edited by F. Seitz and D. Turnbell) 3, 307, Academic Press, New York, 1956.

[3] S.O. Kasap, Principles of Electronic Materials and Devices, Tata McGraw-Hill Publishing Company Limited, Third edition, 2008.

[4] S.M. Sze and K.K. Ng, Physics of Semiconductor Devices, Wiley India Pvt. Ltd., Third edition, 2009.

[5] http://pveducation.org/pvcdrom

[6] A. Rockett, Tutorial on Materials, Defects, and Characterization Methods for Photovoltaics, IEEE PVSC 33rd Conference (2008).

[7] S.B. Zhang, Su-Huai Wei, A. Zunger and H. Katayama-Yoshida, Phys. Rev. B. 57(16) (1998) 9642.

[8] S. Lany, and A. Zunger, J.Appl. Phys. 100 (2006) 113725.

[9] S. Lany, Y.J. Zhao, C. Persson and A. Zunger, Appl. Phys. Lett. 86 (2005) 42109.

[10] R. Scheer and H.W. Schock, Chalgogenide Photovoltaics: Physics, Technology and Devices, First edition, Weinheim, Germany : Wiley-VCH, 2011

[11] D.V. Lang, J. Appl. Phys. 45(7) (1974) 3023.

[12] D.L. Losee, Appl. Phys. Lett. 21 (1972) 54.

[13] J.D. Cohen, T. Unold, A.V. Gelatos, and C.M. Fortmann, J. Non-Cryst. Solids 141 (1992) 142.

[14] A.V. Galatos, K.K. Mahavadi, . D. Cohen and J.P. Harbison, Appl. Phys. Lett. 53(5) (1966) 403.

[15] V. Ramanathan, T. Datta, and R. Noufi, Appl. Phys. Lett. 51(10) (1987) 746.

[16] M. Igalson and A. Urbaniak, Bull. Pol. Acad. Sci-Te. 53 (2005) 157.

[17] C.T. Sah and J.W. Walker, Appl. Phys. Lett. 22 (1973) 384.

[18] A. Bauknecht, S. Siebentritt, J. Albert, and M. Ch. Lux-Steiner, J.Appl. Phys. 89 (2001) 4391.

[19] S. Siebentritt and U. Rau, Wide-gap Chalcopyrites, First edition, Springer Series in Materials Science, 2005.

[20] D.K. Schroder, Semiconductor Material and Device Characterization, Third edition, Wiley-Interscience, 2006.

[21] W. Schockley and H.J. Queisser, J. Appl Phys. 32(3) (1961) 510.

[22] http://www.icds2011.com/docs/DLTS_tutorial_ICDS.pdf

[23] R. Brunwin, B. Hamilton, P. Jordan and A.R. Peaker, Electron. Lett. 15(12) (1979) 349.

[24] Y. Zohta, Solid State Electron, 16 (1973) 1029.

[25] T. Walter, R. Herberholz, C. Muller and H.W. Schock., J. Apply. Phys. 80 (1996), 4411.

CHAPTER 4

LASER ANNEALING OF as-ELECTRODEPOSITED CHALCOPYRITE FILMS

4.1 Background and motivation

$Cu(In,Ga)(Se,S)_2$ (CIGSeS) is one of the leading inorganic absorber layers for thin film photovoltaic technology. It offers a number of desirable properties such as a direct band gap tunable from ≈ 1.04-1.68 eV, very high optical absorption coefficient ($\alpha \approx 10^4$ /cm) and low surface recombination velocity, to name a few. Over the years CIGSe technology has emerged from the laboratory with industrial module efficiency reaching close to 16% [1] and champion cells in laboratory exceeding 20% [2]. However in order to expand the CIGSe photovoltaics market and approach the desired $0.50/Watt, a production method which is fast, cost-effective, reliable, scalable, and not energy intensive but which at the same time maintains the high efficiency of CIGSSe devices is of paramount importance. These challenges have motivated us to attempt to synthesize device-quality CIGSSe material from a process which couples rapid nonvacuum but low-crystalline quality deposition (electrochemical deposition) followed by high temperature laser annealing.

Electrochemical deposition offers attractive characteristics for large area, low cost, low temperature and soft processing of materials [3]. Compared to vacuum deposition, it

has the advantages of requiring only a small amount of energy, allowing fast depositionrates ~20 μm/hr [4], and effective material utilization. Recently, one of the photovoltaic manufacturers has scaled up the electrodepositon of CIGS by selenization of electrodeposited elemental stacks [5]. However the biggest disadvantage is that as-electrodeposited (ED) thin film semiconductors are not useful in devices and thermal annealing is required to form the desired semiconductor phase, to improve crystallinity, and to minimize structural and electronic defects [6].

Laser annealing is advantageous over furnace annealing and or rapid thermal annealing (RTA), as it could be used for selective heating of different layers or depths within a sample, i.e., annealing the semiconductor absorber layer effectively while minimizing the thermal budget of the substrate by choosing the correct laser wavelength and dwell time. Since the heat capacity of the semiconductor thin film (≈ 1 μm) is negligible as compared to the thick glass substrate (≈ 2-3 mm), it could result in the use of less total energy to achieve a given annealing process. Lasers today are being used for selective emitter doping of c-Si solar cells and line beams up to 750 mm wide are the enablers of the thin Si recrystallization on glass critical for thin film display technologies. These applications, which laser anneal the entire area as opposed to, e.g., laser scribing of monolithically integrated thin film photovoltaic (TFPV) modules, thus indicating viability of current technologies towards laser annealing in CIGSeS TFPV production.

Hence the motivation behind this work is to reduce the overall annealing time and thermal budget for small areas as compared to typical furnace annealing and RTA processes. There has been some work reported by different groups [7-12] which were marred with problems like thermal cracking, oxide formation, dewetting, etc. Hence we

believe that this work sheds some light on the laser annealing of CISe and help develop the annealing process.

4.2 Experimental details

4.2.1 Sample synthesis and preparation

CISe thin films with Cu-poor (Cu/In<1) and Cu-rich (Cu/In>1) stoichiometry were electrodeposited from a single bath on Mo coated soda lime glass substrates at University of Luxembourg. The precursors for the Cu, In and Se atoms are $CuCl_2$, $InCl_3$ and H_2SeO_3. For details involved in sample preparation, the reader is suggested to go through Ref. [6, 13] . The deposition was carried out for varying times of 60 and 30 min giving an average thickness of ≈ 1000 nm and ≈ 600 nm, respectively. The 1" x 1" as-ED (as-electrodeposited) samples were cut into 6 mm x 6 mm samples at University of Utah followed by laser annealing.

Pulsed laser annealing (PLA) was carried out using a KrF excimer laser (λ =248 nm and $\tau \approx$ 25 ns) and a solid state Nd:YAG (Neodymium-doped Yttrium Aluminum Garnet) laser (λ = 1064 nm and $\tau \approx$ 75-150 ns). On the other hand continuous wave laser annealing (CWLA) was carried out with solid state Nd:YAG laser (λ = 1064 nm) only. Figure 4.1 shows the setup of 1064 nm laser.

The samples were held in an annealing chamber with a quartz front window and purged with flowing Ar gas to provide an inert atmosphere and suppress oxidation. For the annealing experiments with 1064 nm laser, an aperture of 2x2 mm size was used in front of the sample and multiple spots were tiled to cover the entire sample surface. Varying annealing conditions of fluence (mJ/cm^2) and power densities (W/cm^2) and

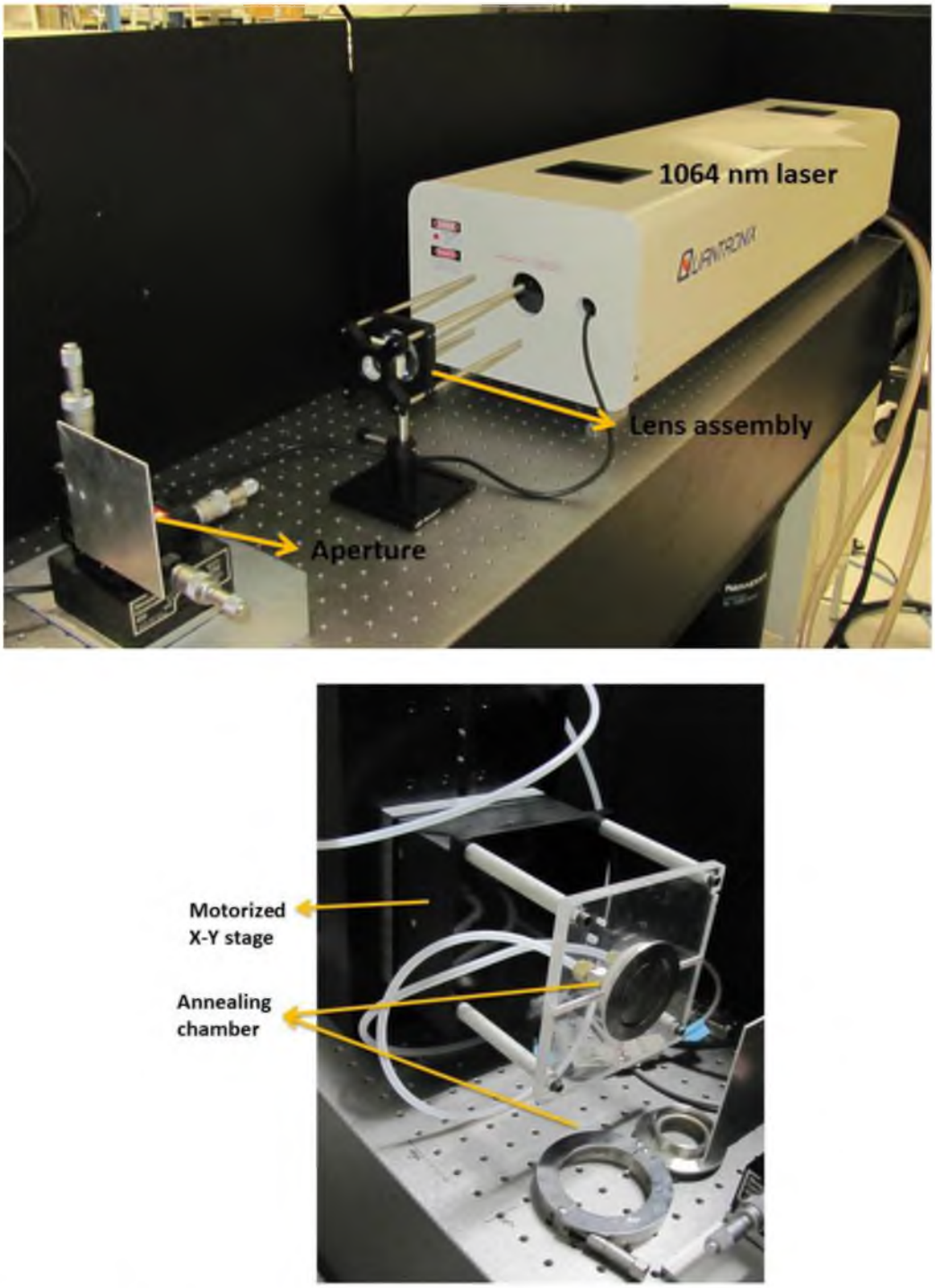

Figure 4.1: Nd:YAG laser setup and the annealing chamber.

annealing time were tested (as will be discussed later) so as to determine the optimal annealing parameters. A computer controlled mechanical shutter was used to control the exact annealing time.

4.2.2 Characterization

Scanning electron microscopy (SEM) was used to investigate the surface morphology and energy dispersive x-ray (EDS) analysis at an acceleration voltage of 15 kV was used to determine the bulk composition of the CISe films. X-ray diffraction (XRD) measurements (θ-2θ) were carried out using $Cu_{K\alpha}$ radiation (λ = 1.54056 Å) in a range varying from 2θ = 20°-60° in a Bragg-Brentanno focusing geometry. Raman spectra were obtained with 532 nm laser excitation from a spot size of 2 μm within a 20 μm laser-illuminated area on the sample using a confocal optical microscope.

4.3 Results

4.3.1 PLA of as-ED CISe films (Cu-poor, 1000 nm thick)

4.3.1.1 PLA using 248 nm laser

PLA of as-ED CISe films was carried out with the 248 nm excimer laser at varying fluence from 30 mJ/cm^2 up to 500 mJ/cm^2. The number of pulses used was 1, 5 or 25. Figure 4.2 shows the SEM images of the as-ED and PLA samples. As can be seen in the figure, no changes in the surface morphology are observed for fluence < 50 mJ/cm^2. However at fluence ≥ 50 mJ/cm^2, the CISe film starts to melt and completely dewets at about 100 mJ/cm^2. The full dewetting must occur within 200 ns after laser pulse, as

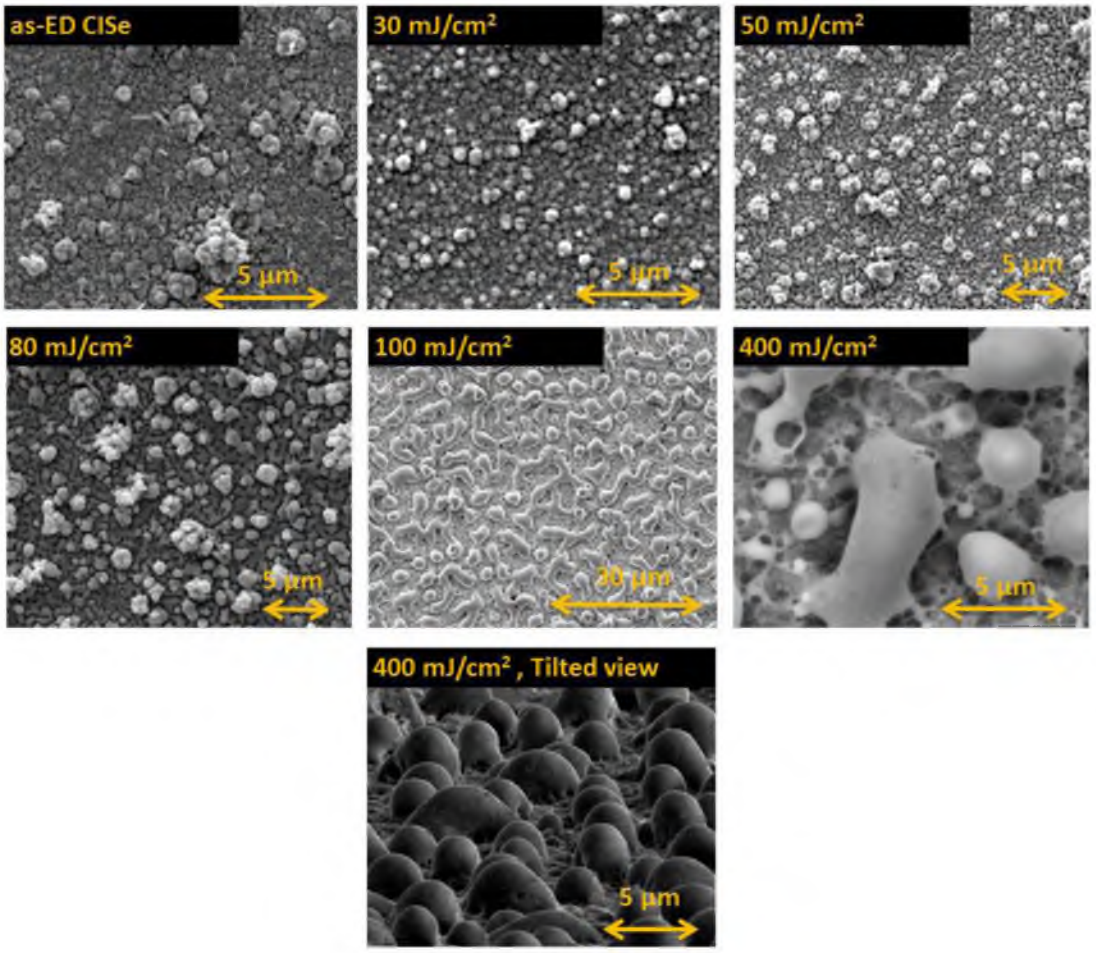

Figure 4.2: SEM images of as-ED and PLA CISe films on Mo using 248 nm laser.

suggested by temperature estimates on furnace annealed CISe films (see Chapter 5). While XRD results (Fig. 4.3) at low fluence show no improvement in crystallinity , a reduction in full width at half maximum (FWHM) of the XRD peaks for the samples annealed at $\geq$100 mJ/cm^2 is observed. However these films are not suitable for PV applications because any attempt to synthesize a PV device would result in short circuiting of the cell.

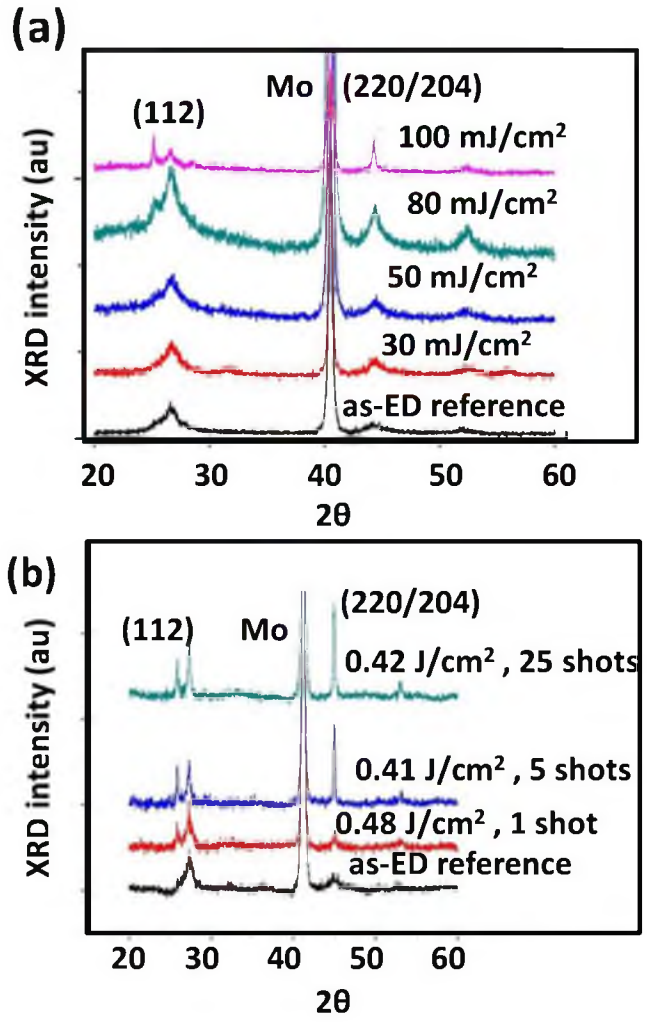

Figure 4.3: XRD data of as-ED and PLA CISe films on Mo using 248 nm laser.

Since CISe films annealed at high fluence dewet on Mo, interfacial energy was changed by depositing the CISe films on top of Mo, which was furnace annealed in Se atmosphere so as to yield $MoSe_2$ as the back contact. These films were further annealed under high fluence conditions. However, dewetting was observed for these films too (Fig. 4.4), suggesting that interfacial energy did not change significantly.

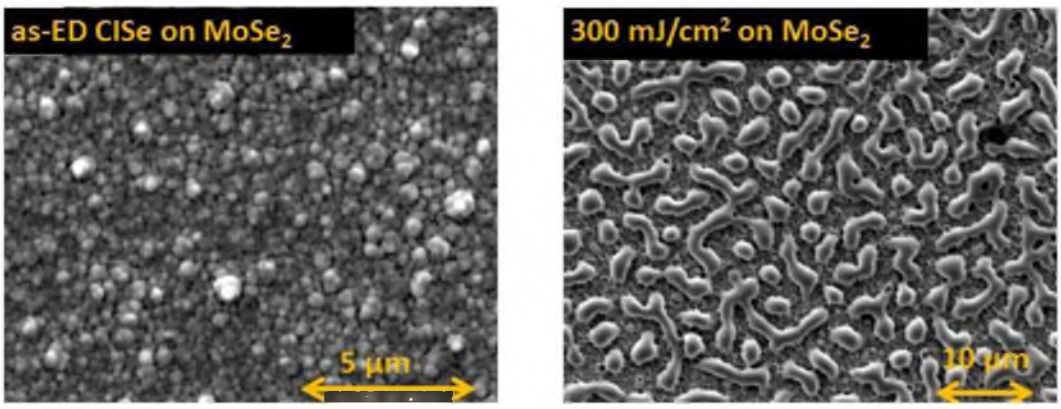

Figure 4.4: SEM images of as-ED and PLA CISe films on $MoSe_2$ using 248 nm laser.

4.3.1.2 PLA using 1064 nm laser

Since liquid phase CISe dewets on Mo and $MoSe_2$, thus the substrate was changed to Cu, again in an attempt to change interfacial energy and avoid dewetting. Figure 4.5 shows the SEM image of the sample that underwent PLA at 100 mJ/cm^2 and was exposed to 5 laser pulses at 10 Hz. For comparison, SEM image of a similar CISe film on Mo annealed under same conditions is shown. As can be seen from the figures, unfortunately changing the substrate to Cu also did not help in prevention of dewetting.

Hence an attempt was made to work in the submelting regime but for longer times and total numbers of pulses so as to avoid dewetting but at the same time reach high enough temperatures for long enough to drive long range atomic diffusion. Since 1064 nm laser has a larger optical absorption depth (inversely related to absorption coefficient; see Chapter 1, 2, see Fig. 4.6), it will help in heating the CISe film more uniformly in comparison to 248 nm laser. Various CISe films underwent PLA at 50, 60 and 70 mJ/cm^2. The number of laser pulses was also varied up to 1000 and frequency varied up to 400 Hz. Figure 4.7 (a) and (b) show the SEM images of (respectively) an as-ED CISe

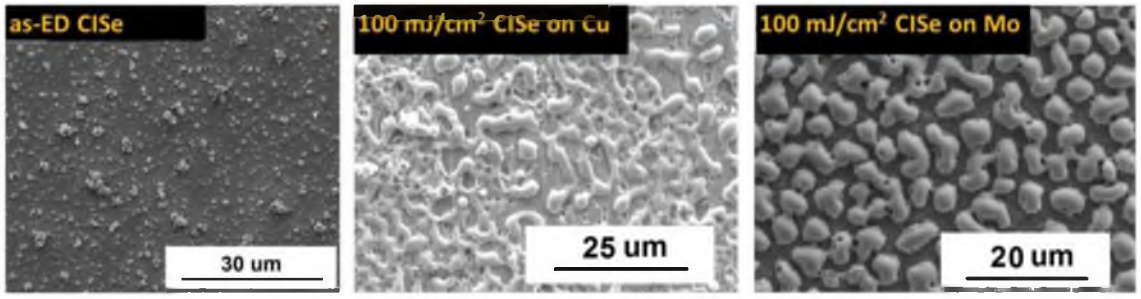

Figure 4.5: SEM images of as-ED and PLA CISe films using 1064 nm laser.

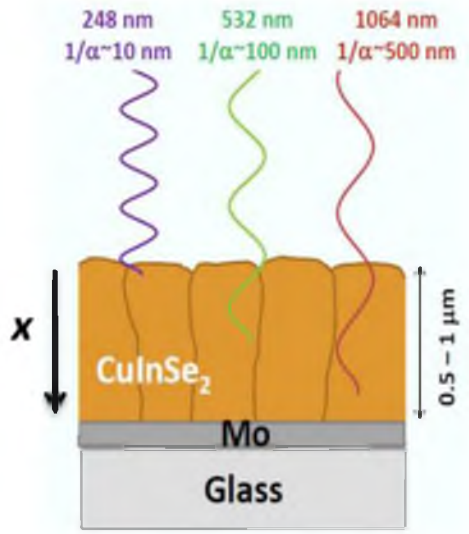

Figure 4.6: Comparison of optical absorption depth in CISe for lasers with varying wavelengths.

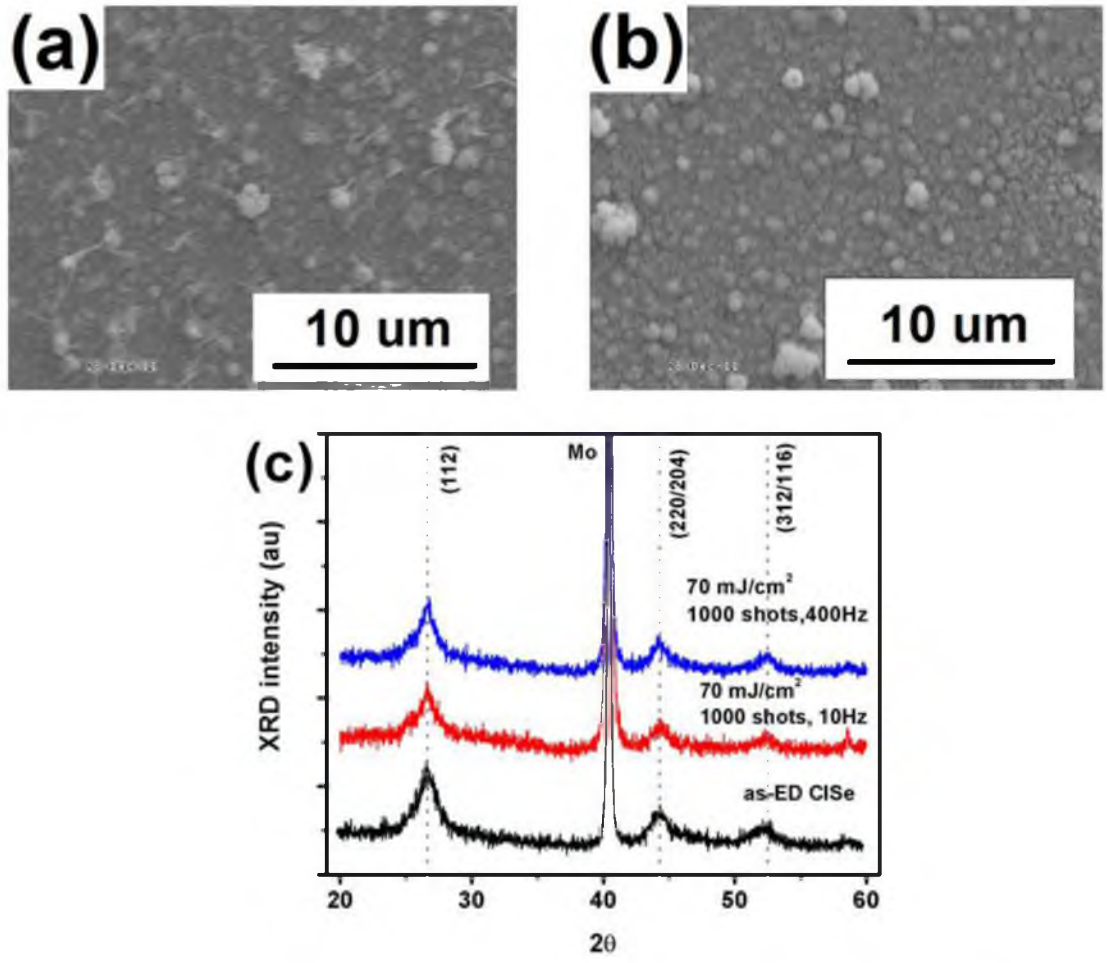

Figure 4.7: SEM images of (a) as-ED CISe ref film, (b) PLA at 70 mJ/cm^2 for 1000 pulses at 400 Hz and (c) shows XRD scans of as-ED CISe films and samples that underwent PLA at 1064 nm, 70 mJ/cm^2 for 1000 pulses at 10 Hz and 400 Hz.

film and a film that underwent PLA at 70 mJ/cm^2 for 1000 pulses working at 400 Hz. As can be seen from the figure there is no sign of melting, but counter to the purpose of the experiment no improvements are seen in XRD results of the films (Fig. 4.7(c)).

These results prompted us to think carefully about the PLA process. The atomic diffusion length can be estimated as $\approx\sqrt{D(T)t}$ in which D is the diffusion coefficient which is a function of temperature (T) and t is the time of annealing. Now, in order to

increase the atomic diffusion length, i.e., to improve crystallinity of $CuInSe_2$ system we could either increase D(T) or t.

In the case of electrodeposited $CuInSe_2$ on a Mo back contact, increasing T beyond T_{melt} results in dewetting of $CuInSe_2$. Electron back scatter diffraction (EBSD) data [14] revealed that dewetted $CuInSe_2$ droplets sit on top of Mo. These droplets have an amorphous shell with the recrystallized grains in the core. The amorphous shell could be overcome by using slower pulses, but the gathering up of the $CuInSe_2$ into droplets will be present for any conditions producing a melt for long enough time for viscous flow to occur. If it is made faster so that the liquid solidifed before droplet formation, then we face another problem of amorphous solidification. So the conclusion is that there is no process window at all, unless the interface energetics are changed. However as discussed earlier changing the substrate to $MoSe_2$ or Cu also did not solved the dewetting problem. Although there exists a possibility of trying out liquid phase $CuInSe_2$ recrystallization using other suitable back contact layers such as W, Ta, etc. [15].

The other approach to increase crystallinity will be to work under the sub-melting regime ($T < T_{melt}$). As discussed earlier working in sub-melting regime also did not help in improving crystallinity of the samples. This is because of the constraint imposed by t which is < 150 ns and is probably not large enough for long range diffusion. It should be pointed out that the long range diffusion simply means an annealing process which gives an increase in X-ray coherence length by about 10 times, i.e., approximately from 7 nm to 70 nm. These estimates are based on Scherrer's formula [16] applied to as-ED and furnace annealed CISe [6, 17-18] samples. The reason behind no appreciable improvements in X-ray coherence length is simple to understand. The work frequency of

laser beam during the experiments is varied from 10 Hz to 400 Hz which is equivalent to a minimum of 2.5 ms, about five orders of magnitude greater than the pulse width. This implies that the each pulse that $CuInSe_2$ film is exposed to (either 5 or 1000) is acting independently of each other resulting in noneffective long range diffusion. One of the possible but difficult way to counter this would be to work with a laser system which can possibly work at MHz and still deliver high energy laser pulses to drive long range atomic diffusion in submelting regime.

The other possibility that exists and we have used is to increase the annealing time by switching from PLA mode to CWLA mode. In CWLA, the sample can be held at an elevated temperature for longer times which can allow for sufficient diffusion to occur without exceeding the melting temperature.

4.3.2 CWLA of as-ED Cu-poor and Cu-rich films using 1064 nm laser

Two kinds of samples with Cu-poor (Cu/In < 1) and Cu-rich (Cu/In > 1) stoichiometry underwent CWLA using 1064 nm laser at ≈ 50 W/cm^2. The thickness of both kinds of samples was ≈ 500 nm. Figure 4.8 (a) and (b) show the SEM images of the Cu-poor and Cu-rich as-electrodeposited reference samples, respectively. As can be seen, both of the films have granular structure with a sparse layer of tall features protruding from the films' surface and appear to be quite similar irrespective of the initial Cu-content. However, Cu-rich films appear to be more compact in plane but also nonuniform with protrusions. There is no apparent change detectable by SEM in the respective surface morphology of the samples even after CWLA for up to 45 s (Fig. 4.8

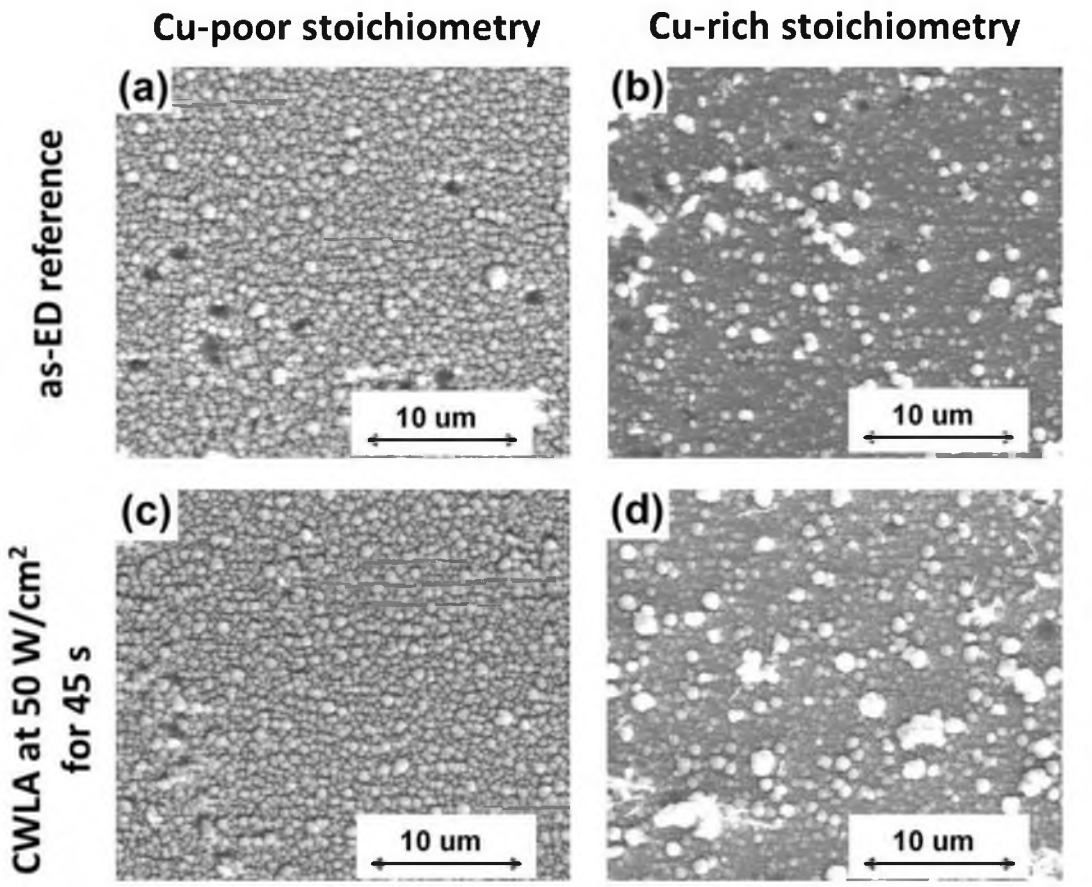

Figure 4.8: SEM images of Cu-poor and Cu-rich samples in the as electrodeposited state (as-ED) and after CWLA at 50 W/cm^2 using 1064 nm laser. The Cu-rich and Cu–poor films have somewhat different surface morphology and no apparent changes result from CWLA.

(c) and (d)). This lack of apparent change in surface morphology is consistent with the results of furnace annealed samples [6]. Thus from the SEM images we can infer that no melting and/or dewetting occurred during the course of CWLA and the annealing takes place in complete solid phase mode.

EDS measurements of the samples (Fig. 4.9 (a) and (b)) clearly show the difference in the composition of Cu-poor and Cu-rich samples before and after CWLA. The literature on CIGSe suggests that an overall Cu-poor stoichiometry results in the champion

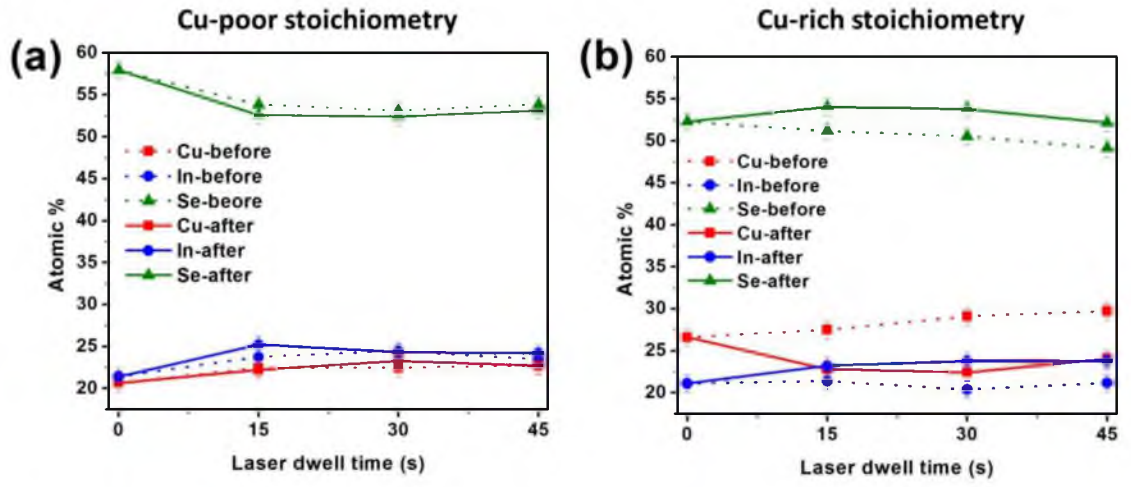

Figure 4.9: Composition of (a) Cu-poor and (b) Cu-rich samples as measured by EDS after CWLA for varying times at 50 W/cm^2 using 1064 nm laser. Dotted lines represent composition of the films before KCN etching while solid lines show the composition after KCN etching. The Cu-poor films do not change significantly after KCN etching, while the Cu-rich films go from Cu-rich to Cu/In ≈1 (within estimated uncertainty).

efficiency cells [2]. This is interesting from research point of view also because although Cu-poor chalcopyrites end up with higher efficiency they are characterized by a high degree of compensation, lower mobilities, and a higher degree of space charge recombination [19]. On the other hand Cu-rich samples tend to have lower compensation and better transport properties such as higher mobility but are limited by recombination at the interface [19]. Also the presence of highly conductive Cu_xSe_y phase in case of Cu-rich samples, could end up in short circuiting the solar cell device. The Cu_xSe_y phase is generally etched off using KCN solution, and the etching has been done for these samples. While the Cu-poor samples do not show much change in the composition after KCN etching (Fig. 4.9(a)), as expected the Cu/In ratio in Cu-rich samples reduces to ≈ 1 after KCN etching (Fig. 4.9(b)). The samples are also observed to become progressively Se-poor as the CWLA time increases (Fig. 4.9 (a) and (b)). The Se-poor films will have

Se vacancies (V_{Se}) which are known to severely restrict cell efficiency. The V_{Se} can either induce a deep donor defect state (0/+) or form a defect complex with Cu vacancy (V_{Se}-V_{Cu}). This defect complex is amphoteric in nature and possess multiple ionization states and is known to be metastable in nature [20, also see Chapter 3]. Thus, incorporation of additional processes or the modification of the laser step to suppress Se loss will be critical for use of CWLA in actual cell processing.

Figure 4.10(a) and (b) show the XRD (θ-2θ) scans for Cu-poor and Cu-rich samples respectively. As can be seen from the Fig. 4.10, the as-ED reference samples have a broad (112), (220/204) and (312/116) diffraction peaks. This indicates the nano-crystalline nature of as-ED reference samples. After CWLA all of the diffraction peaks become both narrower and more intense, indicating improved crystalline quality. This is because a longer X-ray coherence length is an indication of less structural defects and/or imperfections. The full width at half maximum (FWHM) values for (112) diffraction plane is around 1.6°, 1.0°, 0.16° and 0.11 for as-ED reference (Cu-poor as well as Cu-rich), laser annealed Cu-poor, laser annealed Cu-rich and furnace annealed Cu-poor sample, respectively. Thus, while the reduction in the FWHM (Fig. 4.10(c)) of the diffraction peaks in Cu-poor samples irradiated for times ≥15 seconds is only about 40%, Cu-rich samples show more than 80% reduction in the FWHM of diffraction peaks. It is important to highlight here that no peaks corresponding to Cu_xO_y or In_xO_y are seen here which has been observed by others [9-10]. This we think is probably because of the different precursor structure used in this study.

The reduction in FWHM value (Fig. 4.10(c)) for the diffraction peaks of Cu-rich samples after CWLA is comparable to what has been observed by annealing CISe films

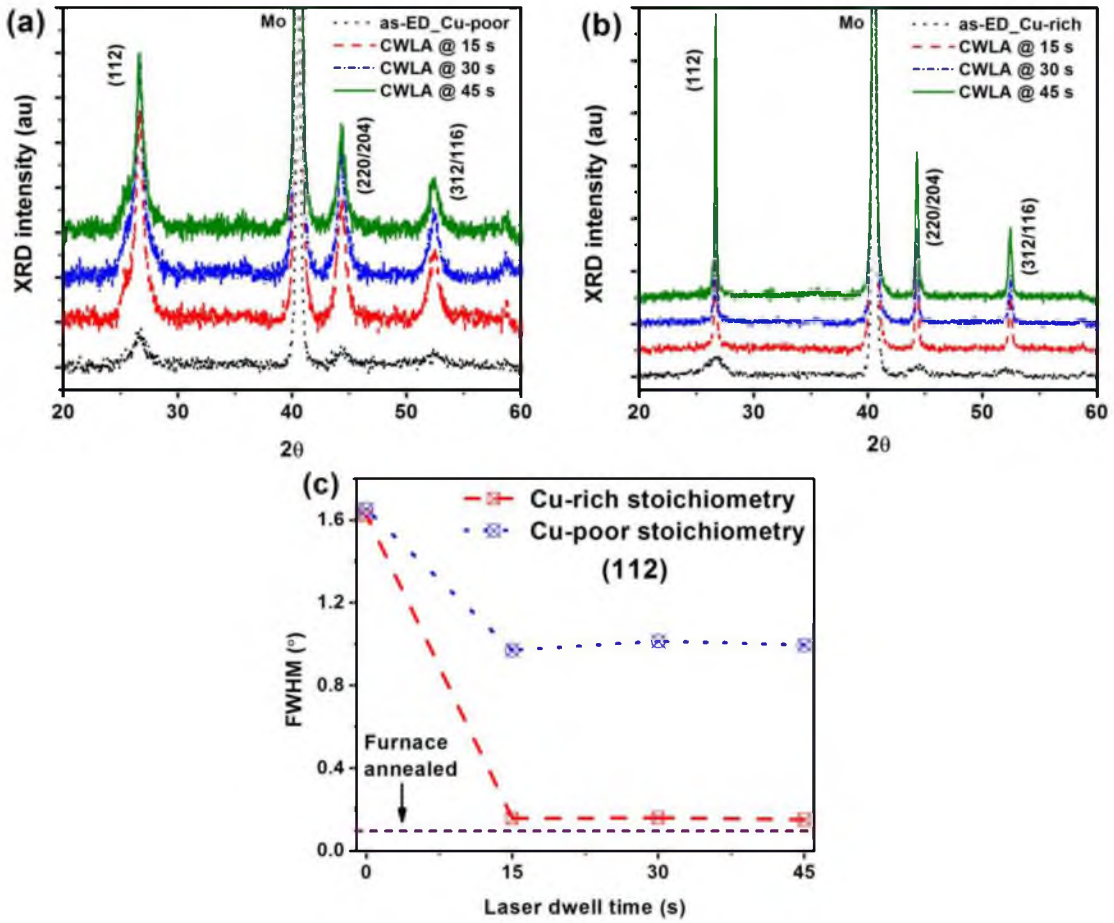

Figure 4.10: θ-2θ XRD results of (a) Cu-poor and (b) Cu-rich samples annealed for varying times at 50 W/cm^2 using 1064 nm laser. Panel (c) shows the reduction in FWHM for the (112) peak after CWLA for varying times at 50 W/cm^2.

in a furnace [17-18] or by rapid thermal annealing [21-22] (both in the presence of Se or S vapor) – the difference here for the CWLA case is the timescale of annealing. In terms of kinetics within the film, CWLA demonstrated herein is roughly 100 times faster than furnace annealing and 10 times faster than the time at maximum temperature for RTA because of the higher temperatures attainable.

It is known in the CIGSe literature that in case of Cu-rich films the individual grains are significantly larger than in case of Cu-poor films [23]. However since no gross changes are observed in the grain structure from SEM observations we speculate that in

this solid state annealing case the x-ray coherence length is being lengthened by increase of intragranular crystalline order.

In order to gain insight into the CWLA process and understand the difference in the behavior of Cu-poor and Cu-rich samples, i.e., how the laser beam interacts with the respective samples based on their optical properties, a finite element model in COMSOL [24] was developed with the geometric structure and optical properties given in Table 4.1. A full-field simulation was run to determine the electric field (V/m) at all points and the total power dissipation density (W/m^3) at all points in the simulation volume. The boundary conditions used in this study are: (a) The tangential components of the electric field at the interface between two mediums is equal, i.e., $E_{tangential}$ (medium 1) =$E_{tangential}$ (medium 2) and (b) the electric flux density at the interface between two medium is equal, i.e., D (medium 1) = D (medium 2), where D= ε E and ε is the electrical permittivity. A periodic boundary condition was used at the boundary edges of the each material element (perpendicular to direction of propagation). This sets the electric field periodic, i.e., equal on the source and destination. Figure 4.11 shows the result of the steady-state simulation when a 1064 nm laser interacts with the Air/CISe/Mo/Glass materials stack. The absorption properties of Cu-poor and Cu-rich CISe are based on Ref. [25], which shows that the absorption coefficient of Cu-rich $CuInSe_2$ is almost twice as for Cu-poor.

For the case of a UV excimer laser, the light is absorbed completely with approximately 10 nm and the temperature may be estimated with little error using a heat flow model with a surface heat source (see Chapter 5). This is not the case for the weakly-absorbed 1064 nm laser. The weak absorption of the 1064 nm light within the

Table 4.1: Properties of the materials and other parameters used for simulating the steady state EM interaction of 1064 nm laser with Air/$CuInSe_2$/Mo/Glass stack. These properties are as per Ref. [20, 25, 27-28].

Layer	Thickness (nm)	1064 nm Complex Refractive Index
Air	500	1
$CuInSe_2$	500	2.95 + 0.15 *i* (Cu-poor), 2.95 + 0.3 *i* (Cu-rich)
Mo	500	2.35 + 4.43 *i*
Glass	2000	$1.5 + 1x10^{-7} i$

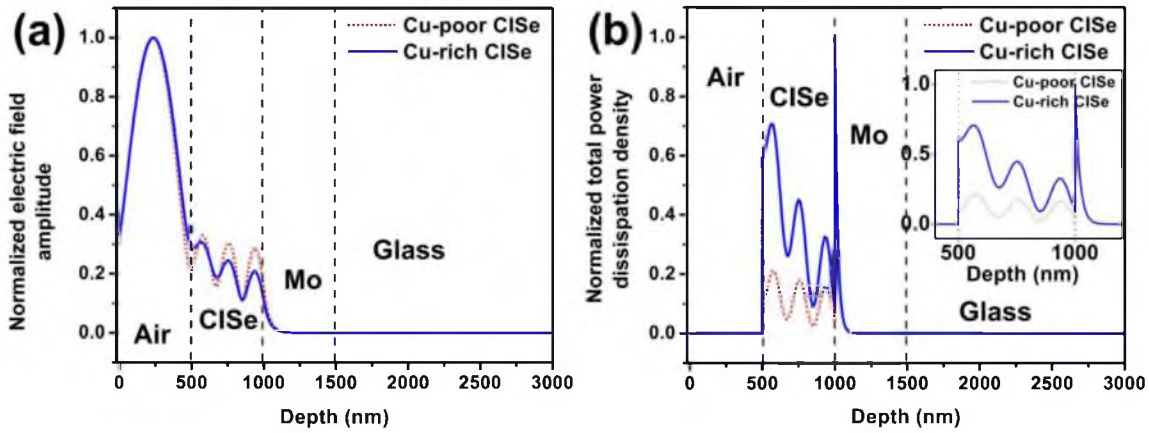

Figure 4.11: Multilayer calculation of the steady-state electric field amplitude for the interaction of the 1064 nm laser with the Air/$CuInSe_2$/Mo/Glass stack. (a) shows the normalized electric field amplitude vs. depth while (b) shows the normalized total power dissipation density as a function of depth. Inset to Fig. 4.11(b) shows the region from 400 nm to 1200 nm.

CISe film results in Fabry-Perot oscillations within the stack and hence a complicated depth-varying heat generation pattern within the CISe film as well as at the Mo interface (Fig. 4.11(b)).

This is in contrast to the situation for a smaller wavelength laser (i.e., hν=5 eV excimer) which is completely absorbed according to the Beer-Lambert law within the currently-used thickness of the CISe and thus points out the importance of calculations and simulations to help understand the laser annealing experiments. One very interesting possibility unique to using engineered incident light spectra (i.e., lasers or filtered broadband sources) is that it may be possible to induce inverted temperature gradients within the film by maximizing power absorption at the Mo interface and minimizing the power absorbed at the front interface. Such an inverted gradient could be utilized to produce otherwise inaccessible compositional, electronic, and microstructural changes in the films.

From the multilayer optical model (which includes reflection from the front interface) in Fig. 4.11(b), it is seen that the power dissipated in the CISe for Cu-rich samples is higher than for Cu-poor samples and hence the temperatures reached during the course of CWLA will be greater for Cu-rich samples for a given laser power density. This would be in addition to any effects of pseudo-liquid Cu_xSe_y 2nd phase fluxing widely discussed in the CIGSe literature [26]. These could possibly explain the greater reduction in FWHM for Cu-rich samples. Another possibility which we cannot rule out is that the thermophysical properties, i.e., thermal conductivity, specific heat capacity, emissivity, density, and melting temperature of Cu-poor and Cu-rich samples are different, which may also contribute to higher temperatures for the Cu-rich case. This is well supported

by the fact that properties like thermal conductivity and reflectivity of CIGSeS undergo a sudden change as soon as a small amount of Cu-excess is present in the material and the secondary phases formed because of the Cu-richness dominate the properties of the Cu-rich samples [26].

In order to investigate phases present at the sample surface, Raman spectroscopy was performed on the samples. Besides identification of small volume fractions of phases which XRD θ-2θ scans may miss, Raman spectroscopy is an important tool for characterization of chalcopyrite thin films because XRD peaks of phases such as sphalerite cation disordering, Cu_xSe_y etc. lie close to XRD peaks of the chalcopyrite phase of CISe while they may be easily distinguished from Raman data [27]. The inset to Fig. 4.12 (a) and (b) show the Raman spectra of Cu-poor and Cu-rich samples respectively in the spectral range of 125-300 cm^{-1}. No Raman peaks corresponding to secondary phases such as Cu or In oxide and/or selenides are observed. Single crystalline $CuInSe_2$ has a dominant Raman peak at 174-175 cm^{-1} corresponding to the chalcopyrite (CH) A_1 vibration mode corresponds to motion of all of the Se anions against the cation sublattice. The other phonon modes that are generally seen are mixed B_2-E modes observed between 215-230 cm^{-1} [29].

As can be seen from the inset to Fig. 4.12 (a) and (b) the spectrum for the as-ED reference samples is featureless except for a broad hump extending from 150 to 250 cm^{-1} indicating high disorder in as-ED state. After CWLA both A_1 and mixed B_2-E modes emerge indicating increased crystalline quality and or ordering in the material. As the dwell time increases from 15 to 45 s, the peak position of the A_1 mode for the Cu-rich samples (Fig. 4.12 (b)) approaches 175 cm^{-1}. The observed peak position is in agreement

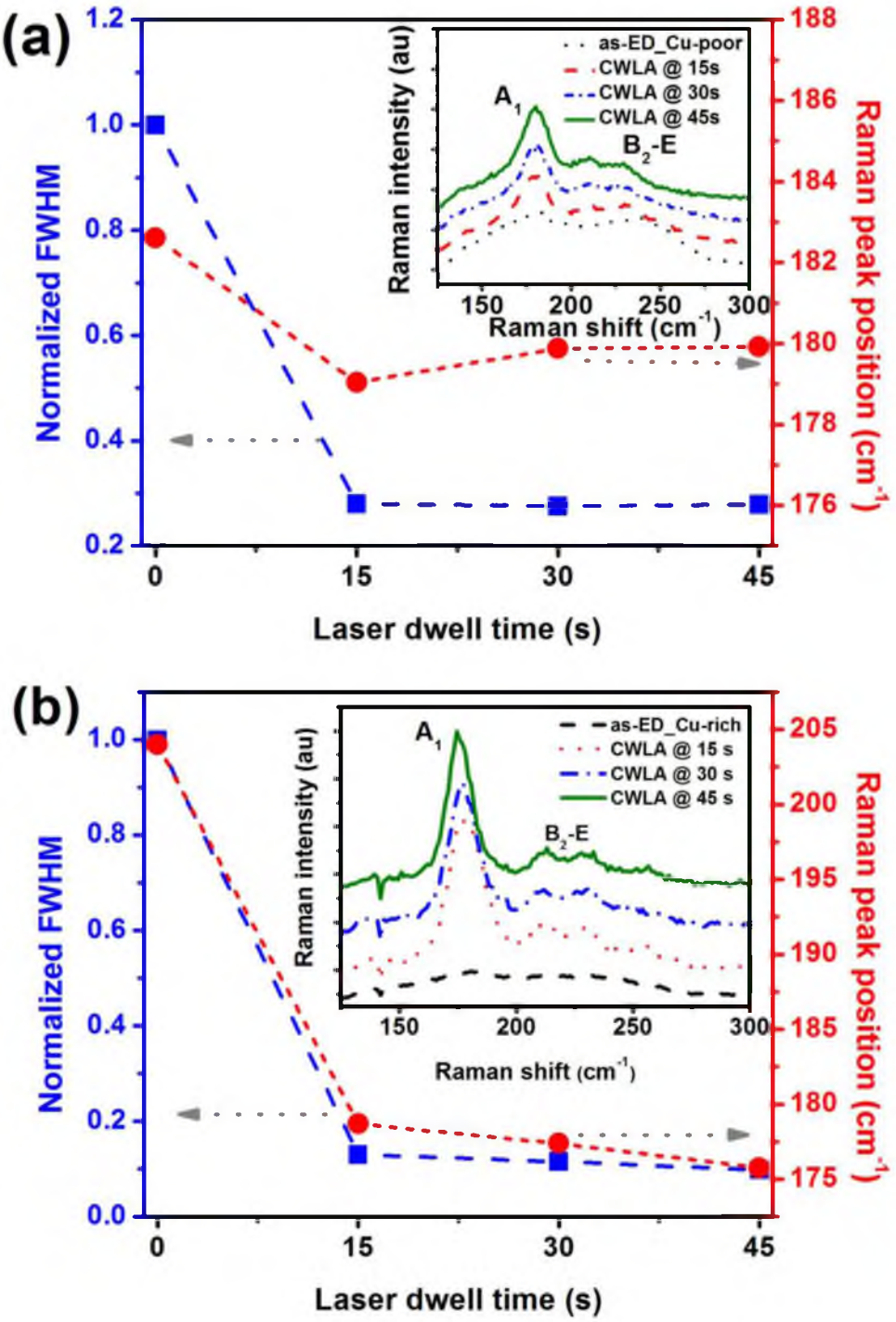

Figure 4.12: Comparisons of Raman peak position and FWHM for the A_1 vibration mode for (a) Cu-poor (Cu/In < 1) and (b) Cu-rich (Cu/In > 1) samples annealed for varying times at 50 W/cm^2 using the 1064 nm laser. The insets show the respective Raman spectra in the range from 125 cm^{-1}-300 cm^{-1}.

with what has been observed for furnace annealed samples [17-18]. However the peak position for Cu-poor samples (Fig. 4.12(a)) trends towards 180 cm^{-1}. This shift of the A_1 mode towards higher wavenumber could be attributed to compressive stress [30] or to the presence of extended defects such as twins, dislocations and grain boundaries [31]. These two possible reasons may correlate to the XRD results, in which we see only about 40% improvement in crystalline quality of the Cu-poor samples after CWLA indicating residual numbers of extended defects and strain resulting from cold deposition of samples. Another possible reason for the apparent shift in A_1 mode could be because of presence of Cu-Au ordered CISe phase coexisting with the chalcopyrite CISe phase. The Cu-Au ordered CISe phase has an energy formation difference of only 2 meV per atom with that of chalcopyrite CISe phase [32-33] and hence could be formed easily. The Raman peak position for the Cu-Au ordered CISe phase is reported to be at 185 cm^{-1} [34], which may imply that our samples contain either incomplete ordering or both types of ordering in different grains. Examining the FWHM values for the A_1 peak (Fig. 4.12 (a) and (b)), the reduction is comparable to the XRD results, i.e., a decrease of more than 80% observed for the Cu-rich CWLA samples. The FWHM of the A_1 mode ($\approx$ 12 cm^{-1}) for the Cu-rich CWLA films is comparable to furnace annealed samples [17-18]. On the other hand the FWHM of Cu-poor samples after CWLA is slightly larger at 16 cm^{-1} also indicative of inhomogeneity.

Encouraged by the results with CWLA of CISe films, an attempt was made further to reduce the dwell time of the laser on the samples, since the main idea behind this research is to lay the foundation for a path that could be used to increase the throughput, reduce the cost and synthesize device quality CIGSeS films via a complete nonvacuum synthesis

route. The power density of the laser beam was increased to ≈ 1000 W/cm^2 and the dwell time of the laser beam on the sample was reduced to 1 s. Figure 4.13(a) shows the XRD result of as-ED and laser annealed sample. As can be seen from the figure, the reduction observed in the FWHM of the (112) peak is about 70%. The SEM images (Fig. 4.13(b)) suggest that the annealing still takes place in the nonmelting regime. Although the samples annealed at high laser power density yield photoresponse [35], a big challenge is to overcome the problem of Se loss which as discussed earlier is not good from device point of view. Figure 4.14 shows the evidence of Se loss during the course of CWLA.

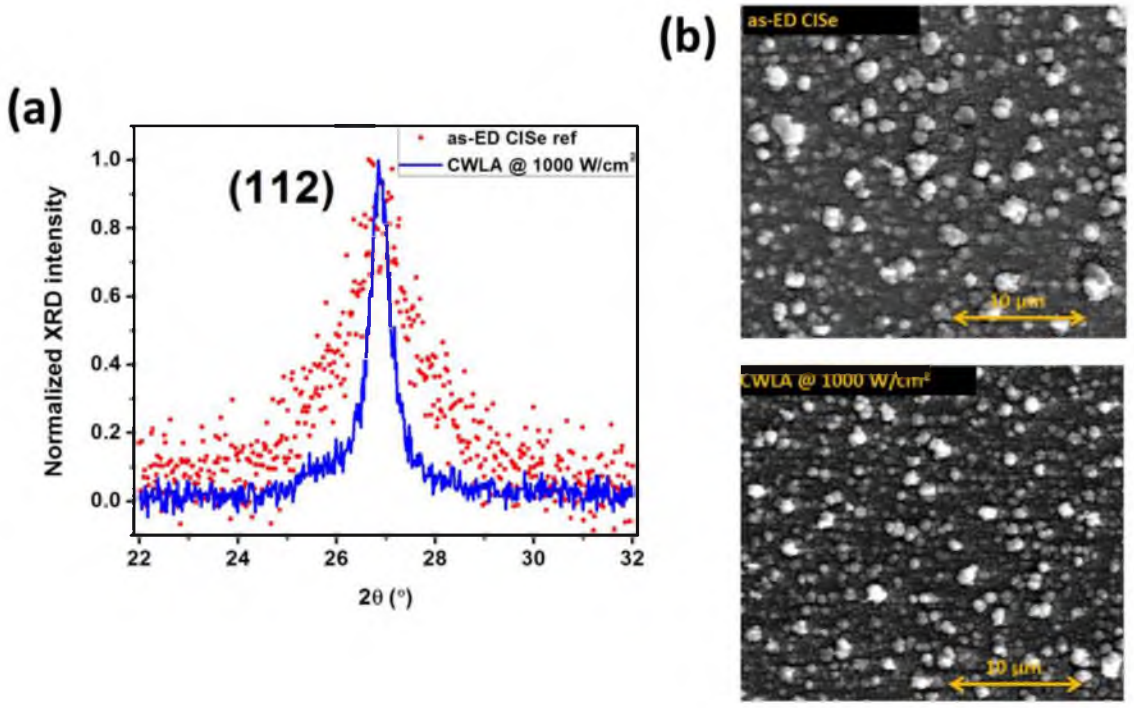

Figure 4.13: CWLA results for reduced dwell time and high power density. (a) XRD results of as-ED ref and laser annealed sample at 1000 W/cm^2. (b) SEM images of as-ED ref and laser annealed sample at 1000 W/cm^2. The dwell time of the laser beam is 1s.

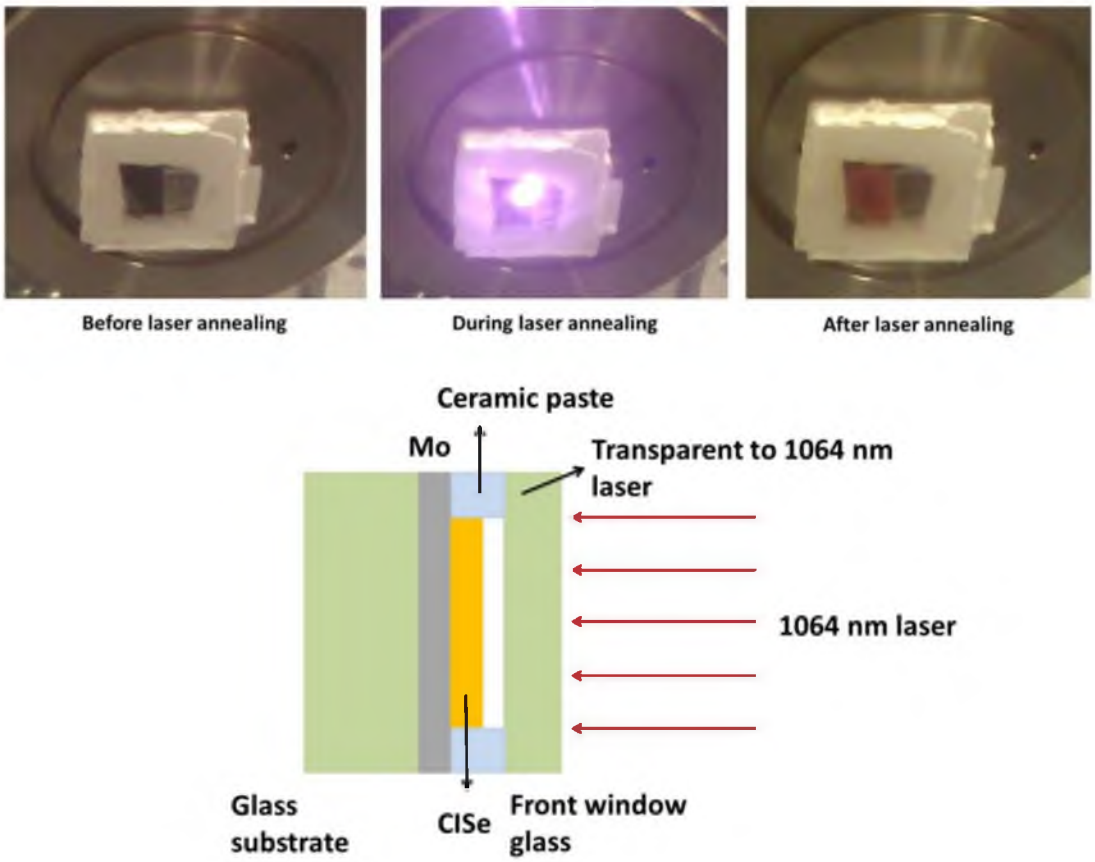

Figure 4.14: Evidence of Se loss (red condensate on window) from the sample and graphic illustrating experiment design for the same.

As can be seen in Fig. 4.14 after laser annealing, the evaporated Se from the sample (hot) condenses (red matter) on the glass (cold) which is transparent to 1064 nm laser. This experiment suggests that future work should focus on designing the experiment to avoid Se loss from the sample but at the same time improve crystallinity of the as-ED CISe film.

4.4 Summary

Electrochemical deposition coupled with laser annealing offers a complete non-vacuum synthesis route for CISe film processing. We have carried out pulsed laser

annealing (PLA) and continuous wave laser annealing (CWLA) of as-electrodeposited (as-ED) CISe films using 248 nm and 1064 nm lasers. PLA in melting regime using both kinds of lasers leads to dewetting of CISe on the back contact layer making the samples unsuitable for photovoltaic application. On the other hand PLA in submelting regime does not shows any improvements in the crystalline quality of the samples as is evident by broad X-ray diffraction (XRD) peaks.

The CWLA of as-ED CISe films in the submelting regime shows promising results and has outlined the course for the possible future experiments. The effect of Cu/In ratio on the crystalline quality of the samples is compared for CWLA conditions of: $\approx$50 W/cm^2 and dwell time of $\geq$ 15 s. While Cu-rich samples yield parameters (such as X-ray coherence length, FWHM of XRD peaks and Raman peak) comparable to furnace annealed CISe films, Cu-poor samples do not show significant improvements. For example, the reduction in FWHM of XRD (112) diffraction plane is about 80% for Cu-rich samples and about 40% for Cu-poor samples. Future experiments will focus on reducing the dwell time as well as the Se loss which might limit the process feasibility and cell performance, respectively.

4.5 References

[1] M.A. Green, K. Emery, Y. Hishikawa, W. Warta, and E.D. Dunlop, Prog. Photovolt: Res. Appl. 20 (2012) 12.

[2] http://www.empa.ch/plugin/template/empa/3/131438/---/l=2

[3] T. Lincott, Thin Solid Films 487 (2005) 40.

[4] T. Voß, J. Schulze, A. Kirbs, J. Palm, V. Probst, S. Jost, R. Hock, M. Purwins, Proceedings of the 22nd European Photovoltaic Solar Energy Conference and Exhibition, Milan (Italy), Sep. 3 - 7, 2007.

[5] H. Deligianni, S. Ahmed and L.T. Romankiw, Elec. Soc. Interface 20 (2011) 47.

[6] P.J. Dale, A.P Samantilleke, G Zoppi, I Forbes and L.M. Peter, J. Phys. D: Appl. Phys. 41 (2008) 085105.

[7] M.C. Joliet, C. Antoniadis, R. Andrew, and L.D. Laude, Appl. Phys. Lett. 46 (1985) 266.

[8] M.C. Joliet, C. Antoniadis, R. Andrew, and L.D. Laude, Thin Solid Films 126 (1985) 143.

[9] G.D. Mooney, A.M. Hermann, Energy Res. Abstr. 15 (1990) 50720.

[10] G.D. Mooney, A.M. Hermann, Energy Res. Abstr. 14 (1989) 44906.

[11] S. Jost, R. Schurr, F. Hergert, R. Hock, J. Schulze, A. Kirbs, T. Voβ, M. Purwins, J. Palm and I. Mys, Sol. Energ. Mat. Sol. Cells 92 (2008) 410.

[12] D. Bhattacharyya, S. Bocking and M.J. Carter, J. Mater. Sci. 31 (1996) 5451.

[13] A. Bhatia, H. Meadows, A. Crossay, P.J. Dale and M.A. Scarpulla., Proc. SPIE 8473, Laser Material Processing for Solar Energy, 84730F (October 12, 2012).

[14] A. Bhatia, M.L. Nowell, P.J. Dale, M.A. Scarpulla., MRS Spring 2010 Proceedings 1268 (2010) 103.

[15] K. Orgassa, H.W. Schock, and J.H. Werner, Thin Solid Films 431 (2003) 387.

[16] A.L. Patterson, Phys. Rev. 56 (1939) 978.

[17] A. Bhatia, H. Meadows, W.M. Hlaing Oo, P.J. Dale and M.A. Scarpulla, Thin Solid Films 531 (2013) 566.

[18] A. Bhatia, H. Meadows, M.C. Hymas, E.M. Smith, P.J. Dale and M.A. Scarpulla, Conference Record of the 38th IEEE-PVSC 2012 Proceedings, To be published.

[19] V. Depredurand, Y. Aida, J. Larsen, T. Eisenbarth, A. Majerus, S. Siebentritt, Conference Record of the 37th IEEE-PVSC 2011 Proceedings, 337 (2011).

[20] R. Scheer and H.W. Schock, [Chalcogenide Photovoltaics Physics, Technologies, and Thin Film Devices], Weinheim, Germany: Wiley-VCH, 2011.

[21] A. Bhatia, M.A. Karmarkar, H. Meadows, P.J. Dale and M.A. Scarpulla, Proc. SPIE 8549, 16th International Workshop on Physics of Semiconductor Devices, 85493B (October 15, 2012).

[22] A. Bhatia, M.A. Karmarkar, H. Meadows, M.C. Hymas, E.M. Smith, P.J. Dale and M.A. Scarpulla, Conference Record of the 38th IEEE-PVSC 2012 Proceedings, 879 (2012).

[23] E.R. Don and R. Hill, Solar Cells 16 (1986) 131.

[24] COMSOL Multiphysics Version 4.0 released, Sealing Technology 2010 (2010) 4.

[25] G.D. Mooney and A.M. Hermann, NREL subcontract report March 1990-April 1991, NREL/TP- -4 11 -47 52, DE92 001222.

[26] R. Klenk, T. Wulter, H.W. Schock, and D. Cahen, Adv. Mater. 5 (1993) 114.

[27] S.R. Kodigala, [$Cu(In_{1-x}Ga_x)Se_2$ Based Thin Film Solar Cells, Volume 35 (Thin Films and Nanostructures)], Academic Press, 2010.

[28] R. Kitamura, L. Pilon and M. Jonasz, Appl Optics 46 (2007) 8118.

[29] C. Rincon and F.J. Ramirez, J. Appl. Phys. 72 (1992) 4321.

[30] O. Ramdani, J.F. Guillemoles, D. Lincot, P.P. Grand, E. Chassaing, O. Kerrec, E. Rzepka, Thin Solid Films 515 (2007) 5909.

[31] V. Izquierdo-Roca, J. Alvarez-García, L. Calvo-Barrio, A. Perez-Rodríguez, J.R. Morante, V. Bermudez, O. Ramdani, P.P. Grand, and O. Kerre, Surf. Interface Anal. 40 (2008) 798.

[32] D. Wang, Y. Cao, and L. Wan, J. Mater. Res. 24 (2008) 2373.

[33] D. Wang, L. Wan, Z. Bai, and Y. Cao, Appl. Phys. Lett. 92 (2008) 211912.

[34] B.J. Stanbery, S. Kincal, S. Kim, C.H. Chang, S.P. Ahrenkiel, G. Lippold, H. Neumann, T.J. Anderson, O.D. Crisalle, J. Appl. Phys. 91 (2002) 3598.

[35] H.J. Meadows, A. Bhatia, M.A. Scarpulla, S. Siebentritt and P.J. Dale, MRS Spring 2013 Proceedings, to be published.

CHAPTER 5

LASER ANNEALING OF PREVIOUSLY ANNEALED CHALCOPYRITE FILMS

5.1 Introduction and motivation

$Cu(In,Ga)Se_2$ (CIGSe) is one of the leading inorganic absorber layers for thin film photovoltaic technology. Although the gap between the power conversion efficiency (η) of champion cells synthesized in lab (η= 20.4 %) [1] and the highest reported module efficiency (η= 15.7 %) [2] is closing, there is still a lack of certainty about the details of point and extended defects responsible for the higher or equivalent efficiency of polycrystalline CIGSe solar cells when compared to their epitaxial counterparts.

This chapter discusses optoelectronic changes induced by nanosecond pulsed laser annealing (PLA) of electrodeposited-furnace annealed (EDA) $CuInSe_2$ (CISe) thin films (also some other CISe films, see section 5.2 for sample preparation details). The EDA films have been furnace annealed in Se atmosphere after electrochemical deposition.

PLA is very different from furnace annealing and or rapid thermal annealing (RTA), in that the effective heating time in PLA is of the order of 10's to 100's of ns as opposed to furnace annealing (>1000 s) and RTA (~ 1-100 s). Very high temperatures (including melting) and quenching rates (10^9 K/s) can be achieved in PLA and thus the annealing parameters that can be realized using PLA can never be achieved using furnace annealing

or RTA processes. For more discussion on laser annealing theory, the reader should refer Chapter 2.

In this chapter we will discuss whether or not access to these very different annealing regimes can yield improvements in processing and performance of CISe and related thin film photovoltaic materials. Evidence of improvement in photoconductivity has been reported by Gnatyuk et al. [3] following the PLA of CdTe films using a pulsed ruby laser with 694 nm wavelength and a pulse width of 20 ns. Improvements in minority carrier diffusion length, carrier lifetime, mobility, and cell efficiency have been reported earlier by Wang et al. [4-5] following the PLA of vacuum-deposited CIGSe films using a pulsed excimer laser of 248 nm wavelength and 25 ns pulse width. The changes have been attributed to annealing of defect states probably residing near the CdS/CIGSe interface but no identification of the specific defects was carried out. The work reported herein is an attempt to identify changes in dominant defects after PLA of EDA-CISe absorber layers.

5.2 Experimental details

5.2.1 Sample synthesis and preparation

CISe films were electrodeposited followed by furnace annealing (EDA) in Se atmosphere as per Ref. [6] on Mo coated soda lime glass substrates. The electrochemical deposition and furnace annealing was carried out at the University of Luxembourg. The thickness of CISe films after furnace annealing is $\approx$ 1μm. Photoresist was applied to the samples to protect the surface and the 1" x 1" EDA-CISe films were diced into 5 mm x 5 mm samples after which the photoresist was removed with acetone. Although most of

the characterization was done on EDA samples, some statistics have been collected on epitaxial CISe films from the University of Luxembourg and also physical vapor deposited CIGSe films acquired from AQT Solar Company. The details of the deposition are described in Ref. [7] and Ref. [8], respectively.

PLA was done using a KrF excimer laser (λ = 248 nm, pulse width ≈ 25 ns) while the samples were held in a custom annealing chamber with a quartz front window. Figure 5.1 shows the 248 nm laser annealing setup and the annealing chamber. The chamber was purged with flowing N_2 to provide an inert atmosphere and suppress oxidation during PLA. Each sample was annealed with 5 identical laser pulses each in the low fluence regime (< 100 mJ/cm^2) below the threshold for surface melting. Note that the time between pulses was much longer than the cooling time after each individual pulse, so the temperature fields T(x,t) for each pulse are completely independent. The spot size of the laser was slightly larger than the sample size and was uniform in intensity. Thus the entire sample area was irradiated under the same conditions.

In order to perform electrical characterization, reference and laser annealed samples were KCN etched (5 wt. % solution) for 1 minute immediately before Al (for Schottky diodes) and CdS (for full cell stack) deposition. KCN treatment in general is used to etch off excess Cu_xSe_y from CIGSe films [9]. A 250 nm thick Al film was deposited on top of CISe using e-beam evaporator. The deposition was carried out at a base pressure of < $1x10^{-6}$ Torr using a current of 100 mA and 6.5 kV voltage.

In order to make a complete cell stack, CdS/i-ZnO and n-ZnO were deposited on reference and laser annealed samples. The deposition of CdS was carried out using chemical bath deposition (CBD). The CBD process of CdS deposition was developed by

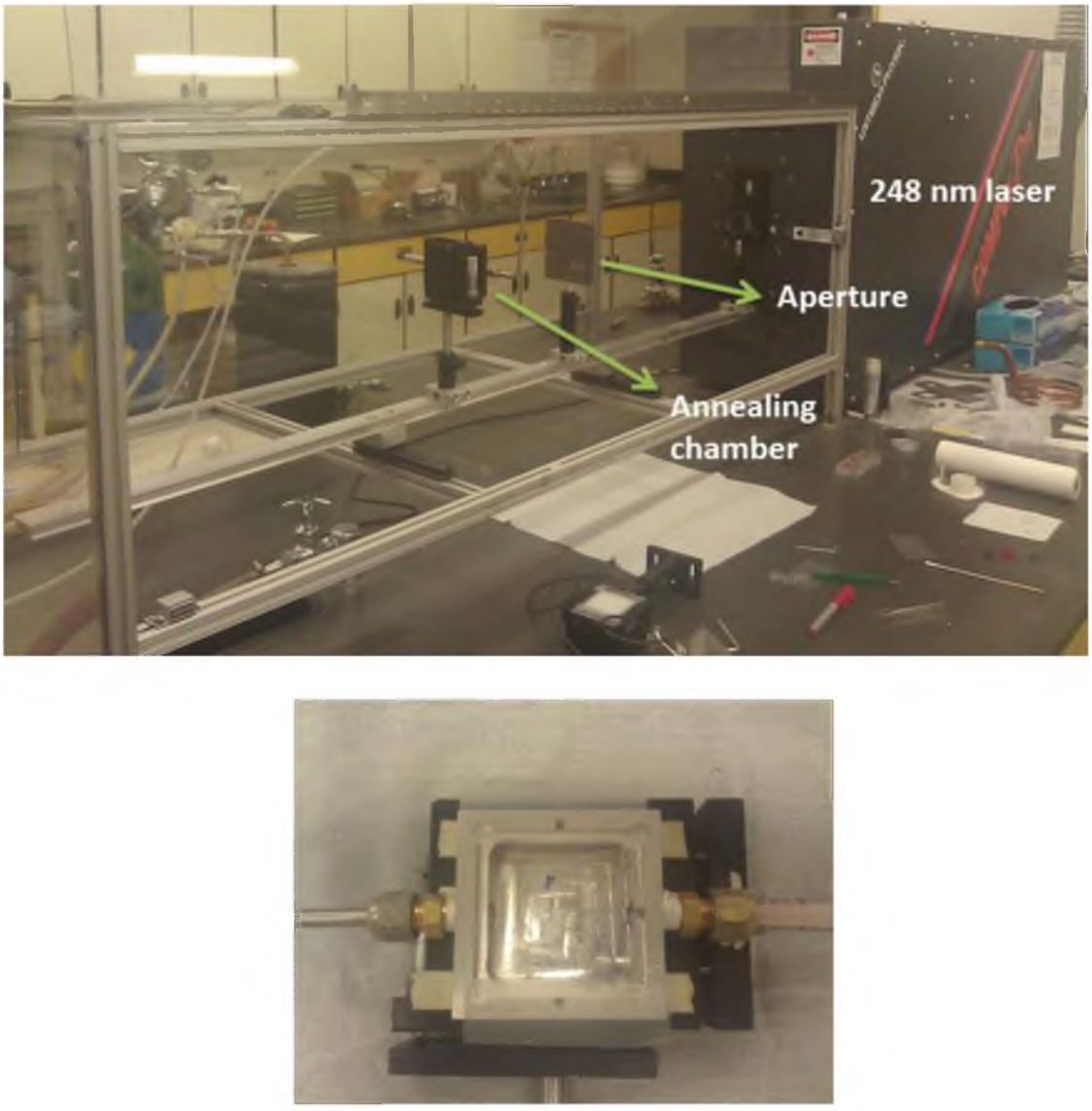

Figure 5.1: 248 nm PLA setup and the custom built annealing chamber.

E. Lund, another graduate student in Dr. Scarpulla's group, following the process used at the National Renewable Energy Laboratory (NREL). It involves a precipitation reaction via the combination of different solutions. The cadmium source is a salt, usually $CdCl_2$, $CdSO_4$, or $Cd(CH_3COO)_2$. The sulfur source is thiourea ($SC(NH_2)_2$) and the remaining reactants are deionized (DI) water and ammonium hydroxide (NH_4OH). These solutions are mixed together in a heated beaker ($\approx$ 65 °C) and agitated with a magnetic stir bar during the deposition. The deposition time varies but is usually around 11-13 minutes. A sacrificial Mo coated glass slide is included during the reaction. The CdS precipitates out of solution, depositing on the sample(s). The sacrificial Mo slide is used to determine when an adequate CdS layer thickness is achieved by noting the thickness-dependent color change. The Mo starts out silvery and upon the addition of CdS (which is yellowish in color) will change colors from silver to brown to purple and then to blue. The ideal deposition time involves stopping the deposition when the Mo sample changes from purple to blue which corresponds to a thickness of approximately 50-70 nm.

The CdS deposition was followed by intrinsic (i) and n-type ZnO using the Denton sputtering chamber at the University of Utah Nanofab facility. The i-ZnO is deposited for about 15 minutes at an Ar pressure of 2.8 mTorr using RF sputtering at 125 W. The n-ZnO:Al was deposited for 30 minutes at an Ar pressure of 2.8 mTorr using RF sputtering at 125 W. The base pressure was $< 1x10^{-6}$ Torr for ZnO deposition. The target materials for i-ZnO and n-ZnO are pure ZnO and (2% Al doped) ZnO, respectively, both manufactured by Kurt J Lesker.

5.2.2 Characterization

Scanning electron microscopy (SEM) at an acceleration voltage of 15 kV was used to investigate the surface morphology. An electron microprobe (EPMA) equipped with four wavelength-dispersive X-ray spectrometers was used for elemental analysis. Raman spectra were recorded using a micro-Raman spectrometer with 488 nm laser excitation.

Capacitance-voltage (C-V) and DLTS analyses were carried out using a system from Semetrol, LLC which incorporates a Boonton 7200 capacitance meter. For the DLTS measurements a forward bias filling pulse of +0.1 V was applied for 50 ms followed by -0.5 V measurement bias. Dark and light J-V measurements were carried out using Oriel Sol3A Class AAA Solar Simulator and a Keithley 2400 SMU.

Photoluminescence (PL) measurements were carried out at the University of Luxembourg. Samples were placed in a cryostat and illuminated with 514 nm laser light with varying intensity of illumination. PL was recorded on an InGaAs CCD detector with 5 s integration time.

5.3 Results

5.3.1 Heat flow modeling and calculation

For the 5 eV photons from the KrF laser, the optical absorption depth is approximately 10 nm while within the pulse duration (≈ 25 ns) heat will diffuse a distance of 450 nm. Therefore the effects of the laser may be approximated as a surface heat source. The thermal diffusion equation for an infinite CISe layer with a surface heat source with Gaussian temporal dependence is:

$$\frac{c_p \rho}{k}\frac{\partial T}{\partial t} = \frac{\partial}{\partial x}\left(\frac{\partial T}{\partial x}\right) + \frac{F\alpha(1-R)e^{-(\alpha x)}\, e^{-\left(\frac{t^2}{2\sigma^2}\right)}}{\sigma k\sqrt{2\pi}} \qquad (5.1)$$

where c_p is the specific heat capacity (0.30 J/g-K) [10], ρ is the density (5.77 g/cm^3) [10], k is the thermal conductivity (0.037 W/cm-K) [10], F is the laser fluence (J/cm^2), α is the optical absorption coefficient at 5 eV (10^6 cm^{-1}), R is the reflectivity (0.32) of CISe in air [11], and σ is the standard deviation of the temporal Gaussian laser pulse. The total pulse energy per unit area or fluence (J/cm^2) is the time integral of the instantaneous power flux (W/cm^2) for the pulse.

The following procedure was used to estimate the temperature fields T(x, t) in the electrodeposited CISe samples during PLA. Note that this is considered an estimate because the critical material parameters such as surface reflectivity and thermal conductivity are ill-defined for the nanostructured films resulting from electrodeposition and because temperature-dependent properties are not available. A no-flux boundary condition $\frac{\partial T(x,t)}{\partial x}\Big|_{x=0} = 0$ has been shown to introduce minimal error for ns PLA of semiconductors [12] and was used here also. However, in Ref. [12] the case of crystalline samples such as Si was considered, where the conductive heat flow is really fast. Hence taking into account these factors, we propose an error bar of about ± 100 K in the predicted temperatures, although reducing the thermal conductivity of CISe in the model affects the temperature by about 25 K only.

An initial condition of T(x, 0) = 298 K and a constant-temperature condition of 298 K at a depth of 10 μm were assumed. Results are only shown in Fig. 5.2 for depths up to the film thickness of 1 μm and for times such that the temperature does not change appreciably at this depth. These estimates are relevant for the actual CISe film on Mo because no heat reaches the Mo interface during the pulse time. Figure 5.2(a) shows the

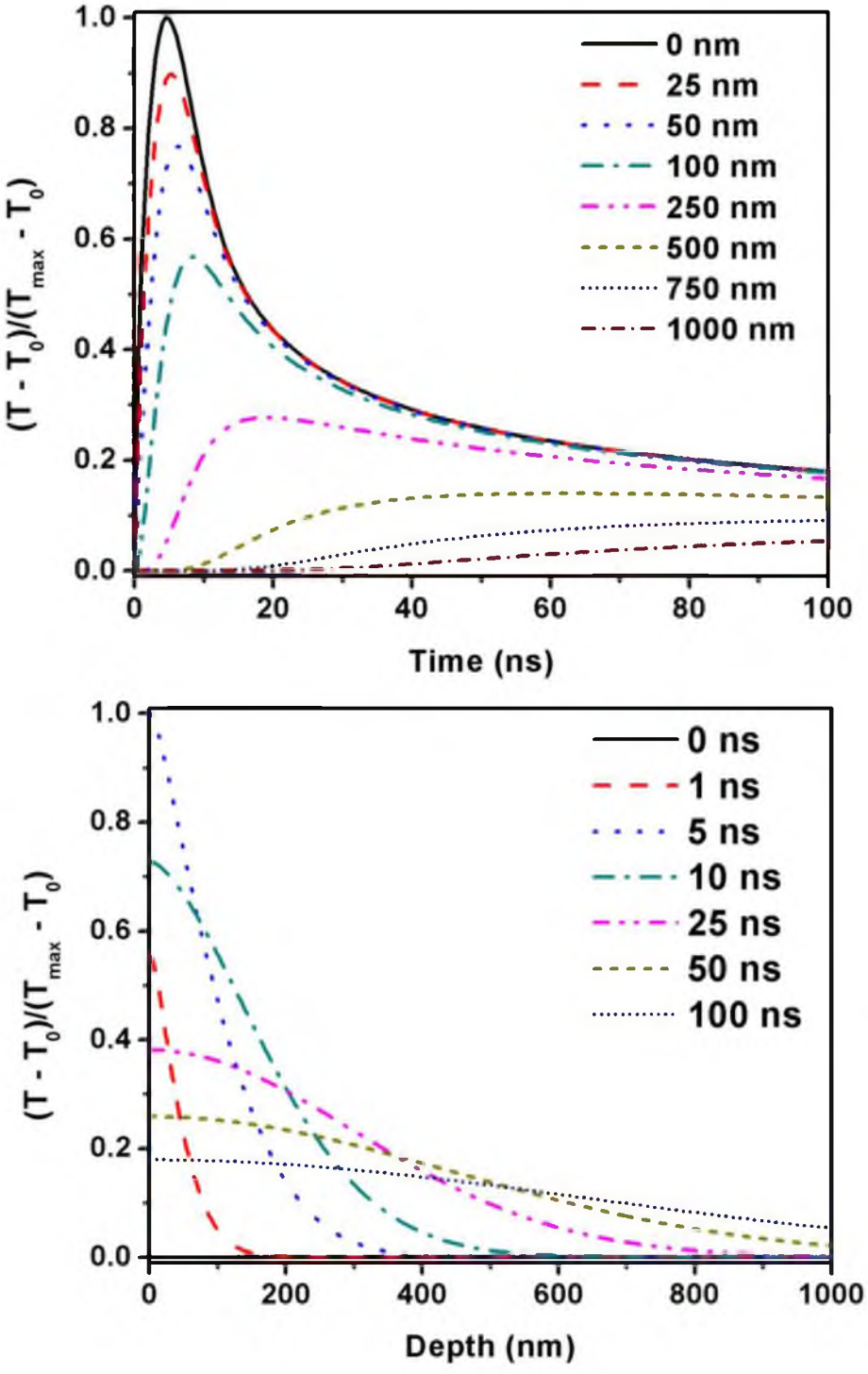

Figure 5.2: Normalized temperature increase above initial temperature (T_o) (a) versus time at varying depths and (b) versus depth at varying times.

normalized temperature profile versus time for different film depths and Fig. 5.2(b) shows the normalized temperature profile versus depth for different times. The maximum temperature always occurs at the surface and noting that the pulse shape can be assumed to be fluence-independent for a standard excimer laser, a proportionality constant of 13.5 K-cm^2/mJ has been calculated between the maximum surface temperature increase above the initial temperature (K) and the pulse fluence (mJ/cm^2). This is a useful estimate because the differential equation is linear and we are not using temperature dependent properties so we could scale temperature for any fluence. This gives estimated maximum temperatures of 570, 705, and 840 K (± 100 K) for fluences of 20, 30, and 40 mJ/cm^2, respectively. Though we are working at fluences lower than required for surface melting of CISe ($T_{melt} \approx 1200$ K) the temperatures during PLA are enough to cause atomic level rearrangement and modify the optoelectronic behavior of the films (evidence discussed below). Also, this is supported in Refs. [13-14] which suggest that multiple low power laser pulses (below melting regime), well-separated in time can cause defects reordering in a disordered semiconductor.

5.3.2 Structural and compositional characterization

The top view and cross-sectional SEM images of the EDA-reference and 40 mJ/cm^2 PLA sample in Fig. 5.3 show that no gross microstructural changes are induced by the laser annealing. The composition of the films as measured by EPMA is shown in Fig. 5.4(a). The inset in Fig. 5.4(a) shows the variation in Cu/In and Se/(Cu+In) ratios with fluence. For both EDA-reference and PLA samples the values of Cu/In and Se/(Cu+In)

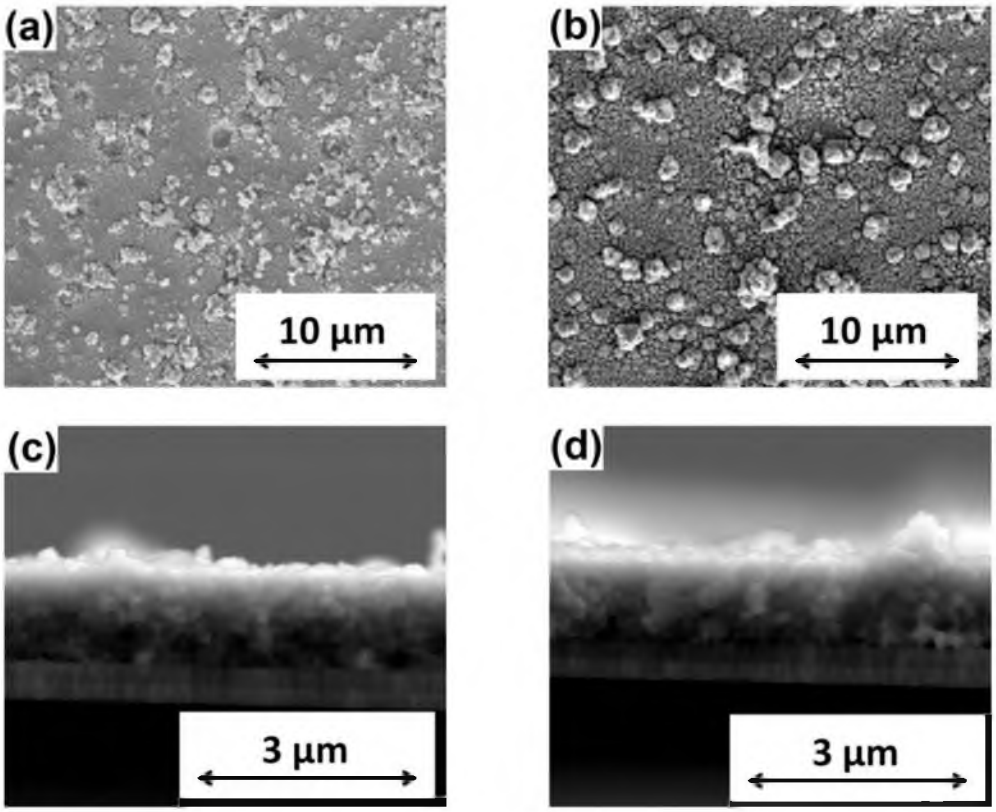

Figure 5.3: Top view SEM images of (a) EDA-reference sample and (b) PLA sample processed at 40 mJ/cm^2. Cross-sectional SEM images of (c) EDA-reference sample and (d) PLA sample processed at 40 mJ/cm^2.

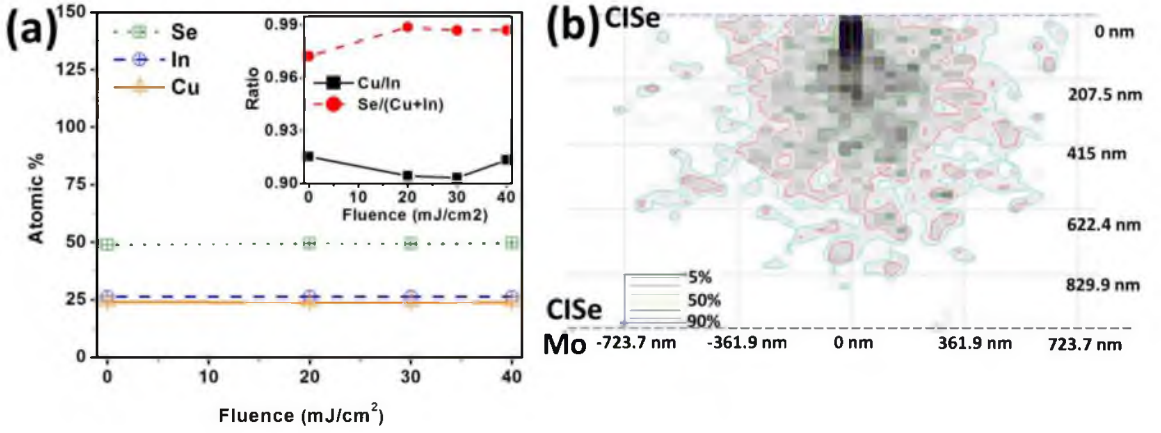

Figure 5.4: Composition and simulation results for CISe films. (a) EPMA results showing the composition of EDA-reference and PLA samples. Inset shows minor variation in Cu/In and Se/(Cu+In) ratios for samples. (b) CASINO simulation results for electron beam at 15 kV interacting with CISe.

are less than 1, suggesting that all of the films are both Cu-poor and Se-poor. The composition results are in agreement with the photoluminescence (PL) spectra of the samples (see section 5.3.3.1) which shows the characteristic behavior of Cu-poor samples, i.e., relatively broad emission from below the stoichiometric band gap as compared to their Cu-rich counterparts. The changes in the values of Cu/In and Se/(Cu+In) for EDA-reference and PLA samples are less than 2%, which is within the limits of error. Therefore any changes in the composition as a result of the PLA carried out in this work are below the noise level. However there is a possibility of some Se loss from the samples. Fig. 5.4(b) shows the estimated depth of collection of signal (≈ 800 nm) for EPMA measurements as determined from CASINO simulations [15].

The peak near 290 cm^{-1} [16] in the Raman scattering measurements on the EDA-reference sample (Fig. 5.5(a)) indicates the presence of CuO which could possibly contribute to the high built-in voltage (V_{bi}) observed in the capacitance-voltage characterization (see section 5.3.3.2.1). The absence of the CuO peak for all of the PLA samples indicate that the laser treatment removes surface copper oxides – a significant finding given the risk of further oxidation during the PLA process. The PLA samples show only the A_1 (174 cm^{-1}) and mixed B_2-E (213-230 cm^{-1}) phonon modes corresponding to the CISe chalcopyrite phase [17]. Figure 5.5(b) shows that the A_1 mode for EDA-reference sample occurs at slightly higher wavenumber than those for the PLA samples. Relaxation of residual strain present in the EDA samples during PLA processing may help to explain this behavior.

A decrease in full width at half maximum (FWHM) of the Raman A_1 mode is also observed following the PLA process and is a signature of improved crystalline quality.

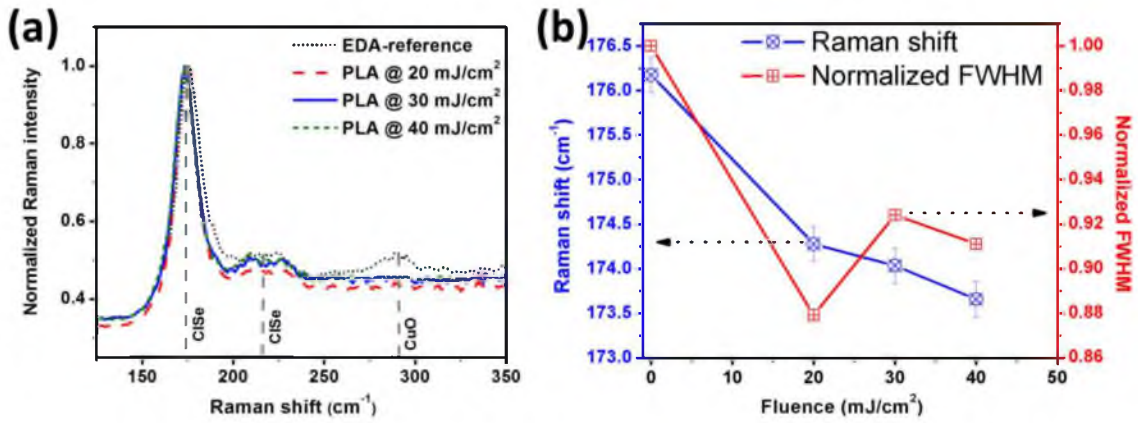

Figure 5.5: Raman characterization results. (a) Raman spectra for EDA-reference and PLA samples. The peak at 174 $cm^{-1}$and 213-230 cm^{-1} correspond to A_1 and mixed B_2-E phonon modes, respectively. The peak at 290 cm^{-1} corresponds to CuO phase present in EDA-reference sample. (b) Raman peak position and normalized FWHM of A_1 mode for EDA-reference and PLA samples.

Figure 5.5(b) shows the normalized FWHM of the Raman 174 cm^{-1} peak. The structural improvement result is consistent with the results reported elsewhere [4, 18]. The mechanism(s) responsible for the observed phonon mean free path increase is not known but grain growth should be ruled out based on the SEM observations of the unchanged surface morphology. This improvement in the crystalline order parameter proves that measurable atomic diffusion does take place during PLA although the diffusion lengths for each species during each pulse are not known.

5.3.3 Optoelectronic characterization

5.3.3.1 Photoluminescence measurements

PL measurements were made on two sets of EDA-ref and laser annealed samples, measured at University of Luxembourg. Figure 5.6(a) and (b) shows the PL data on EDA-ref and PLA samples recorded at 10 K and 298 K, respectively. Since our samples are polycrystalline we do not expect to see excitonic transitions, so the PL spectra in Fig.

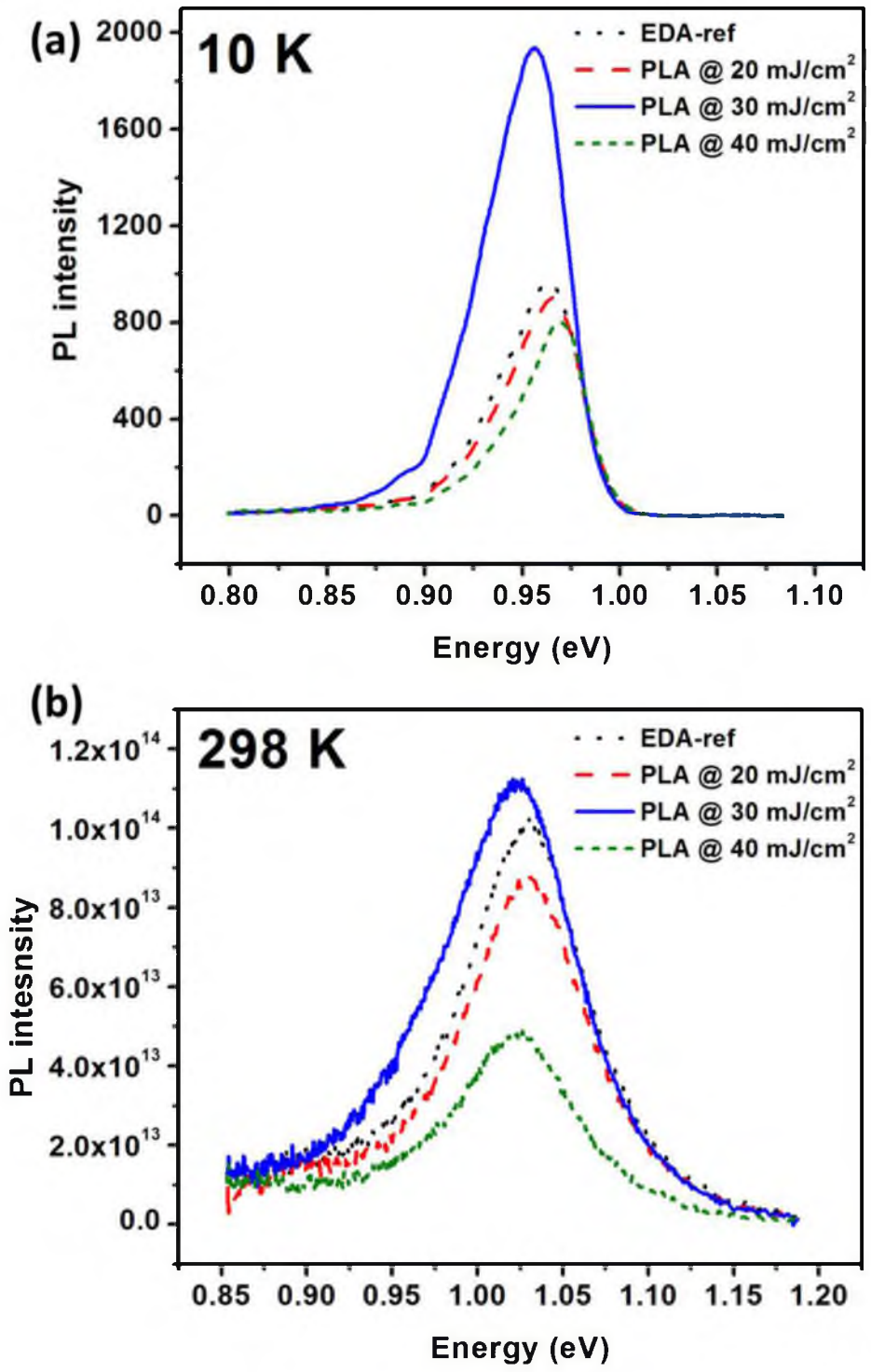

Figure 5.6: PL spectra for EDA-reference and PLA samples recorded at (a) 10 K and (b) 298 K, respectively.

5.6(a) are a result of the other radiative transitions taking place at low temperature. As can be seen from Fig. 5.6(a) the sample laser annealed at 30 mJ/cm^2 shows a broader and relatively higher luminescence yield as compared to the EDA and other PLA samples. A broader spectrum is an indication of compensation of the samples, while the higher luminescence probably indicates annealing of surface states leading to an overall increase in number of radiative transitions.

It is known for Cu(In,Ga)(S,Se)$_2$ family that surface states are detrimental for device performance as they act as nonradiative recombination centers. Since we are using a 248 nm laser which has a small absorption depth it could possibly be annealing out those surface states. A similar observation of reduction in surface states after PLA of single crystal CdTe samples was reported by Gnatyuk et al. [3]. They attributed the increase in photoconductivity signal to a decreased surface recombination rate as a result of removal of oxygen and annealing of structural imperfections. This observation is supported by our Raman data, which shows CuO removal and stress reduction for PLA samples.

Fig. 5.6(b) shows a similar trend in the PL yield to what we observe at low temperature, the only difference being the data at 298 K are a result of band to band transitions. In general, the higher PL yield indicates lower nonradiative recombination suggesting good optoelectronic quality of the absorber layer.

These trends have been observed on two sets of EDA samples synthesized separately and measured at different times. However, in order to build more statistics out of the PL data and affirm that the trends in the PL data are sample specific and not caused by inhomogeneity across the EDA sample or just optical alignment issue, epitaxial samples of CISe (Cu-poor and Cu-rich) were also laser annealed in the low fluence regime and

measured by PL spectroscopy. In order to quantify the net difference between the reference and PLA epitaxial samples, generalized Planck's law [19-21] was applied to the PL spectra of both the Cu-rich as well as Cu-poor samples. The relevant equation is:

$$Y_{PL}(\omega) = C\,A(\omega)\,(\hbar\omega)^2\,\frac{1}{exp\left(\frac{(\hbar\omega-\mu)}{k_bT}-1\right)} \tag{5.2}$$

where Y_{PL} (ω) is the photon flux emitted by the sample, A(ω) is the absorptivity of the sample, $\hbar\omega$ is the photon energy, μ is the Fermi level splitting ($\Delta E_{fn} - \Delta E_{fp}$) and is proportional to the achievable open circuit voltage. The constant C is given by:

$$C = \frac{1}{4\pi^2\hbar^3c^2} \tag{5.3}$$

where $\hbar$ is the reduced Planck's constant and c is the speed of light in vacuum.

For high photon energies, where $\hbar\omega - \mu \gg k_bT$, and the absorptivity approaches unity ($A \approx 1$), equation 5.2 can be written as the following to determine μ:

$$\mu = \hbar\omega - k_bTln\left(\frac{C(\hbar\omega)^2}{Y_{PL}(\omega)}\right) \tag{5.4}$$

Figure 5.7(a) and (b) show the Fermi level splitting for the Cu-poor and Cu-rich epitaxial samples treated at varying laser fluence. Again we see that PLA induces an increase in the Fermi level splitting by about 50 meV for the case of the Cu-poor epitaxial sample. In a PL study by Larsen et al. [19], it was found that spatial variations in epitaxial CGSe samples can cause the μ to vary up to about 7 meV. Since the epitaxial films studied over here have been prepared following similar recipes, we believe that the 50 meV difference between the reference and PLA samples is above the error bars brought about by spatial inhomogeneties.

The average Fermi level splitting is greater in case of Cu-rich samples as compared to Cu-poor samples, which is consistent with the literature results [22]. It is important here

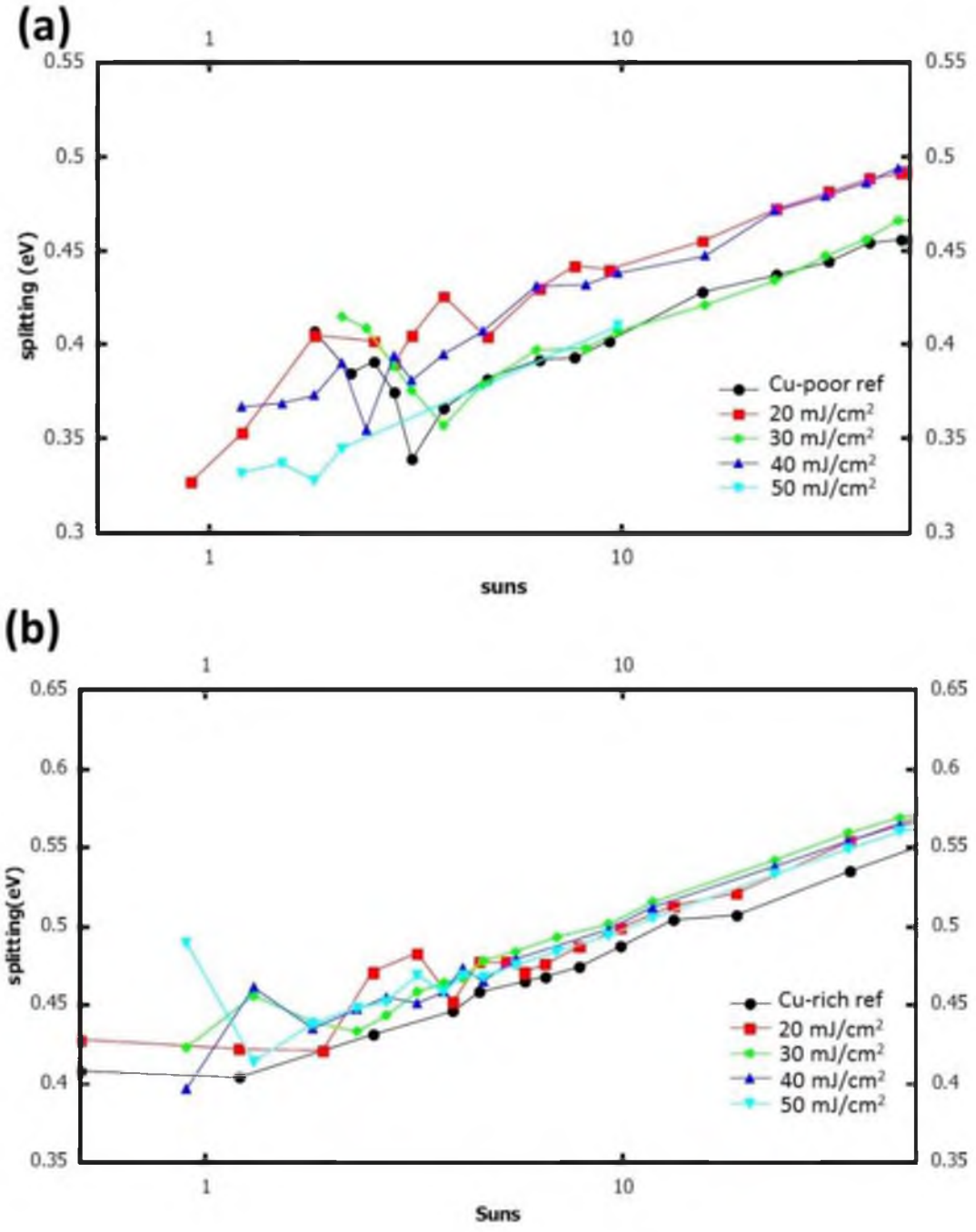

Figure 5.7: Fermi level splitting for (a) Cu-poor and (b) Cu-rich epitaxial samples before and after PLA.

to point out that although Cu-rich samples tend to yield sharp, narrow and well defined PL spectra, the PV devices made out of Cu-rich samples turn out to be inferior to Cu-poor samples which usually show broad PL spectra. For more discussion on Cu-rich vs. Cu-poor samples reader is suggested to read Chapter 4.

5.3.3.2 Electrical characterization

5.3.3.2.1 Capacitance voltage characterization results

Capacitance voltage (C-V) measurements were made on Schottky didoes fabricated on EDA-ref and PLA samples. Figure 5.8 shows the $1/C^2$ vs. V (Mott-Schottky plots) results for these diodes. For Schottky junctions, the slope of the graph is inversely proportional to the net doping concentration and the intercept on the x-axis gives the built-in voltage (V_{bi}). The results of this analysis are tabulated in Table 5.1.

The slopes for the EDA-reference and 30 mJ/cm^2 samples are similar indicating similar net dopant densities near $4x10^{16}$ cm^{-3} while the 40 mJ/cm^2 sample has the highest apparent carrier density of $6x10^{17}$ cm^{-3}. The data for both the 20 mJ/cm^2 and 30 mJ/cm^2 PLA samples show reasonable Schottky barrier heights near 0.6 V while the EDA-reference and the 40 mJ/cm^2 samples indicate $V_{bi} > 4$ V, well in excess of the CISe bandgap and thus indicating perhaps the presence of an insulating oxide and trapped charges at the Al/ CISe interface. However, the 1.2 eV bandgap of CuO is insufficient to explain the $V_{bi} > 1.0$ V for these two samples so other oxides (e.g., In_2O_3) (although not observed in Raman or XRD results) are speculated, as well as a large density of interface states possibly from Se vacancies may have been present for these two samples. While PLA using low fluence conditions, i.e., 20 and 30 mJ/cm2 could cause structural ordering

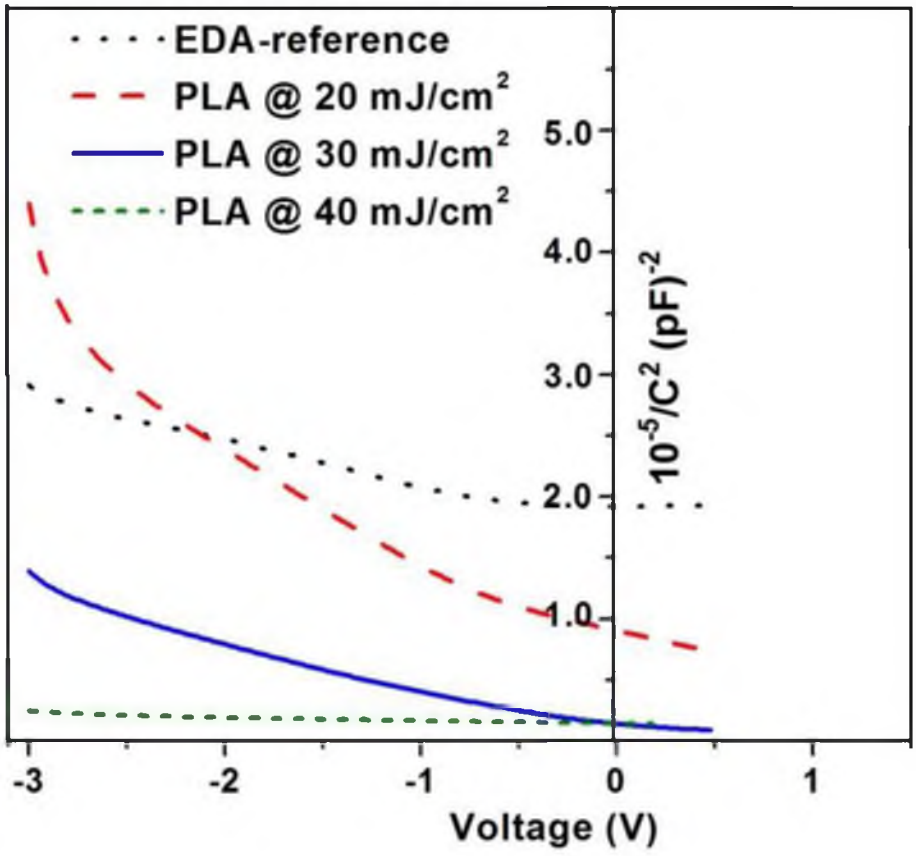

Figure 5.8: Mott-Schottky plots as obtained for Schottky diodes synthesized from EDA-reference and PLA samples when the voltage is varied from -3 to +0.5 V.

Table 5.1: Net carrier concentration values (cm^{-3}) and built-in voltage: V_{bi} (V) as determined from Mott-Schottky plots for EDA-reference and PLA samples.

Sample	**Net carrier concentration (N_a - N_d) (cm^{-3})**	**Built-in voltage :V_{bi} (V)**
EDA-reference	$4x10^{16}$	4.0
PLA @ 20 mJ/cm^2	$2x10^{16}$	0.6
PLA @ 30 mJ/cm^2	$4x10^{16}$	0.5
PLA @ 40 mJ/cm^2	$6x10^{17}$	5.0

[13-14] and thus passivation of these defects leading to improved surface, the high surface temperature during PLA at 40 mJ/cm2 probably caused excessive elemental loss from sample surface thus damaging near surface region and resulting in abnormal Vbi. The surface of the EDA-reference sample had at least surface CuO and possibly other oxides which were apparently removed by the PLA process at 20-30 mJ/cm2. Similar surface cleaning has been reported for PLA of Si [25] as well as CdTe [3]. It is also noted that the PL yield decreased for similar samples irradiated at 40 mJ/cm2.

5.3.3.2.2 DLTS characterization results

DLTS measurements were carried out on the same Schottky diodes to investigate the details of any changes in defect populations brought about by PLA. Figure 5.9 shows the Arrhenius plots as extracted from the capacitance transient data for all of the samples. For all of the samples the capacitance transients were negative indicating that majority carrier defects were being measured. The signal polarity may be inverted resulting in an erroneous assignment of defect type if a large series resistance is present [26-27]. In order to test whether series resistance could be causing this inversion, a 1 kΩ resistor was placed in series with each sample. In all cases this caused the transient's polarity to invert, implying that the sample itself did not suffer from this complication. Thus the assignment of the entire defect states measured in this work as majority (hole) carrier defects for the p-type CISe films is definitive. The extracted defect activation energies for the EDA-reference and 40 mJ/cm^2 PLA samples are very close at ≈ 200 meV, while the 20 and 30 mJ/cm^2 samples exhibited a dominant defect level at ≈ 300 meV. Similar

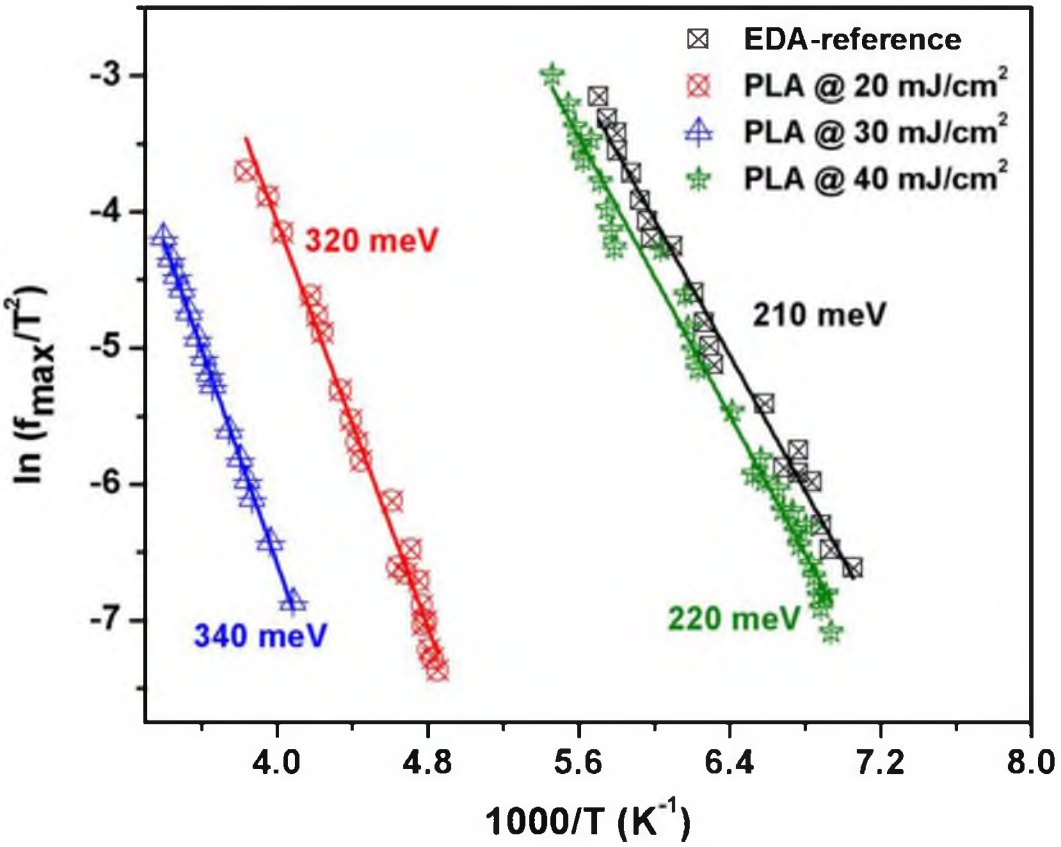

Figure 5.9: Arrhenius plots showing the activation energy of the majority carrier defects (holes) present in EDA-reference and PLA samples.

defect activation energies have been reported earlier by other groups [28-29] for Cu-poor samples.

Table 5.2 gives the values for the apparent concentration of majority defects (N_t) as determined from equation 3.16. The apparent concentration of defects increases monotonically with the fluence, while interestingly both the activation energies and capture cross-sections (also in Table 5.2) indicate that the identity of the dominant defect type changes twice as the fluence increases from 20 to 40 mJ/cm^2. This implies that at least two competing physical effects occur in parallel.

Table 5.2: The activation energy of the defect (meV), capture-cross section (cm^2) and defect concentration (cm^{-3}) for EDA-reference and PLA samples as determined from Arrhenius plots.

Sample	Defect level (meV)	Capture cross-section (cm^2)	Defect concentration (cm^{-3})
EDA- reference	210	$2x10^{-17}$	$1x10^{15}$
PLA @ 20 mJ/cm^2	320	$1x10^{-16}$	$1x10^{15}$
PLA @ 30 mJ/cm^2	340	$2x10^{-17}$	$1x10^{16}$
PLA @ 40 mJ/cm^2	220	$2x10^{-16}$	$4x10^{16}$

Definitive assignment of the actual defects responsible for these activation energies is of course very difficult, but it is plausible if not probable that the ≈ 200 meV defect is caused by indium vacancies $V_{In}(-/0)$ or defect complex associated with vacancy of Se and Cu V_{Se}-V_{Cu} (+/-), given the Cu-poor and Se-poor nature of the samples. On the other hand the ≈300 meV defect is probably caused by copper antisites $Cu_{In}(-/0)$. These tentative assignments were made primarily on the basis of the data presented in Ref. [9, 30].

At first glance, one would assume that since the samples are Cu-poor, indium antisites $In_{Cu}(0/+)$ and copper vacancies $V_{Cu}(-/0)$ should be the dominant point defects. However, counter intuitive defects could be present in samples as has been reported by Stephan et al. [31]. They reported presence of Cu_{In} antisite defects for samples with Cu-poor stoichiometry, as determined from neutron scattering experiments.

In this study, since the measurements were made on Schottky diodes which are majority carrier devices and not p-n junctions (minority carrier devices) the simplest explanation is that majority carrier (hole) defects were measured. Minority carrier injection may be possible for Schottky diodes [32-33] leading to DLTS signals originating from minority carrier defects. This is possible when the Schottky barrier is large and comparable to the bandgap thus allowing minority carrier injection into the semiconductor. However, we can rule this out in the 20-30 mJ/cm^2 samples because of the 0.4-0.5 eV Schottky barrier heights measured in the Mott-Schottky data in Fig. 5.8. For the EDA-reference and 40 mJ/cm^2 samples a risk of minority carrier injection arises based on the C-V data. However the possibility was ruled out by the unambiguous majority-carrier capacitance transients from all of these samples.

As pointed out earlier, the defect present at $\approx$ 200 meV could also be attributed to defect complex associated with V_{Se}-V_{Cu} (+/-), given the Se- and Cu-poor stoichiometry of the films. However this defect is a metastable complex [9] and shows multiple ionization energy states varying from a 100-200 meV acceptor state to a 100 meV donor state. Since these DLTS measurements were not carried out under light nor any light soaking experiments that could induce changes in the material and could possibly expose (if) the metastable nature of this defect state were performed, it is not possible to assign the defect state definitively either to V_{In}(-/0) or V_{Se}-V_{Cu} (+/-). However it is important here to realize that in order to perform any light dependent study the samples should be transparent and not Schottky as is the case here. Again it is worthwhile to mention here that we have over the period of time consistently observed the same activation energy values and the sign of capacitance transient of the defect observed for different EDA-

reference samples. However if the defect state present at 200 meV is attributed to V_{In}(-/0), a plausible hypothesis (discussed below) could explain the changes in the defect spectra as observed here.

Based on the assignments of the dominant defect signals to V_{In}(-/0) in EDA-reference sample and Cu_{In}(-/0) in 20 mJ/cm^2 sample, the most likely explanation for the change in ionization energy is that Cu diffuses to and fills In vacancies converting V_{In}(-/0) to Cu_{In}(-/0). This interpretation is supported by the measured density of defects being identical for these two samples (within experimental error) as shown in Table 5.2. Also, Cu is the fastest-diffusing species in chalcopyrites such as CISe [9]. The origin of the Cu atoms migrating into these V_{In} is unknown – CuO, $Cu_{2-x}Se$, Cu_i, or metallic Cu are all possibilities (although metallic Cu is considered to be very unlikely given the sample preparation). For the 30 mJ/cm^2 sample, it appears that Cu_{In}(-/0) antisites are still the dominant hole defects but their density increases by an order of magnitude. The two ways for this to happen during PLA are via direct formation of Cu_{In}(-/0) or via the formation of V_{In}(-/0) by the removal of In from lattice sites followed by their filling by Cu. It is noted that for Cu/In <1, the calculated formation enthalpy in Ref. [30] for V_{In}(-/0) is lower that of Cu_{In}(-/0). So to first order we would expect that V_{In}(-/0) will form in greater numbers than Cu_{In}(-/0) as the temperature or the fluence is raised.

As mentioned earlier, cooling of a solid sample after ns pulsed laser irradiation is very fast and thus it can be assumed that defect populations formed at high temperature are quickly quenched. However, full thermal equilibrium may not be reached during the laser irradiation and thus the defect populations will be determined by kinetics. Hence thermodynamic driving forces could guide us but predicting actual defect populations is

more complex. It is also noted that the formation of $V_{In}(-/0)$ requires the diffusion of only one atom compared to the direct formation of $Cu_{In}(-/0)$ which requires two atoms to exchange simultaneously and is thus statistically less likely. A plausible, self-consistent picture emerges when the conversion of the dominant defect back to $V_{In}(-/0)$ is considered for the 40 mJ/cm^2 sample and the increase in the net defect density by another factor of ~2 compared to the 30 mJ/cm^2 sample. If we postulate that the primary directly-laser-induced majority defect generation process for all fluences studied herein is the formation of $V_{In}(-/0)$, and that a secondary parallel process of Cu diffusion from a finite reservoir of Cu fills these vacancies to form $Cu_{In}(-/0)$ antisites up to a maximum density of ~10^{16} /cm^3, then the entire range of behavior could be explained.

However, it is intriguing to note that the samples annealed at 20 and 30 mJ/cm^2 have a deeper defect similar to results in Refs. [34-35] which observed a deeper majority carrier defect for material yielding increased photovoltaic device efficiency. It should be pointed out that for low injection conditions, Shockley-Read-Hall recombination rate (see equation 3.1) is maximized not by the defect state being at midgap, but rather by the defect level coinciding with the Fermi level. Therefore this confounding behavior could be possible if the Fermi level is closer to 200 meV defect.

5.3.3.2.3 Current voltage characterization results

In order to further analyze the effects of PLA on the properties of CISe absorber layers, current voltage (J-V) measurements were performed on the complete solar cell stacks made out of EDA CISe and PVD CIGSe samples. Figure 5.10(a) and (b) shows the J-V results on EDA CISe and PVD CIGSe samples, respectively.

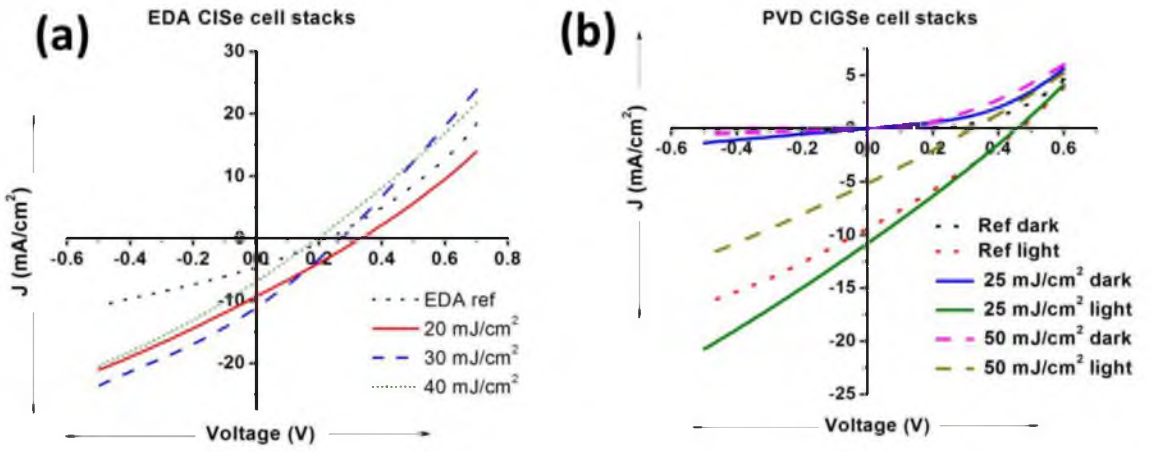

Figure 5.10: J-V results for (a) EDA CISe and (b) PVD CIGSe samples.

Table 5.3 and Table 5.4 give the parameters of the EDA CISe and PVD CIGSe cells, respectively. Although the efficiency of all of the synthesized cells is close to 1%, the trend observed in the change in the efficiency is in agreement with the changes observed in the PL spectra as well as the changes in the parameters of the solar cell as reported by Wang et al. [4]. Unfortunately these fabricated solar cells are not suited for any capacitance spectroscopy and hence defect characterization because the series resistance is high for all of the cells ($\geq$ 10 Ω-cm^2), diode ideality factor >2 and capacitance transients suffer from high noise to signal ratio as well as change their behavior with time. These problems might result in ambiguous interpretation of the data.

Table 5.3: Cell parameters for EDA CISe samples.

Fluence (mJ/cm^2)	**V_{oc} (V)**	**J_{sc} (mA/cm^2)**	**η (%)**
Ref	0.23	4.57	0.29
20	0.33	9.28	0.8
30	0.27	11.07	0.82
40	0.19	6.88	0.34

Table 5.4: Cell parameters for PVD CIGSe samples.

Fluence (mJ/cm^2)	V_{oc} (V)	J_{sc} (mA/cm^2)	η (%)
PVD-Ref	0.46	9.39	1.20
25	0.46	10.79	1.30
50	0.32	5.15	0.43

5.4 Summary

We have carried out pulse laser annealing (PLA) of electrodeposited-furnace annealed (EDA) CISe films at varying fluence (mJ/cm^2) of 20, 30 and 40 mJ/cm^2. Raman spectroscopy and photoluminescence results suggest improvements in structural properties as well as optical properties of the samples after laser annealing at low fluence conditions. These results are in agreement with the results reported earlier for PLA on CIGSe as well as CdTe samples. In order to understand these changes from defect physics point of view, deep level transient spectroscopy (DLTS) was performed on Schottky diodes made out of reference and laser annealed samples. The measurements suggest that the defect level for reference and high fluence sample is at about ≈ 200 meV while the low fluence samples have a defect state at around ≈ 300 meV. Both of these states correspond to majority carrier related defects. We present a hypothesis that possibly explains this behavior and suspect that Fermi level might be residing closer to 200 meV defect state thus maximizing Shockley-Read-Hall recombination rate. Full solar cells made out of PLA absorbers need to be characterized further in order to complement the present work, which will give insights into the changes in minority carrier related defect states.

5.5 References

[1] http://www.empa.ch/plugin/template/empa/3/131438/---/l=2

[2] M.A. Green, K. Emery, Y. Hishikawa, W. Warta, and E.D. Dunlop, Prog. Photovolt: Res. Appl. 20(1) (2012) 12.

[3] V.A. Gnatyuk, T. Aoki, O.I. Vlasenko, S.N. Levytskyi, B.K. Dauletmuratov and C.P. Lambropoulos, Applied Surface Science 255 (2009) 9813.

[4] X. Wang, S.S. Li, C. H. Huang, S. Rawal, J.M. Howard, V. Craciun, T.J. Anderson and O.D. Crisalle, Sol. Energ. Mat. Sol. Cells. 88 (2005) 65.

[5] X. Wang, S.S. Li, C.H. Huang, L.L. Kerr, S. Rawal, J.M. Howard, V. Craciun, T.J. Anderson and O.D. Crisalle, 3rd World Conference on Photovolt. Energ. Convers. 2P-A8-12 (2003) 396.

[6] P.J. Dale, A.P. Samantilleke, G. Zoppi, I. Forbes and L.M. Peter, J. Phys. D: Appl. Phys. 41 (2008) 085105.

[7] S. Siebentritt, N. Rega, A. Zajogin and M. Ch. Lux-Steiner, Phys. Stat. Sol. (c) 1(9) (2004) 2304.

[8] Hung-Ru Hsu, Shu-Chun Hsu, Y. S. Liu, Solar Energy 86 (2012).48.

[9] R. Scheer and H.W. Schock, Chalgogenide Photovoltaics: Physics, Technology and Devices, First edition, Weinheim, Germany : Wiley-VCH, 2011.

[10] A.D. Compaan, I. Matulionis and S. Nakade, Opt. Laser. Eng. 34 (2000) 15.

[11] W. Horig, H. Neumann and I. Godmanis, Solid State Commun. 36:2 (1980) 181.

[12] R.F. Wood and G.E. Giles, Phys. Rev. B. 23(6) (1981) 2923.

[13] G. Vitali, Phys. Lett. 78A(4) (1980) 387.

[14] M. Bertolotti, J. Russ. Laser Res. 6(4) (1985) 395.

[15] http://www.gel.usherbrooke.ca/casino/What.html.

[16] H.F. Goldstein, Dai-sik Kim, P.Y. Yu, and L.C. Bournet, Phys. Rev. B. 41(10) (1990) 7192.

[17] C. Rincon and F.J. Ramirez, J. Appl. Phys. 72(9) (1992) 4321.

[18] E. Ahmed, M. Amar, W. Ahmed, R.D. Pilkington, A.E. Hill, and M.J. Jackson, J. Mater. Engn. Perform.,15 (2006) 213.

[19] J.K. Larsen, L. Gütay, Y. Aida, S. Siebentritt, Thin Solid Films 519 (2011) 7332.

[20] L. Gütay, G.H. Bauer, Thin Solid Films 515 (2007) 6212.

[21] L. Gütay, C. Lienau, G.H. Bauer, Appl. Phys. Lett. 97(5) (2010) 052110.

[22] V. Depredurand, Y. Aida, J. Larsen, T. Eisenbarth, A. Majerus, S. Siebentritt, Conference record of the 37th IEEE-PVSC 2011 proceedings, 337 (2011).

[25] D.M. Zehner, C.W. White, and G.W. Ownby, Appl Phys Lett. 36 (1980) 56.

[26] D.K. Schroder, Semiconductor Material and Device characterization, Third edition, Wiley-Interscience, 2006.

[27] A. Broniatowski, A. Blosse, P.C. Srivastava and J.C. Bourgoin, J. Appl. Phys. 54(6) (1983) 2907.

[28] H.J. Moller and E.M. Rodak, Proc. of 10th Eur. Photovolt. Solar Energ. Conf. (1991) 13.

[29] F.A. Abou-Elfotouh, L.L. Kazmerski, H.R. Moutinho, J.M. Wissel, R.G. Dhere, A.J. Nelson, and A.M. Bakry, J. Vac. Sci. Tecnol. A. 9(3) (1991) 554.

[30] S.B. Zhang, Su-Huai Wei, A. Zunger and H. Katayama-Yoshida, Phys. Rev. B. 57(16) (1998) 9642.

[31] C. Stephan, S. Schorr, M. Tovar and H.W. Schock, Appl. Phys. Lett. 98 (2011) 091906.

[32] F.D. Auret and M. Nel, J. Appl. Phys. 61(7) (1987) 2546.

[33] S.W. Johnston, S.R. Kurtz, D.J. Friedman, A.J. Ptak, R.K. Ahrenkiel, and R.S. Crandall, Appl Phys Lett. 86 (2005) 072109.

[34] S. Kuranouchi and M. Konagai, Jpn. J. Appl. Phys. 34 (1995) 2350.

[35] L.L. Kerr, Sheng S. Li, S.W. Johnston, T.J. Anderson, O.D. Crisalle, W.K. Kim, J. Abushama and R.N. Noufi, Solid State Electron. 48 (2004) 1579.

CHAPTER 6

ELECTRICAL CHARACTERIZATION COMPARISON OF EFFICIENT CIGSe AND CZTSe SOLAR CELLS

6.1 Background and motivation

As mentioned in Chapter 2, $Cu_2ZnSnSe_4$ (CZTSe) is analogus to $CuInGaSe_2$ (CIGSe), where In and Ga are replaced with Zn and Sn. The CZTSe material has a direct bandgap of about 1eV [1-2] and high absorption coefficient ($> 10^4$ cm^{-1}) [3]. Although the efficiency of CZTSSe based materials has reached 11.1% [4], many physical properties of these compounds are still unknown. Furthermore, there is lack of information about the point defects in these absorber materials.

On the other hand CIGSe type solar cells have been a subject of research for more than two decades and the efficiency of the champion cells synthesized in lab has reached 20.4% [5]. Although a lot of research (e.g., Refs. [6-11]) has been focused on understanding the defect physics in these compounds there exists a lot of discrepancy amongst the scientific community as far as the role and assignment of deep defects are concerned.

In this chapter a comparison of the device characteristics of efficient CZTSe and CIGSe solar cells is presented, using various electrical characterization techniques.

6.2 Experimental details

6.2.1 Sample synthesis and preparation

CIGSe based solar cells were acquired from AQT Inc. solar company while CZTSe based solar cells were supplied by NREL. Although the complete details of synthesis of the CIGSe type solar cells is not available, the recipe is similar to what has been reported by Hsu et al. [12], which mainly involves selinization of sputtered metallic precursor of Cu-In-Ga, deposited on top of Mo coated glass at 500°C for about 20 minutes. This was followed by CdS deposition by chemical bath deposition and i-ZnO/n-ZnO by RF sputtering. The fabrication of the CZTSe solar cells is described elsewhere [13]. Briefly, it involves co-evaporation of elemental Cu, Zn, Sn and Se on Mo coated glass at 500 °C for about 40 minutes. This was again followed by the deposition of usual layers i.e. CdS/i-ZnO/n-ZnO.

6.2.2 Characterization techniques

In order to compare the electrical characteristics of the two kinds of cells, various characterization techniques were used. Dark and AM1.5 current density- voltage (J-V) measurements were performed using a Keithley 2400 SMU and an Oriel Sol3A Class AAA solar simulator. Capacitance-voltage (C-V) and DLTS analyses were carried out using a system from Semetrol LLC which incorporates a Boonton 7200 capacitance meter, which operates at 1 MHz. For the DLTS measurements (see Chapter 3 for theory of DLTS) a forward bias filling pulse of +0.1 V (absolute) was applied for 5 ms followed by -0.5 V (absolute) measurement bias for CIGSe cells. The measurement bias for CZTSe solar cells was -0.6 V and a filling pulse of +0.2 V vas applied for 1 ms. Since

the filling pulse is > 0 V, it could lead to injection of minority carriers and hence both types of carriers could be present in this scenario. The minority carrier related defect states will show up under these conditions provided $\sigma_{minority} >> \sigma_{majority}$, as discussed in Chapter 3. The minority carrier DLTS (MCDLTS) was performed using -0.5 V and -0.6 V for CIGSe and CZTSe solar cells, respectively. During the course of measurement, 1 s white light pulses from a LED were used to bias the diode, and the capacitance transients were recorded following the end of the light pulses. The thermal admittance spectroscopy (TAS) (see Chapter 3 for theory) measurements were made using a Quadtech 1920 LCR meter. The DC bias for all TAS measurements was either 0 V or -0.5 V while an AC voltage of 50 mV was used. The frequency of measurements was varied from 20 Hz to 1 MHz. During the course of measurements, the temperature was varied from 50 to 325 K using a closed-cycle He cryostat. Figure 6.1 shows the instrumentation for C-V, DLTS and TAS measurements.

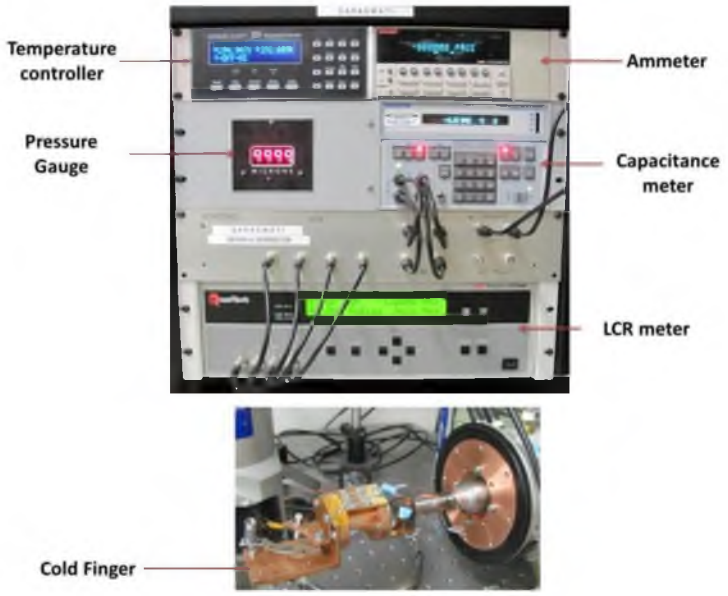

Figure 6.1: Instrumentation and setup for C-V, DLTS and TAS measurements.

6.3 Results

6.3.1 Dark and AM1.5 current density-voltage (J-V) measurements

Table 6.1 summarizes the parameters as extracted from Fig. 6.2, which shows the J-V results for CIGSe and CZTSe solar cells. The parameters were extracted using the CurvA program [14]. As can be seen, the efficiency of both the cells is $5\% < \eta < 10\%$ and have very small series resistance (R_s) making them ideal for defect spectroscopy. The diode ideality factor for both of the devices is $1 < n < 2$, which is usually found for these material types of solar cells. The other difference between the two kinds of cells is the fill factor (FF) which is about 1.3 times larger for CIGSe solar cell and the shunt resistance (R_{sh}) which is again 5 times larger for CIGSe device. A smaller shunt resistance could probably be because of the presence of secondary phases and or disordered phases in case of CZTSe devices [15]. This could possibly cause an order of magnitude larger saturation current J_o (quantifies leakage of a diode) for CZTSe as observed here.

Table 6.1: Parameters for the CIGSe and CZTSe solar cells determined from AM1.5 J-V curves.

Cell parameter	CIGSe	CZTSe
η (%)	9.74	6.27
V_{oc} (V)	0.53	0.35
J_{sc} (mA/cm^2)	28.04	34.5
FF	65.1	51.2
R_s (Ω-cm^2)	0.03	0.05
R_{sh} (Ω-cm^2)	170	34.5
J_o(mA/cm^2)	4.9×10^{-4}	5.3×10^{-3}
Diode ideality factor	1.83	1.68

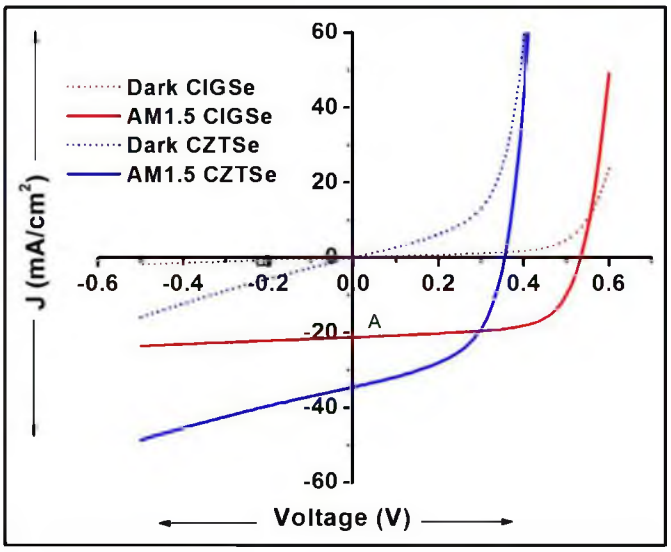

Figure 6.2: J-V dark and AM1.5 curves on CIGSe and CZTSe solar cells.

As discussed in Chapter 1, the theoretical limit on V_{oc} is set by the band gap of the material. However, the nonideal factors (recombination, etc.) contribute to losses and hence a rule of thumb is that the maximal V_{oc} for good p-n junction solar cells is approximately 0.4 V smaller than E_{gap}/e [6]. In this case we see that for CZTSe solar cells the V_{oc} is atleast 40% lower than the expected value while it is only about 25% lower in case of CIGSe cells. The differences in R_{sh} or J_o could possibly be contributing to the losses observed here.

6.3.2 Capacitance-voltage (C-V) measurements

Figure 6.3 shows the net carrier concentration (N_{net}) vs depth for both type of solar cells. In order to generate these plots we could use the following equation which states that:

$$N_{net} = -\frac{2}{\varepsilon A^2 q} \frac{d\left(\frac{1}{C_{depletion}^2}\right)}{dV} \qquad (6.1)$$

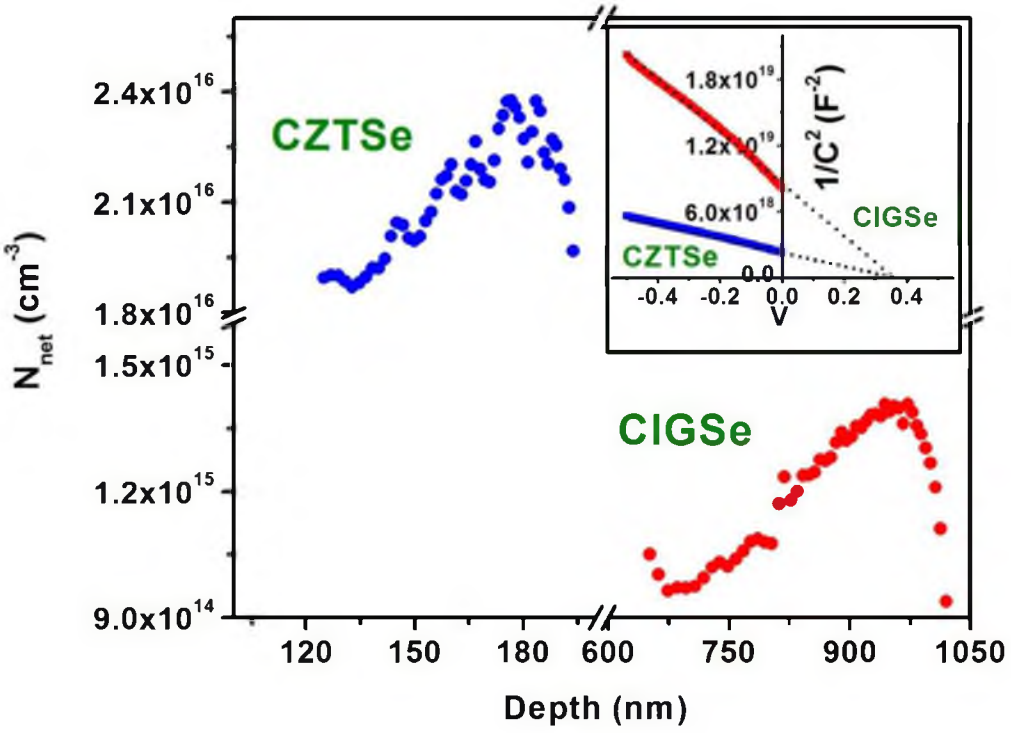

Figure 6.3: Net carrier density profiles extracted from the C-V measurements on CIGSe and CZTSe solar cells. Inset shows the Mott-Schottky plots in order to determine the built-in voltage for the respective cells.

The above equation could be derived by differentiating equation 1.3 two times. When we change the applied bias from equilibrium (0 V) to more negative, we increase the depletion width and hence by continuously increasing the bias (more negative) we could probe deeper into the device starting from the edge of the space charge region. An important thing to keep in mind is that this analysis is good only in the reverse bias region and not in the forward bias region. This is because the depletion capacitance accounts for most of the junction capacitance when the junction is in the reverse bias. In the forward bias regime, in addition to the depletion capacitance, the capacitance of the device has contribution from diffusion capacitance as well, which arises from the rearrangement of minority carriers [16].

The N_{net} actually represents the apparent or effective carrier density. It is a measure of the net ionized concentration of the defects in the space charge region [17]. As can be seen, the shape of the curves for both of the cells looks identical, except for order of magnitude higher carrier densities for CZTSe solar cell. The apparent increase in N_{net} with depth for both of the samples could possibly be because of the contribution from incompletely ionized deep defect state. The inset to the figure shows the Mott-Schottky curve, intercept of which on the X-axis gives the value of the built-in voltage (V_{bi}, as per equation 1.3). The V_{bi} for both of the cells is around 0.35 V. One difference between the two solar cells is the depletion width at equilibrium (no bias). The depletion width for CIGSe solar cells is about ≈ five times larger than CZTSe solar cells. One of the factors that causes this difference is the larger net carrier density for CZTSe cell, which is inversely related to depletion width (see equation 1.2).

These all factors are significant from device performance point of view because for good optoelectronic performance one aims for a larger depletion width, smaller J_0 and larger R_{sh}. These all parameters cumulatively determine the probability of minority carrier collection i.e. transfer of minority carrier to the other side of junction thus making them majority carriers (see Chapter 1). And hence CIGSe solar cell looks promising from this point of view.

6.3.3 Thermal admittance spectroscopy (TAS) measurements

The basic principle of TAS measurements was discussed in Chapter 3. Both of the cells underwent TAS measurements made at 0 V DC bias and 50 mV AC bias in a temperature range of 50 K to 325 K. Figure 6.4 (a, b) shows the C-f curves for the

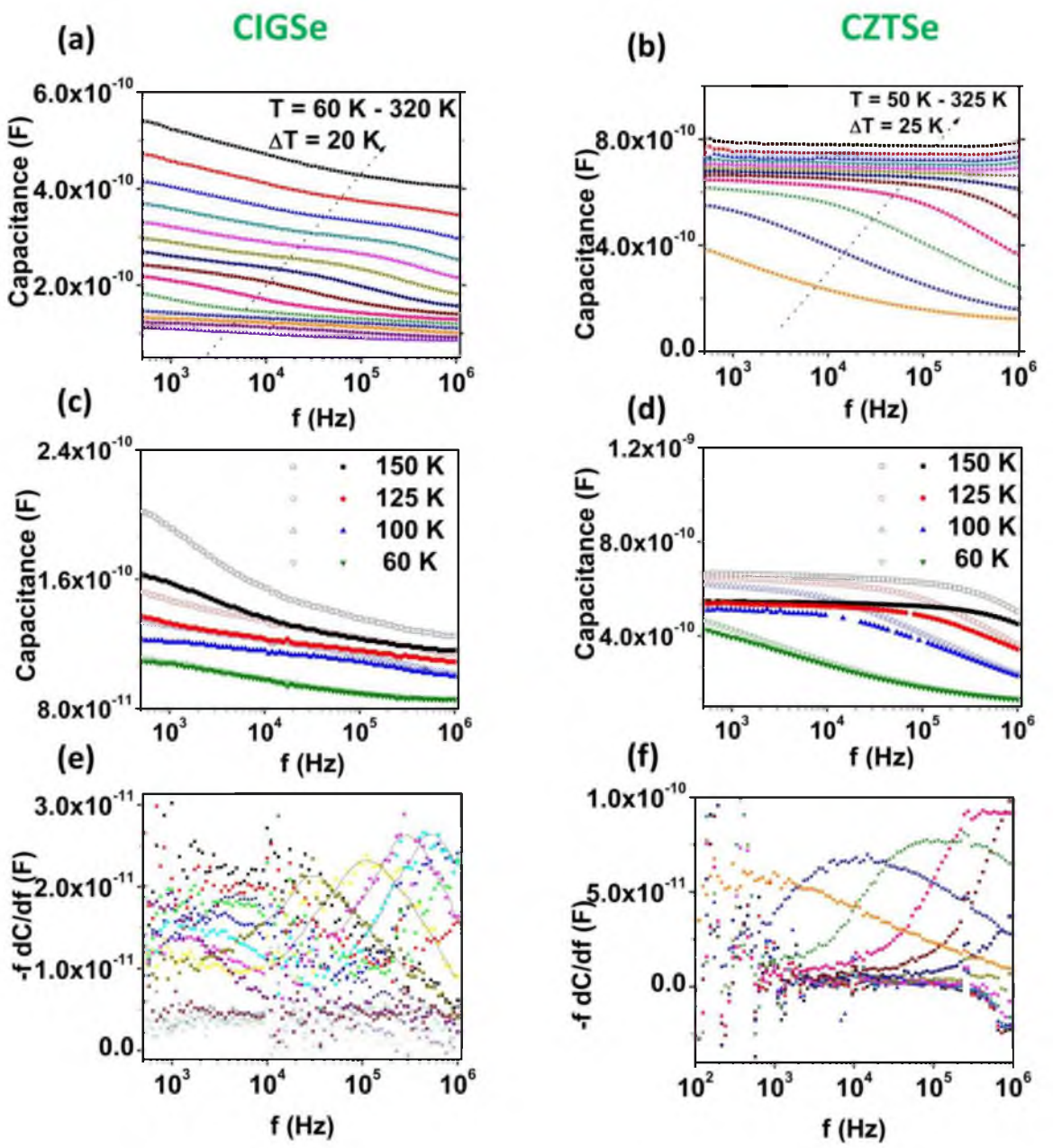

Figure 6.4: TAS data analysis on CIGSe and CZTSe solar cells. Figures (a) and (b) show the capacitance variation with frequency at different temperatures at 0 DC bias and 50 mV AC bias. Figures (c) and (d) show the capacitance variation with frequency below 150 K. Open symbols represent measurements at 0 DC bias and 50 mV AC bias while filled symbols represent measurements at -0.5 DC bias and 50 mV AC bias. Figures (e) and (f) show the differentiated capacitance spectra for both of the cells.

CIGSe and CZTSe solar cells. As can be seen, the C-f spectra for both of the samples look quite distinct. Firstly, the capacitance of the CIGSe cell at higher temperatures decreases with increasing frequency and decreasing temperature. However, no clear step in the C-f spectra is observed at higher temperatures for CIGSe solar cell. For the temperatures below 140 K, capacitance changes only slightly with decreasing temperatures and increasing frequency. This kind of behavior can also be seen in the TAS data reported by Walter et al. [18] for CIGSe. Thus for the interpretation of defects from TAS data, only the region $\geq$ 140 K should be considered. Comparing the C-f spectra collected at 0 and -0.5 DC bias (Fig. 6.4(c)), the spectra at the two biases start to converge only around 100 K. This shows that in this regime ($T < 100$ K and frequency $\geq$ 1 MHz), the capacitance is independent of applied bias, space charge region behaves as an insulator and the capacitance response is a consequence of dielectric freezeout and not a response of deep defect state [19-21].

On the other hand, for CZTSe cells (Fig. 6.4(b)) at high temperatures the capacitance changes only slightly with decreasing temperatures and increasing frequency. It is only below 200 K that we start to see a large drop in capacitance with decreasing temperature and increasing frequency. Again for region $\leq$ 150 K, capacitance curves start to converge and become independent of the applied bias (Fig. 6.4(d)) for certain frequency ranges which change with temperature. This again is a consequence of dielectric freezeout and hence this region should not be considered for interpretation of defect states from TAS data.

In order to find the inflexion point and hence the peaks (see Chapter 3), the capacitance spectrum is differentiated with respect to frequency (see Fig. 6.4(e) and (f)).

While for CIGSe cell we could deduce a set of (f, T) points corresponding to different peaks above 140 K, the analysis of CZTSe cell results in peaks only below 150 K. This region for CZTSe cell could not be used for data interpretation as it is a consequence of dielectric freezeout and not a response from a defect state. Hence TAS analysis on CZTSe sample unravels no peaks.

Following the procedure outlined in Chapter 3, we could determine density of states for CIGSe sample (Fig. 6.5). The peak position is at about ≈ 150 meV and the defect state is usually referred to as N1 defect. This defect energy position has been reported earlier by different groups [6] and there is still a debate on the interpretation and the effect of this state on the cell performance. Since the purpose of this study is to compare

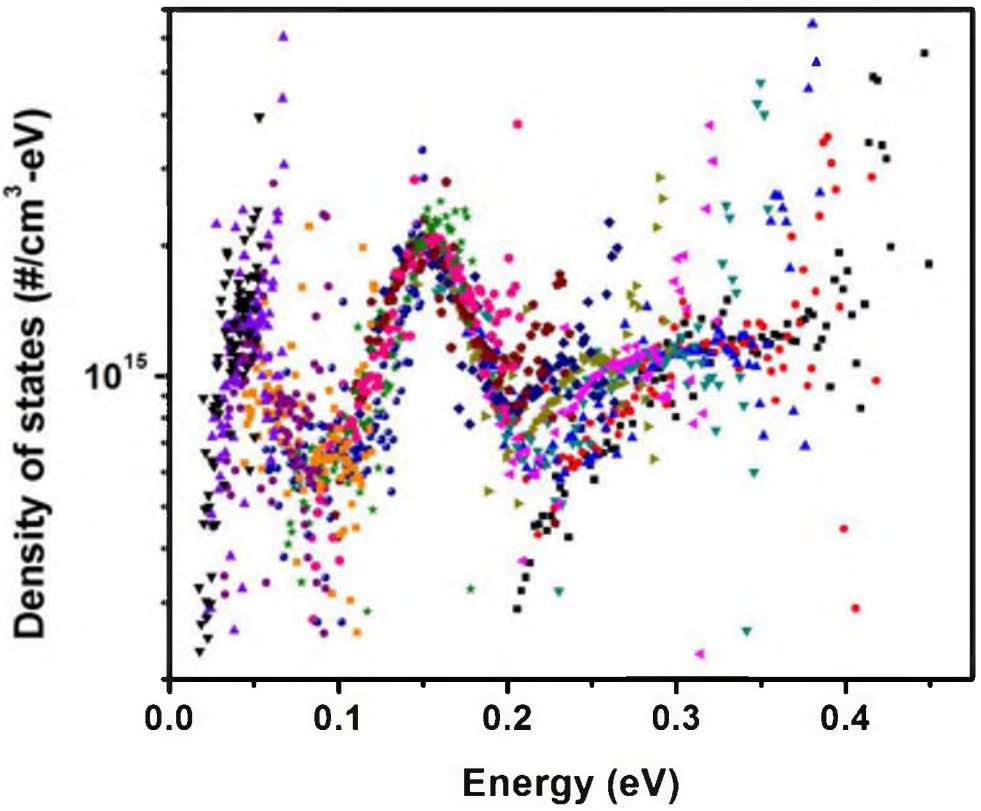

Figure 6.5: Density of states extracted from TAS analysis on CIGSe solar cell. For the defect analysis, only the data at higher temperatures were used (as explained earlier).

the characteristics of CIGSe and CZTSe cells, we do not assign this defect state to any particular kind of defect and just report the energy value.

6.3.4 Deep level transient spectroscopy (DLTS) and minority carrier deep level transient spectroscopy (MCDLTS) measurements

The physics behind the DLTS and MCDLTS spectroscopy was discussed in Chapter 3. A common feature for both the CIGSe and CZTSe cells is that in the DLTS spectrum the peaks/valleys observed are relatively broad, extending over a large temperature range (> 100 K) (see Fig. 6.6). Igalson et al. [22] have attributed this behavior to non-exponential capacitance transients caused by a hyperbolic process of recombination which contributes to the transients apart from the thermal emission from traps.

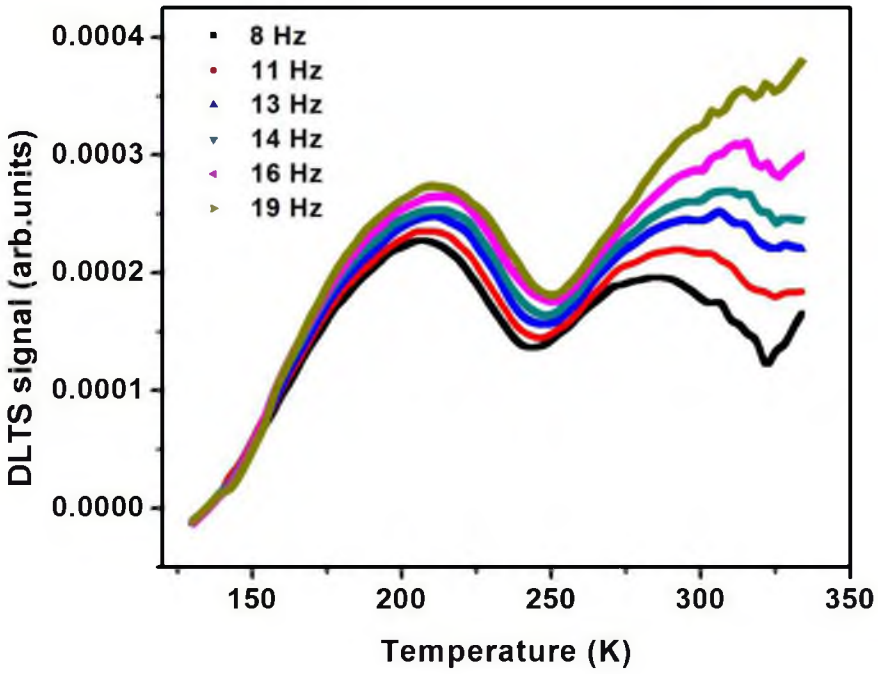

Figure 6.6: DLTS spectrum for CZTSe cell.

The other possibility for the broad DLTS signal observed in these material systems could probably be related to a distribution of defect states and band tails extending into the forbidden gap region. It is known that these material systems possess a large number of shallow defect states which give them smeared band edges and give them an effective (reduced) bandgap rather than a sharp band edge [6, 15, 23]. It is quite possible that a superposition of all these factors results in a broad signal observed here. Also it is argued that this process is a specific material property, depending only indirectly on the interface properties or junction quality.

The DLTS data analysis on CIGSe and CZTSe cells reveals majority carrier related defects located at $\approx$ 550 meV (around mid-gap) for CIGSe and two defect levels for CZTSe located at $\approx$ 350 meV and $\approx$ 600 meV. The respective capture-cross sections and concentrations are reported in Fig. 6.7. In order to test whether series resistance could be causing signal inversion, a 0.5 kΩ resistor was place in in series with each sample. In all cases this caused the transients' polarity to invert, implying that the sample response rather than the equivalent circuit response is causing the observed signal. Thus the assignment of all of the defect states measured in this work as majority (hole) or minority (electron) carrier defects is definitive.

A similar defect level situated at around 550 meV related to majority carrier defect has been reported earlier by different groups for CISe as well as CIGSe [24-29]. This defect level could possibly be because Cu_{In} (-/-2) or O_{Se} (-/0) [6, 30]. As discussed in Chapter 5, the interpretation and origin of any defect level is difficult especially if the complete history of the sample is unknown. Since no exact details are available about the CIGSe precursor layers, we think more work is warranted in order to definitively assign

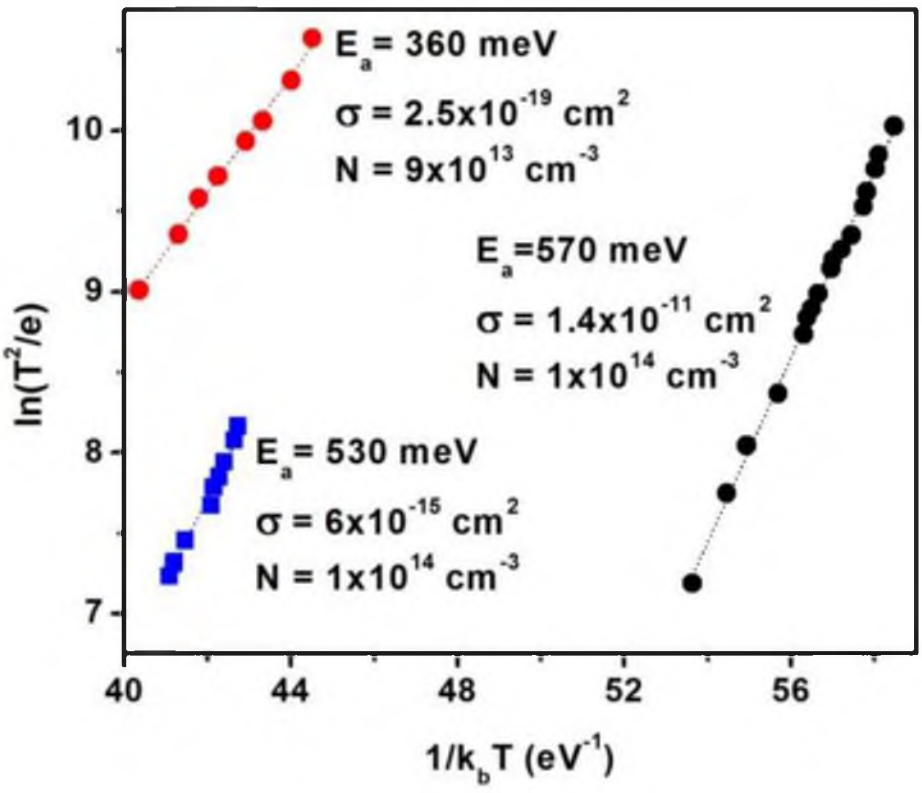

Figure 6.7: Arrhenius plot for DLTS data on CIGSe and CZTSe solar cells. Solid circles (●, ●) represent data for CZTSe cells and solid square (■) represent data for CIGSe cells, respectively.

these defect levels to certain defect states that have been theoretically calculated.

On the other hand the assignment of the defect levels in CZTSe is complicated by the fact that there is a lack of theoretical and experimental work related to deep defects in CZTSe. However, interpretation of these defect levels based on Ref. [31] is in progress and will be published soon [32].

MCDLTS study was performed on both the CIGSe and CZTSe solar cells. Figure 6.8 shows the capacitance transients collected for the CZTSe solar cell. As can be seen, the positive capacitance transient arises only when the light is switched off and no transient is present in dark. This interpretation is consistent with the theory and hypotheses discussed in Chapter 3 making us believe that the capacitance transient in this case either

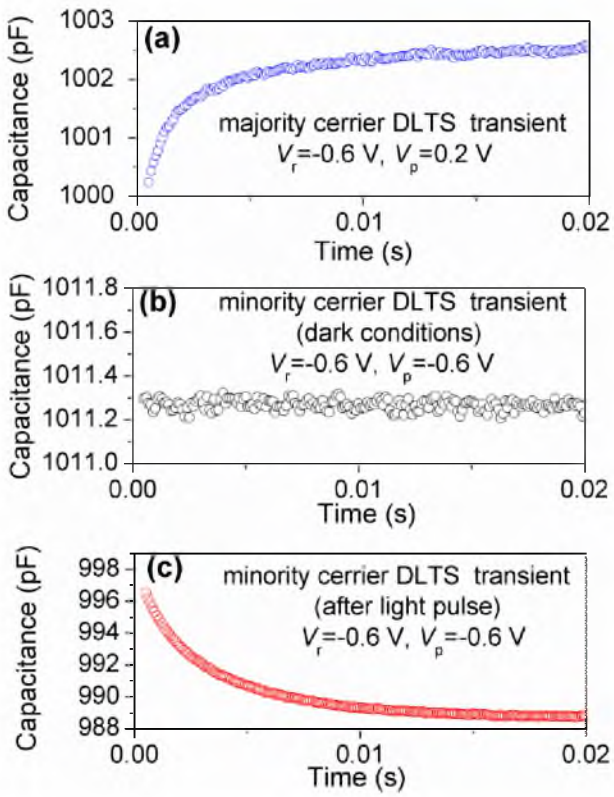

Figure 6.8: The capacitance transients under the reverse bias V_r =-0.6 V: (a) after the voltage pulse V_p=0.2 V (majority carrier DLTS), (b) after the voltage pulse V_p=-0.6 V without light pulse (minority carrier DLTS), (c) after the voltage pulse V_p=-0.6 V synchronized with light pulse (minority carrier DLTS).

corresponds to a recombination center or a minority carrier related defect. The calculated value of ionization energy of the defect state is this case is around ≈ 650 meV from the conduction band (Fig. 6.9). Since the sum of defect level measured using DLTS and MCDLTS is close to band gap of CZTSe (≈ 0.35 + 0.65 =1 eV), we speculate that the defect level being measured here may be a recombination center (see Chapter 3), which can interact with both majority and minority carriers and thus affect the device performance. A similar behavior has been reported earlier by Johnston et al. [33] for Schottky diodes synthesized using InGaAsN/Au. They observed that as the electron injection was increased, the behavior associated with the hole defect changed to electron

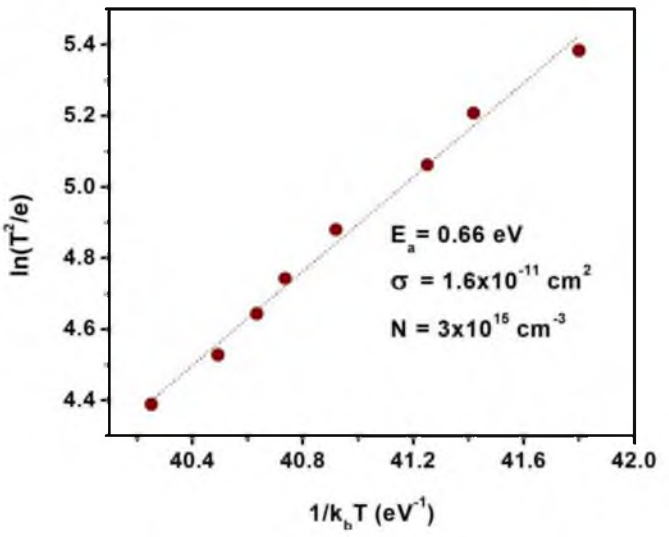

Figure 6.9: Arrhenius plot for MCDLTS data on the CZTSe solar cell.

trap, thus confirming recombination center theory hypothesis. The MCDLTS study on CIGSe solar cell resulted in large values of ionization energies as well as capture cross section making the data unreliable.

6.4 Summary

In this study, the electrical characteristics of CIGSe and CZTSe solar cells were measured and compared using current-voltage (J-V) measurements, capacitance-voltage (C-V) measurements, thermal admittance spectroscopy (TAS), deep level transient spectroscopy (DLTS) and minority carrier deep level transient spectroscopy (MCDLTS). It is found that shunt resistance is about 5 times larger and saturation current is an order of magnitude smaller for CIGSe cells in comparsion to CZTSe cells as determined from AM1.5 J-V measurements. The C-V measurements suggest 5 times larger depletion width for CIGSe cells. These all factors could possibly contribute to easy minority carrier transport in case of CIGSe cells in comparison to CZTSe cells.

TAS measurements reveal that dielectric freezeout occurs at much higher temperatures (≈ 150 K) and lower frequency (< 1MHz) in case of CZTSe cells. The DLTS signal for both kinds of samples results in a broad peak/valley. This probably indicates some parallel recombination process occurring with carrier emissions or a distribution of closely spaced defect states contributing to the DLTS signal. A recombination center is speculated for CZTSe cell based on the MCDLTS results.

6.5 References

[1] M. Grossberg, J. Krustok, K. Timmo, M. Altosaar, Thin Solid Films 517 (2009) 2489.

[2] J. Krustok, R. Josepson, T. Raadik, M. Danilson, Physica B 405 (2010) 3186.

[3] K. Ito, T. Nakazawa, Japanese Journal of Applied Physics 27 (1988) 2094.

[4] T.K. Todorov, J. Tang, S. Bag, O. Gunawan, T. Gokmen, Y. Zhu, D.B. Mitzi, Adv. Mater 3 (2013) 34.

[5] http://www.empa.ch/plugin/template/empa/3/131438/---/l=2.

[6] R. Scheer and H.W. Schock, Chalgogenide Photovoltaics: Physics, Technology and Devices, First edition, Weinheim, Germany : Wiley-VCH, 2011. Also see mentioned references in same.

[7] M. Igalson and H.W. Schock, J. Appl. Phys. 80(10) (1996) 5765.

[8] G. Dagan, F. Abou-Elfotouh, D.J. Dunlavy, R.J. Matson and D. Cahen, Chem. Mater. 2(3) (1990) 286.

[9] S. Siebentritt, N. Rega, A. Zajogin, and M.Ch. Lux-Steiner, Phys. Stat. Sol. (c). 1(9) (2004) 2304.

[10] M. Igalson, A. Urbaniak, A. Krysztopa, Y. Aida, R. Caballero, M. Edoff and S. Siebentritt, Thin Solid Films 519 (2011) 7489.

[11] A. Krysztopa, M. Igalson, P. Zabierowski, J. Larsen, Y. Aida, S. Siebentritt and L. Gütay, Thin Solid Films 519 (2011) 7308.

[12] Hung-Ru Hsu, Shu-Chun Hsu, Y.S. Liu, Solar Energy 86 (2012) 48.

[13] I. Repins et al., Solar Energy Materials & Solar Cells 101 (2012) 154.

[14] Procedure outlined in: Steven S. Hegedus and William N. Shafarman, Prog. Photo.: Res. and Appl. 12 (2004) 155.

[15] M.J. Romero, I. Repins, G. Teeter, M.A. Contreras, M. Al-Jassim and R. Noufi, Conference Record of the 38th IEEE-PVSC 2012 Proceedings, 1580 (2012).

[16] S.M. Sze and K.K. Ng, Physics of Semiconductor Devices, Wiley India Pvt. Ltd., Third edition, 2009.

[17] D.K. Schroder, Semiconductor Material and Device Characterization, Third edition, Wiley-Interscience, (2006).

[18] T. Walter, R. Herberholz, C. Muller and H.W. Schock., J. Apply. Phys. 80 (1996) 4411.

[19] O. Gunawan, T. Gokmen, C.W. Warren, J.D. Cohen, T.K. Todorov, et al., Appl. Phys. Lett. 100 (2012) 253905.

[20] J.W. Lee, J.D. Cohen, and W.N. Shafarman, Thin Solid Films 480 (2005) 336.

[21] Joachim Kneisel, Kai Siemer, Ilka Luck, and Dieter Braunig, J. Appl. Phys. 9 (2000) 5474.

[22] M. Igalson and R. Bacewicz, Eleventh E.C. Photovoltaic Solar Energy Conference; Proceedings of the International Conference, held at Montreux, Switzerland, 12-16 October 1992.

[23] S. Siebentritt and U. Rau, Wide-gap Chalcopyrites, First edition, Springer Series in Materials Science, 2005.

[24] H.J. Moller, E.M. Rodak, Proc. 10th European Photovoltaic Solar Energy Conf. p. 913 (1991).

[25] L.S. Yip, W.S. Weng, L. Li, I. Shih, and C.H. Champness, Tenth E.C. Photovoltaic Solar Energy Conference; Proceedings of the International Conference, held at Lisbon, Portugal, 8-12 April 1991.

[26] T.R. Hanak. A.M. Bakry, D.J. Dunlavy, Abou-Elfotouh, R.K. Ahrenkiel. M.L. Timmons, Solar Cells 27 (1989) 347.

[27] H. Wang, PhD Thesis, McGill University, Montreal, Quebec, Canada (2001).

[28] A.L. Li and I. Shih, J. Electron. Mater. 22 (1993) 195.

[29] L.L. Kerr, Sheng S. Li, S.W. Johnston, T.J. Anderson, O.D. Crisalle, W.K. Kim, J. Abushama and R.N. Noufi, Solid State Electron. 48 (2004) 1579.

[30] S.B. Zhang, Su-Huai Wei, A. Zunger and H. Katayama-Yoshida, Phys. Rev. B. 57:16 (1998) 9642.

[31] Shiyou Chen, Aron Walsh, Xin-Gao Gong and Su-Huai Wei, Adv. Mater. 2013, DOI: 10.1002/adma.201203146.

[32] V. Kosyak, A. Bhatia, E.A. Lund, M.A. Scarpulla, I. Repins, Appl. Phys. Lett., In preparation.

[33] http://www.nrel.gov/docs/fy03osti/33557.pdf

CHAPTER 7

CONCLUSIONS AND FUTURE WORK

This chapter summarizes the conclusions of the research undertaken and also proposes the future avenues that might be explored based on this work.

7.1 Chapter 1 through Chapter 3

Chapter 1 provides an overview of semiconductor physics followed by photovoltaic principles in general and the effect of various parameters on photovoltaic cell performance.

This is followed by literature review of Cu based thin film photovoltaic materials in Chapter 2. It highlights the various aspects of polycrystalline CIGSe and related materials which make them special and discusses the reasons why polycrystalline materials outperform their epitaxial counterparts. Most importantly, the low formation energy of native point defects results in creation and interaction of electrically benign defect clusters and also ordered vacancy compounds (n-type) if the film is non-stoichiometric. The ordered vacancy compounds are segregated at the surface and perhaps intergranular interfaces mainly affecting the valence band by creating a barrier for holes. This helps in lowering the recombination rate at grain boundary since the probability of finding an electron as well as a hole at the same time is reduced. The role

of various material layers that go into making a complete CIGSe type solar cell is discussed followed by the physics of an actual CIGSe type solar cell. The formation of ordered vacancy compounds coupled with Cd diffusion in CIGSe results in type inversion at the interface of CdS/CIGSe and hence formation of a buried p-n junction which suppresses recombination at the metallurgical interface. A quick comparison is provided between CIGSSe and CZTSSe type materials, which are believed to possess similar characteristics. However the main difference so far appears to be the smaller region of stability of CZTS as compared to CIGSe. This is followed by the discussion on thermodynamic principles of electrochemical deposition and theory of laser annealing.

Chapter 3 begins with a general discussion on defects in a material system followed by the theory and physics behind advanced characterization techniques such as deep level transient spectroscopy (DLTS) and thermal admittance spectroscopy (TAS) that can be used to characterize deep defect states in a semiconductor. In general, both DLTS and TAS rely on measuring changes in the capacitance of the p-n junction. The main difference being that DLTS measures the capacitance transient when a diode is switched from a positive, zero or slightly negative bias to more reverse bias, while TAS measures the absolute capacitance of the junction when the frequency of the applied AC voltage is varied. The optical variant of DLTS, i.e., minority carrier deep level transient spectroscopy (MCDLTS) that may be used to characterize minority carrier related defects is also discussed.

7.2 Chapter 4

7.2.1 Summary and conclusions

Chapter 4 deals with laser annealing of as-electrodeposited CISe films in order to investigate the possibility of a complete nonvacuum synthesis route of synthesizing device quality CISe films by coupling electrochemical deposition with laser annealing. Different annealing conditions such as wavelength of laser (248 nm and 1064 nm), operating mode of the laser (pulsed and continuous), energy/power densities, annealing time and number of pulses were the variables for the experiments. It is found that CISe films dewet on top of Mo, $MoSe_2$ and Cu if melted. Although crystallinity may be improved by passing through a liquid phase having high mass transport mobilities, in this case the dewetted films cannot be used for making solar cells because of severe shunting. In the submelting regime of PLA using a 1064 nm laser, no change is seen in crystalline quality using XRD. Thus we conclude that no PLA processing window for structural modification of as-electrodeposited $CuInSe_2$ absorber films exist for lasers with similar parameters.

Continuous wave laser annealing (CWLA) using 1064 nm laser in submelting regime improves crystallinity of samples while dewetting has been avoided. These results are better than what has been reported earlier, because no secondary phases related to oxides and or selenides are observed. However, for the same CWLA conditions the peak FWHM narrowing is more pronounced in Cu-rich samples ($\approx$ 80% reduction) as against Cu-poor samples ($\approx$ 40% reduction). The probable reasons for the difference in behavior of the samples have been mentioned, one of them being higher absorption coefficient for Cu-rich samples which translates into higher temperatures. The dwell time of the laser

while achieving similar increases in crystalline perfection was reduced to 1 s by increasing the power density to approximately ≈ 1000 W/cm^2. However a key issue to be addressed is the Se loss from the samples which is detrimental for device performance.

7.2.2 Future work related to Chapter 4

One experiment that needs to be tried is having a heated glass window on top of the CISe film which could induce a Se vapor pressure on top of the CISe film if the temperature of the heated glass is around ≈ 200 °C. If the glass window is coated with n-ZnO or fluorinated tin oxide (FTO) or a similar material, Ohmic heating of the conductive film might help achieve the above mentioned conditions. Also, in order to increase the coupling between the 1064 nm laser radiation and CISe film, heating the sample from the back side during the course of annealing could be tried. This might help in the reduction of the laser power density employed for annealing if surface damage is suspected by high power densities employed in laser annealing.

Working in melting regime is possible only if we change the back contact layer. As highlighted in Chapter 2 and 4, W has been shown equivalent to Mo, as far as the electrical properties to the CIGSe devices are concerned. The good thing is that W has higher surface energy than Mo, which makes us think that CISe has lower probability of dewetting on W.

Lastly a full finite element model should be developed combining both electromagnetic interactions and heat flow in order to estimate the temperature of the sample during any arbitrary laser annealing process. As mentioned in Chapter 4, due to incomplete and weak absorption of 1064 nm laser the heat generation function inside the

film is complicated and the correct way to estimate the temperature during CWLA using 1064 nm laser would be solve the time dependent EM wave interaction with the sample which dissipates power as it travels through the test structure.

Some initial steps have been made in this direction in the course of this research. However, problems like scaling of the geometry and selection of the appropriate boundary conditions for heat flow must be resolved and the model be verified by experiments. A few things that need to be tried are making the air column in front of the CISe film infinite in thickness making the mesh denser at the Air/CISe interface, taking into account rastering of the laser beam and making a full 3-D model. One more thing that could be added to the model is the phase transition phenomena and the diffusion of species.

7.3 Chapter 5

7.3.1 Summary and conclusions

Chapter 5 of thesis discusses the research work on pulsed laser annealing (PLA) of previously annealed CIGSe type films. It was found (by peak shift in Raman spectroscopy) that PLA of CISe films in low fluence (mJ/cm^2) regime results in increased structural ordering. Changes in optoelectronic properties such as minority carrier lifetime for CIGSe and photoconductivity of CdTe films after PLA, has been reported previously by different groups. However, no complimentary defect study has been performed. We saw an increase in the photoluminescence yield for low fluence treatment which suggests reduction in nonradiative recombination, while high fluence treatment could damage the sample surface resulting in a decrease in the PL yield. Also observed is the expected

increase in the V_{oc} for epitaxial Cu-poor as well as Cu-rich epitaxial CISe samples related to this increased PL yield.

This was followed by characterization of reference and PLA Schottky diodes (Al/CISe) using DLTS technique. Signatures of dominant hole traps with transition energies of 210-220 meV for unirradiated samples and for those irradiated at 40 mJ/cm^2 and 320-340 meV for samples irradiated at 20 and 30 mJ/cm^2 were identified. The trap level at $\approx$ 200 meV may correspond to either V_{In}(-/0) or V_{Se}-V_{Cu} (+/-) transitions indicating the dominance of these defects, while the defect level at $\approx$ 300 meV correspond to Cu_{In}(-/0) point defect. A hypothesis is presented to explain the non-monotonic changes in the dominant defect populations versus laser fluence in which the two primary effects of the laser irradiation on point defect populations are the formation of V_{In} (assuming V_{In} defect at $\approx$ 200 meV) accompanied by diffusion of Cu in the film which forms Cu_{In} antisites. This hypothesis may explain the observations that the apparent concentration of majority carrier traps increases monotonically with fluence but that the identity of the dominant traps changes. Further work is required to fully understand all of the competing effects of PLA on device performance including those related to changing defect populations.

7.3.2 Future work related to Chapter 5

In order to correlate the device performance with the defect states and their populations, characterization of minority carrier related defects is warranted using MCDLTS technique. An initial step in that direction has been made by starting to characterize full solar cell stacks synthesized using reference CIGSe films as well as laser

annealed films. The device parameters deduced from the current density- voltage (J-V) results also suggest the same trend, i.e., low fluence treatment improves the absorber while high fluence treatment damages the surface resulting in deteriorated performance. However, the series resistance of the synthetized cells is large and as well, the room temperature capacitance transients are noisy and change behavior with time. These problems might result in ambiguous interpretation of the DLTS data. Hence the future work in this direction should focus on firstly trying to optimize the deposition of the solar cell stack, i.e., finding the correct parameters of deposition for CdS/i-ZnO/n-ZnO layers. The aim should be to get reasonable device parameters ($R_s < 1\ \Omega/cm^2$ and diode ideality factor < 2) rather than matching the champion cell efficiency of the cells, synthesized using the similar absorber layers. This is because efficiency of a cell could be affected depending on the deposition parameters of buffer and window layers. So as long as the diode parameters are good and the reference and PLA films undergo cell completion by identical procedure (ideally simultaneously) there is minimal chance of inducing errors and/or misinterpretation of the collected data.

Other experiment that could be of interest is the PLA of full cell stack using 1064 as well as 532 nm laser. Preliminary results suggested improvements in I_{sc} (or J_{sc}) of the sample after PLA at around 75 mJ/cm^2 using 1064 nm laser (Fig. 7.1(a)). One of the possible reasons for this to happen is by the reduction in the series resistance of n-ZnO. The 1064 nm radiation could be absorbed by ZnO via free carrier absorption mechanism, resulting in more capture of photons by CIGSe and hence an increase in J_{sc}. However one has to be careful while interpreting the data as poor electrical connections between the probe and metal pads on the sample might induce changes in fill factor (FF) (see

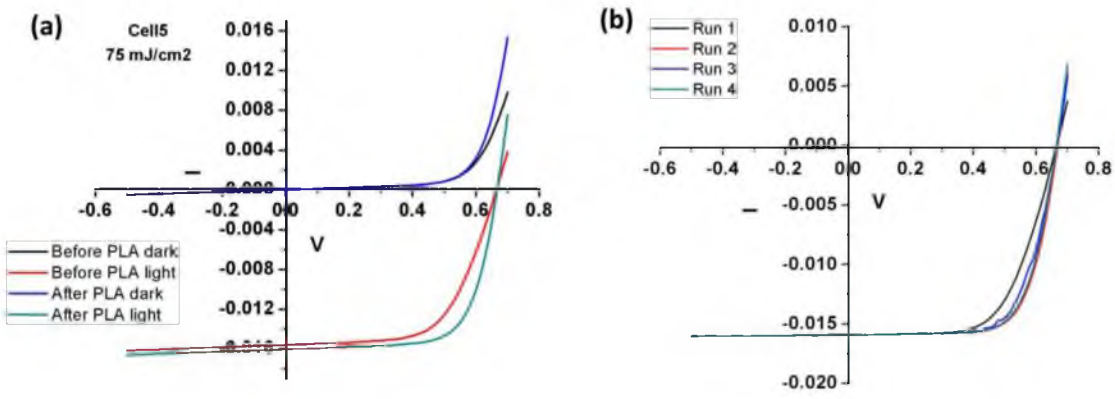

Figure 7.1: Current-voltage results on the solar cells. (a) I_{SC} improvement after PLA using 1064 nm laser and (b) Reduction in FF because of improper electrical connection.

Fig. 7.1(b)). As can be seen, the error induced by improper measurement only affects FF and not I_{SC} or V_{OC} of the cell. Hence one should always make multiple measurements (at least three) in order to verify the observed behavior.

7.4 Chapter 6

7.4.1 Summary and conclusions

Chapter 6 presents a comparison of efficient CIGSe and CZTSe samples using various electrical characterization techniques. The net carrier concentration versus depth plots deduced from capacitance-voltage (C-V) measurements suggests similar concentration profiles except for an order of magnitude higher carrier concentration for CZTSe and 5 times smaller depletion width at equilibrium. The TAS data on both the cells look quite different. While the CIGSe samples experience a dielectric freeze out at relatively lower temperatures ($T < 100$ K) and higher frequencies (> 1 MHz), CZTSe samples experience a dielectric freezeout at around 150 K and lower frequencies. A common feature for both the CIGSe and CZTSe cells is that in the DLTS spectrum the peaks/valleys observed are relatively broad. DLTS data suggest majority carrier related

defect states at around ≈ 550 meV for CIGSe and ≈ 350 and 600 meV for CZTSe samples, respectively. MCDLTS experiments suggests that the observed defect state in CZTSe might be a recombination center. This is speculated based on the observed change of behavior of the majority carrier state to minority carrier state as minority carriers (electrons) are effectively injected into the space charge region.

7.4.2 Future work related to Chapter 6

One important thing that needs to be considered for future DLTS or MCDLTS experiments is the contribution from the band tails and multiple defect states with either different ionization energy or ionization state. This is a relevant point because chalcogen semiconductors have a lot of shallow level defects which result in smeared band edges. In addition, if we have closely spaced energy levels or a single state with different ionization states responding to the signal, the data interpretation will be fudged out. This is because (for example) the capture-cross section of the states with similar ionization energy but different ionization state will be different. Hence some information or insight into the material might be lost. Obviously this will involve a theoretical model development in order to design the relevant experiments.

Another relevant experiment would be to test the metastable behavior as well as ageing effects on the samples. These are very crucial experiments, as for real applications we need to understand how chalcogenide properties get affected under the above mentioned circumstances. Some work has been done by various groups dealing with these issues but their proper interpretation as well as how they manifest into device performance is still a matter of active research. Hence the apt experiments would be

trying out bias soaking and or light soaking of the samples and compare the capacitance spectroscopy response to dark soaking of the samples (relaxed state). A complete story needs to be stitched together, suggesting which defects are good and which are bad for device performance.

APPENDIX

FORMATION OF ANISOTYPE p-n HOMOJUNCTIONS

A p-n junction is formed when a p-type and an n-type semiconductor are brought in intimate contact with each other. A p-type semiconductor is one which has holes (electrons) as the majority (minority) charge carriers, while an n-type semiconductor has electrons (holes) as majority (minority) charge carriers. When these two anisotype semiconductors (different type of majority charge carriers) come in intimate contact, diffusion of majority carriers take place from one side to other side. Initially the barrier for majority carrier diffusion is small and the driving force is large because of the huge concentration gradient. However as the diffusion progresses, the driving force for diffusion keeps on reducing. The diffusion of electrons (holes) from n-type (p-type) side to p-type (n-type) side leaves behind the exposed positive (negative) ionic cores on the n-type (p-type) side. This sets up an electric field pointing from positive ionic cores towards negative ionic cores. It is important to note that this electric field (drift) will be in a direction opposite to the driving force for diffusion. Eventually a stage will arrive when the diffusion and the drift fields will balance each other. This stage is termed as steady state. Again it is important to realize that steady state does not mean that the movement of charge carriers has ceased. In fact under steady state charge carriers do move but the net movement is such that there is no charge accumulation on either side or

the diffusion and drift process counterbalance each other. Under this scenario a spacecharge region (SCR) or the depletion region that is devoid of any free charge carriers and contains only the fixed ionic cores exists between the p-type and n-type side. This condition represents the dynamic equilibrium condition of the p-n junction diode. The electric field that points from the positive ionic cores towards negative ionic is termed the built-in electric field, which also implies the presence of a built-in voltage difference between the sides. This built-in voltage acts as a barrier for the electrons (holes) which have a natural tendency to go down (up) the hill. Figure A.1 illustrates the principal of formation of p-n junction step by step. As can be seen at time $t < 0$, p-type (n-type) semiconductor has excess holes (electrons) and negative-acceptor cores (positive-donor cores). Hence the net charge density in the semiconductors is zero. However, when the two anisotype semiconductors are brought in intimate contact with each other (Fig. A.2) charge carriers begin to flow and once the equilibrium stage is reached an SCR devoid of any free charge carriers develops in between the two anisotype semiconductors.

The above discussion on the formation of p-n junction was a qualitative view to the ideal p-n junction. Now let us try to quantify the p-n junction formation and derive the basic equations related to it.

Again, when p and n type semiconductors are brought in intimate contact with each other, excess free carriers move from one side to other side. The driving force for the movement is the difference in the electrochemical potential of the free carriers. This electrochemical potential is termed as the Fermi energy or level (E_f) of the free carriers. The Fermi level is defined as an arbitrary energy level that represents the charge

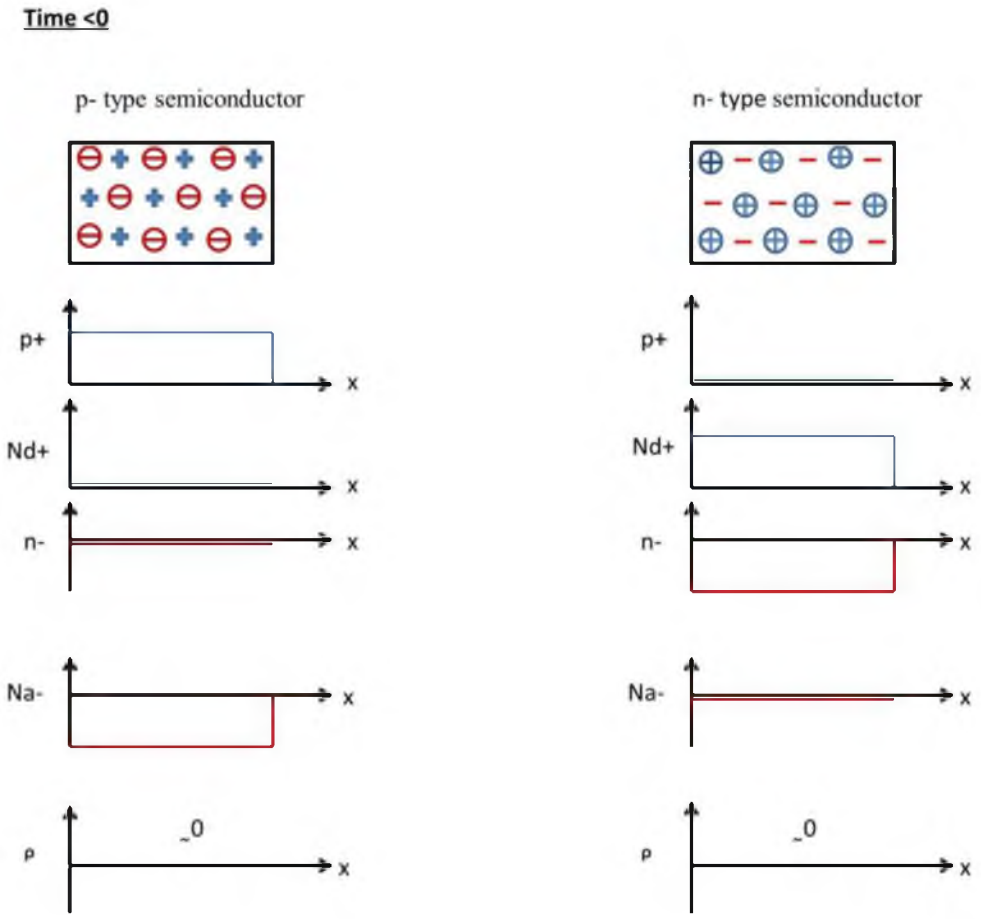

Figure A.1: Representation of p and n type semiconductors before they are brought in intimate contact with each other. As the number of holes (electrons) is approximately equal to negative-acceptor ions (positive-donor ions) the net charge density in p-type (n-type) semiconductor is ≈ zero.

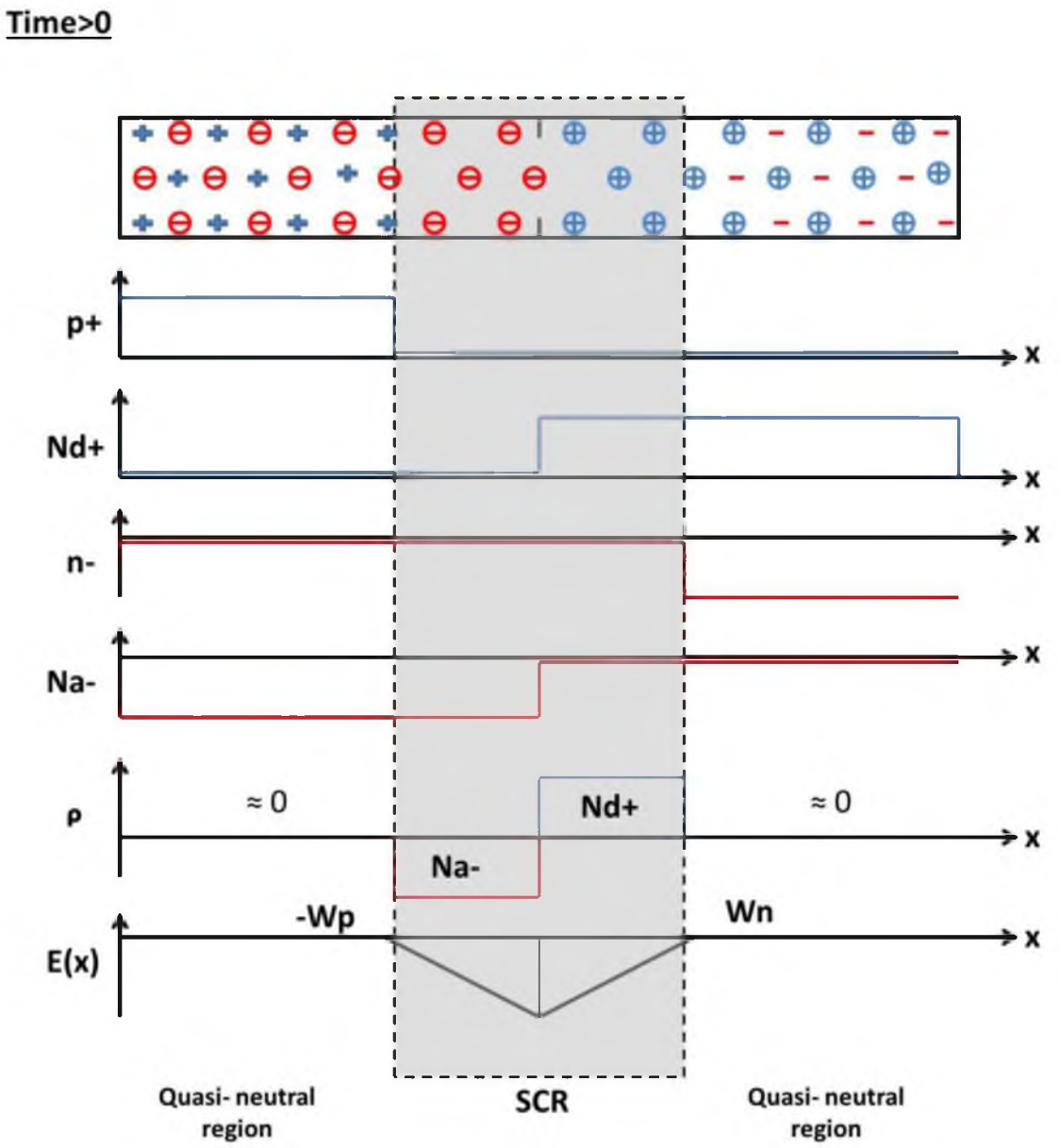

Figure A.2: Formation of p-n junction when p and n type semiconductors are brought in intimate contact with each other. At t>0, equilibrium stage is achieved all throughout the p-n junction and a space charge region (SCR) is formed in between the two anisotype semiconductors. The SCR is devoid of any free charge carriers but has positive (negative) ionic cores on the n-type (p-type) side. This leads to a built-in field across the SCR.

neutrality position in the semiconductor on the energy scale. Roughly speaking it gives an idea about the average energy of the free carriers. Now, for a p-type (n-type) semiconductor that has excess holes (electrons), E_f lies close to the valence (conduction) band. Because of the difference in E_f on both the sides, the system would try to minimize its energy when in intimate contact. Thus at equilibrium or steady state, E_f is constant throughout the p-n junction. However, because of the difference in the E_f on both the sides initially, a built-in voltage (V_{bi}) or potential is created at the interface which acts as a barrier for the carrier's movement once the steady state is achieved.

As per the Maxwell-Boltzmann statistics, for a two-energy level system separated by energy (ΔE), the carrier concentration at the two levels can be related by the following equation:

$$\frac{n_2}{n_1} = \exp\left(\frac{-\Delta E}{k_b T}\right) \tag{A.1}$$

where n_2 and n_1 are the concentrations of the carriers at the two-energy levels, k_b is the Boltzmann's constant and T is the absolute temperature. Now, if we assume that the concentration of majority carrier holes (electrons) on the p-type (n-type) side at equilibrium is p_{p0} (n_{n0}) while the concentration of minority carriers electrons (holes) on the p-type (n-type) side is n_{p0} (p_{n0}), we could write:

$$\frac{p_{n0}}{p_{p0}} = \exp\left(\frac{-qV_{bi}}{k_b T}\right) \tag{A.2}$$

Also,

$$\frac{n_{p0}}{n_{n0}} = \exp\left(\frac{-qV_{bi}}{k_b T}\right) \tag{A.3}$$

Now as per the mass-action law:

$$p_{p0}n_{p0} = {n_i}^2 = n_{n0}p_{n0} \tag{A.4}$$

Thus from equations A.2, A.3 and A.4 solving for V_{bi} gives:

$$V_{bi} = \frac{k_bT}{q} \ln\left(\frac{n_{n0}p_{p0}}{{n_i}^2}\right) = \frac{k_bT}{q} \ln\left(\frac{N_aN_d}{{n_i}^2}\right) \tag{A.5}$$

where N_a and N_d are the majority carrier concentration on the p-type and n-type side, respectively, and n_i is the intrinsic carrier concentration.

Now let us try to calculate the width of SCR or the depletion region. In order to simplify the analysis, let us assume that the depleted charge has a box profile or abrupt junction is formed. Since the p-n junction considered here is at equilibrium, the net charge density on the p-type side and the n-type side across the SCR must be equal. Thus it follows that:

$$N_aW_p = N_dW_n \tag{A.6}$$

where W_p and W_n are the width of SCR on the p and n type side respectively. Again as per Gauss's Law:

$$\frac{dE}{dx} = \frac{\rho_{net}(x)}{\varepsilon} \tag{A.7}$$

in which ε is the permittivity or the dielectric constant of the medium. Thus the built-in field across the SCR can be calculated by:

$$E(x) = \frac{1}{\varepsilon}\int_{-W_p}^{x} \rho_{net}(x)dx\ ;\ -W_p \leq x\ \leq 0 \tag{A.8}$$

and

$$E(x) = \frac{1}{\varepsilon}\int_{x}^{W_n} \rho_{net}(x)dx\ ; 0 \leq x\ \leq W_n \tag{A.9}$$

Again assuming full ionization,

$$\rho_{net} = -q\ N_a\ ;\ -W_p \leq x\ \leq 0 \tag{A.10}$$

And

$$\rho_{net} = -\ q\ N_d\ ;\ 0 \leq x\ \leq W_n \tag{A.11}$$

Thus,

$$E(x) = -\ \frac{1}{\varepsilon} q\ N_a\ (x + W_p);\ -W_p \leq x\ \leq 0 \tag{A.12}$$

And

$$E(x) = \ -\frac{1}{\varepsilon} q\ N_d\ (W_n - x);\ 0 \leq x\ \leq W_n \tag{A.13}$$

Again at x =0 (metallurgical junction):

$$E(0) = E_{max} = \ -\frac{1}{\varepsilon} q\ N_a\ (W_p) = \ -\frac{1}{\varepsilon} q\ N_d\ (W_n) \tag{A.14}$$

and

$$E(-W_p) = E(W_n) = 0 \tag{A.15}$$

Now from Figure A.2,

$$V_{bi} = Area\ of\ triangle = \frac{1}{2}\ (W_n + W_p)|E_{max}| = \frac{1}{2}\ (W_{total})|E_{max}| \tag{A.16}$$

where $W_{total} = W_n + W_p$. Now, the net charge density can also be calculated as:

$$N_{net}\ W_{total} = N_a\ W_p = N_d\ W_n \tag{A.17}$$

in which:

$$\frac{1}{N_{net}} = \frac{1}{N_a} + \frac{1}{N_d} \tag{A.18}$$

Thus

$$W_{total} = \frac{2\,V_{bi}}{E_{max}} \tag{A.19}$$

$$W_{total} = \frac{2\,V_{bi}\,\varepsilon}{q\,N_a\,(W_p)} = \frac{2\,V_{bi}\,\varepsilon}{q\,N_d\,(W_n)} = \frac{2\,V_{bi}\,\varepsilon}{q\,N_{net}\,(W_{total})} \tag{A.20}$$

$$W_{total} = \sqrt{\frac{2\,V_{bi}\,\varepsilon}{q\,N_{net}}} = \sqrt{\frac{2\,V_{bi}\,\varepsilon\,(N_a+N_d)}{q\,N_aN_d}} \tag{A.21}$$

Thus for a one-sided abrupt junction (n^+-p), $N_d >> N_a$:

$$W_{total} = \sqrt{\frac{2\,V_{bi}\,\varepsilon}{q\,N_a}} \tag{A.22}$$

It can be realized from equation A.22 that for an abrupt one-sided junction the depletion region extends in the low doping side.

Also from equation A.17, A.18 and A.21 it can be shown that:

$$W_p = \sqrt{\frac{2\,V_{bi}\,\varepsilon\,N_d}{q\,N_a(N_a+N_d)}} \tag{A.23}$$

and

$$W_n = \sqrt{\frac{2\,V_{bi}\,\varepsilon\,N_a}{q\,N_d(N_a+N_d)}} \tag{A.24}$$